One-Dimensional Quantum Transport Phenomena in Periodically Modulated Electron Waveguides

Elliott Mansfield

Quantum Optics and Quantum Many-Body Systems Group

Department of Physics

University of Strathclyde, Glasgow

May 7, 2024

This thesis is the result of the author's original research. It has been composed by the author and has not been previously submitted for examination which has led to the award of a degree.

Signed: Elliott Mansfield
Date: 28/02/2023

Acknowledgements

First, so many thanks go to my supervisor, Andrew Daley. Never have I seen someone so passionate about physics! It's incredibly inspiring, and with his help I've developed into a capable researcher. On this latter regard, I also want to thank François Damanet and Johannes Kombe, who have both been extremely patient with me as I've struggled through this. Their support both within physics and outside has been instrumental in me getting this far, and so eternal gratitude goes to them. Many thanks also to Callum Duncan for all his advice on my thesis and the future.

I dedicate this thesis to my loving girlfriend Lilou Jourdain, without whom there is no way I would have made it through this. My parents (Helen and David Mansfield) and sisters (Keely, Georgia, and Rachel Mansfield) have also been wonderfully supportive throughout, and so I also would like to thank them.

I'm basically forced to thank Harikesh Ranganath. Since we met right at the start of our MSc Advanced Physics, he's been an incredible friend. I wish him all the best at JPL!

I also want to thank the rest of the current and former QOQMS group members, who have motivated me and held interesting discussions with me. These are Stuart Flannigan, Tomohiro Hashizume, Jorge Yago, Rosaria Lena, Gerard Pelegri, Anton Buyskikh, Eduardo Mascarenhas, Tomas Kozlec, Sebastian Schmidt, Ieva Cepaite, Liam Walker, Sridevi Kuriyattil, and Tom Bintener. From the wider CNQO group, I also thank Peter Kirton, Simon Kothe, Ewen Lawrence, Jack Yang, and Mark Carroll.

Elliott Mansfield, 31st January 2023

Abstract

The study of quantum transport in one dimension is of great interest in many areas of condensed matter physics. This thesis is motivated by conductance measurements in modulated LAO/STO nanowires, where a strong conductance baseline of $2e^2/h$ is observed when a Kronig-Penney potential is applied, which survives up to external magnetic fields > 18 T. This is also observed when the nanowire is helically modulated, but an additional feature is the appearance of conductance oscillations above the $2e^2/h$ baseline which occur at lower energies than the $4e^2/h$ peak.

In order to model this, we begin by constructing an electron waveguide model for the nanowire formed at the LAO/STO interface. We then include the effect of periodic modulations and associated spin-orbit coupling resulting from these, and analyse the resulting band structure and conductance, finding that a single electron model is not sufficient to explain the $2e^2/h$ baseline. This was found in previous work, and the solution is to include electron-electron interactions.

To include the effects of these, we begin with a standard BCS-like mean-field model. To study first the effect coming from a periodic modulation of the potential in the waveguide (vertical modulation), we introduce only the associated spin-orbit coupling to this model. We find that this leads to enhanced pairing, and could potentially explain the strong baseline of $2e^2/h$. Additionally, we look only at the effect of a periodic modulation in the centre of the nanowire (lateral modulation),

which we find introduces triplet pairing in the waveguide region.

Combining these two modulations together, we extend the mean-field model again to include the form of the modulation potential alongside associated spin-orbit couplings to study the helical waveguide. We observe enhanced pairing and triplet pairing simultaneously. To study the oscillations in conductance, we introduce a phenomenological pair scattering model where triplet pairs incedent on the interface between helical and unmodulated regions can backscatter. We find that this model can indeed produce oscillations above the $2e^2/h$ baseline.

Contents

Chapter 1

Introduction

As computers become smaller, a point is eventually reached where the physical properties of wires and transistors are no longer well described by classical and semi-classical models used for designing these modern devices. In these regimes, the quantum behaviour of electrons plays a significant role [1]. Thus, the study of quantum transport of electrons in nanowires using quasi-1D models will be necessary for the continuation of the miniaturization of computing.

The field of quantum transport deals with the quantum-mechanical motion of particles in non-equilibrium systems. This is most readily observed in low dimensions (0,1, and 2D). The most prominent example of this is in solid state systems, where devices such as semiconductors and transistors rely on quantum transport phenomena to function.

Quantum transport is not just limited to solid state physics – another area where this is of interest is the study of ultracold atoms [2]. In cold-atomic systems, atoms (which can be either bosonic or fermionic) are contained in a magneto-optical trap within a vacuum chamber. The atoms can then move by hopping between sites on the lattice generated by the trap. Transport in ultra-cold atoms is generally much more controllable than in the solid state as the underlying physics of the system is cleaner. However, it comes with its own challenges. For example, generating a potential gradient is more difficult, dissipation of photons can prevent the systems from reaching their desired state, and to study magnetic effects we must engineer artificial gauge fields. Despite this, hallmark quantum transport features such as the quantum Hall effect [3] and conductance quantization [4] can be experimentally measured.

Beyond computing, quantum transport offers a platform to study non-equilibrium quantum physics [5]. It can aid in understanding the physics that underpins new technologies such as quantum batteries [6] and optoelectronic devices [7]. It is even useful in quantum computing [8].

The complex metal-oxide heterointerface Lanthanum Aluminiate-Strontium Titanate (which for the remainder of the thesis will be referred to as LAO/STO or $LaAlO_3/SrTiO_3$) is one of many exciting new materials being created in solid state labs [9]. The physical properties of the two-dimensional electron gas (2DEG) formed at the interface between the two materials making it up are highly tunable, and wires can be written onto these devices [10], making them an extremely attractive option for mass production. This material also hosts a variety of interesting phenomena, including gate-tunable conductance [11], ferromagnetism [12], and even superconductivity [13]. LAO/STO has been gaining ground as an exciting platform for studying quantum transport in various 2D and 1D geometries. This material will be discussed in more detail in Sec. 1.2.

One potential use of a system with highly controllable features is quantum simulation [14]. Side gates can be used to tune electron density [11], and even the strength and nature of electron-electron interactions [15]. This means that Hamiltonians of interest could potentially be programmable in LAO/STO devices. However, much is still unknown about how they work. While the strength of the interaction was shown to be tunable [15], the origin and even behaviour (short versus long range, and the sign of the interaction) are still largely a mystery. So, in order to fully utilise this platform to its potential, a much deeper understanding of the underlying physics must be achieved.

This is where one-dimensional channels are extremely useful. The waveguide model captures well the underlying physics of these devices despite its relative simplicity [16], and it gives a clean platform to build more complicated models on. The goal of this work is to study the effects of perturbing the simple waveguide model through the addition of external periodic modulations. Not only does this give an extra degree of control over the electronic behaviour in these systems, it also leads to a number of novel features, which can perhaps be used to shed some light on the nature of electron-electron interactions in these nanostructures.

We will now discuss quantum transport and LAO/STO in more detail. Following this, an overview the results of the thesis will be given.

1.1 Introduction To Quantum Transport

One of the hallmark features of quantum mechanics is wave-particle duality. Essentially, this means that every particle has some wavelength known as the de Broglie wavelength. As electronic systems become smaller, the length scales of the wires become similar to the de Broglie wavelength of the electrons, and so wave-based effects become important, meaning electrons can no longer be described by a “billiard ball” type particle model [16]. Instead, they should be treated as interfering waves inside the channel. The billiard ball model can still be broadly useful as an illustration of the different types of quantum transport though, as in Fig. 1.1, by thinking of the illustrated paths as semi-classical trajectories.

The transport behaviour in nano-scale systems is very dependent on length scales. The quantum transport behaviour can be characterised by the mean free path l of the electrons: the distance an electron travels, on average, before scattering in a channel [17]. If l is small compared to the length of the channel L, then the electron is scattered many times on its journey from source to drain (Fig. 1.1a). In this case, the coherence of the wave is gradually lost, and this kind of electron transport is known as diffusive.

However, if the mean free path is long compared to the length of the channel, then electrons are unlikely to be scattered (Fig. 1.1b). This means that the coherence properties are maintained during the transport processes, meaning the quantum behaviour is strongly preserved. This is known as ballistic transport. It is this regime of electron transport that will be the focus of the work presented here.

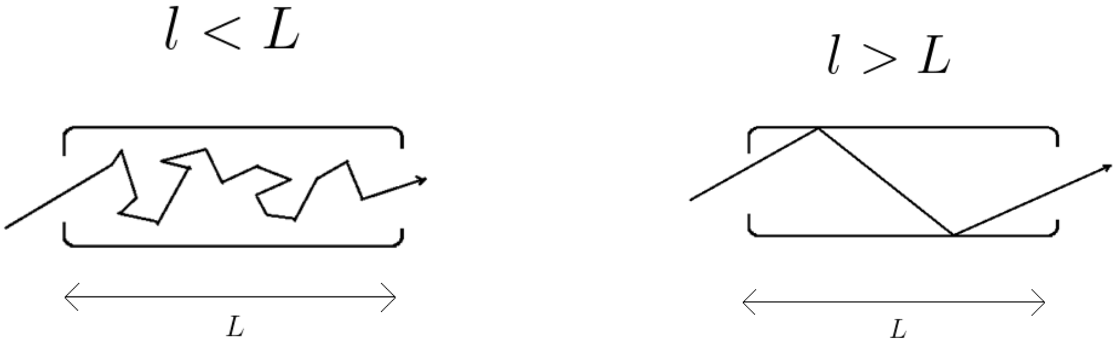

Figure 1.1: The difference between diffusive and ballistic transport. (a) Diffusive transport for $l < L$, showing the electron being scattered in the channel. (b) Ballistic transport for $l > L$, showing no scattering in the channel, only coherent confinement in 1D. This figure is adapted with reference to Fig. 7 of [16].

The mean-free path can be used to define another important quantity in transport, the electron mobility. This is essentially a measure of how strongly electrons feel an applied electric field. We define this as

$$\mu_e = \frac{e}{m_e v_F} l, \tag{1.1}$$

where $v_F = \frac{\hbar k_F}{m_e}$ is the Fermi velocity, m_e is the electron mass, and e is the electronic charge. The importance of this number is that the effective electronic velocity in an applied field is given by $\vec{v}_e = \mu_e \vec{E}$. We define and motivate this now, as it leads to the appearance of interesting physics when discussing the materials in the next section. Thus, when a voltage is applied, the conductivity is expected to be proportional to this mobility. So one can imagine that a higher mobility would lead to regimes where quantisation of transport is more easily observed, whereas low electron mobilities would obscure this and lead to more subtle properties.

1.2 Conductance Quantization

The main feature of quantum mechanical transport which underpins this thesis is the quantization of conductance (the name given to the inverse of resistance). This feature is special to one dimensional systems due to the absence of a Fermi surface – instead we have a finite number isolated Fermi points at the Fermi energy which can be populated [18]. This is discussed in more detail in Ch. 2.

Quantised conductance was first observed in quantum point contacts in 1988 by van Wees *et al.* [19], but had previously been argued for by Landauer [20], whose name now adorns the formula used to calculate conductance in quantum systems. Since then, it has been observed in numerous places such as in GaAs based heterojunctions [21], and indeed in LAO/STO [22].

This is not solely a single particle phenomenon either. Meir and Wingreen derived an interacting equivalent to the Landauer formula [23], and Maslov and Stone used Luttinger liquid theory to show that conductance through an interacting system is determined by the leads [24], and so quantization of conductance is preserved when the leads are non-interacting.

1.3 Quantum Transport Gallery

While this thesis is motivated by experiments in LAO/STO nanowires, the field of low dimensional quantum transport is much wider. To make an exhaustive list would take far too long, but I present here a few topics related to other systems in quantum transport that I find interesting to highlight the place of my research within the wider field.

1.3.1 0D transport

While one dimension already seems low dimensional, it is possible to go even lower to 0D transport. This occurs when the channel confinement is such that only a few states exist and there are no continuous degrees of freedom. Examples include quantum dots [25] (which in their simplest form are a single site which can host up to two electrons in total), quantum point contacts [26] (which can be 0D or 1D, and interestingly were recently realised in 1D in $SrTiO_3$[27]), and molecular junctions [28]. The lack of continuous degrees of freedom in these systems naturally leads to quantum features, such as the quantization of current [29].

1.3.2 Graphene - Nanotubes And Nanoribbons

One of the most promising topics in condensed matter physics is the applications of graphene. Putting aside the higher dimensional physics of twisted bilayer, even in quasi 1D there is plenty of rich physics to explore. Quantized conductance has been observed in carbon nanotubes (CNTs) [30], and in graphene nanoribbons (GNRs) it has been shown that heterojunctions between different surface configurations can be formed locally [31] allowing for the study of novel features like oscillations in conductance [32] predicted to occur in these systems. Their conductivity can also be controlled by doping with nanoparticles [33, 34].

1.3.3 Disordered Systems

In LAO/STO, ballistic transport can be observed, which suggests the electronic environment is clean. This is not the case in every system however. When disorder is introduced into the potential landscape, states become localised which means transport through the entire system becomes impossible [35, 36]. This is known as Anderson localisation and occurs for dimensions as high as two [37]. While this is well studied in non-interacting systems, the analogous many body localisation (MBL) is one of the most active topics of research in quantum many-body physics [35, 38, 39].

1.3.4 Exciton Transport

Excitons offer an entirely new perspective on electronic transport in nanostructures. These form when electrons in the valence band are excited by light into the conduction band, forming a bound state between the electron and the hole. This has some finite lifetime, before the light is re-emitted. Through this, transport in nanostructures can be studied from an optics perspective, rather than measuring currents and voltages. Transport in these systems tends to be diffusive (see [40]), but ballistic exciton transport is possible in optical microcavities when a polariton is formed [41]. This is an extremely rich field, but is far beyond the scope of my research, thus the brevity of this section.

1.4 LAO/STO

In this section, we will describe briefly the physics of the material, and summarise the process used in fabricating the electronic devices that this thesis seeks to model.

Both of the metal-oxides LAO and STO on their own are insulators. However, $SrTiO_3$ has been shown to support bulk superconductivity in the presence of a dopant [42]. The interesting electronic effects occur at the interface between the two metal-oxides, where under correct conditions a two-dimensional electron gas (2DEG) can form. This is a 2D conductive layer with properties similar to that of a metal, but comparatively has a much lower electron density [16]. The exact reason for this occurring in LAO/STO is still an active topic of research, but there are several proposals about the energetic nature of this region which could support a conducting interface [9, 43–46]. However, what is known about the formation of the 2DEG in LAO/STO, is that there is a critical thickness of four unit cells of $LaAlO_3$ for this to occur. [11].

While this 2DEG alone is extremely interesting for the variety of phases attainable, the electron mobility is quite low. Thus, in two dimensions, it is difficult to observe ballistic quantum transport. It was discovered that in 1D channels at the interface, these devices can lead to clean ballistic transport [22]. The number of electronic channels available for transport in these highly quantum regimes can essentially be counted based on transport measurements (this will be described in more detail in Ch. 2).

To make the one dimensional nanowires, the bulk layer of $SrTiO_3$ is supplied with only three layers of $LaAlO_3$, keeping the interface in an insulating state. However, by using a conductive Atomic Force Microscope (c-AFM), the surface of the $LaAlO_3$ can be protonated to locally tune the interface from insulating to conducting [10] (see Fig. 1.2). This is known as c-AFM lithography. By using this technique, nanowires can be “written” onto the $LaAlO_3/SrTiO_3$ interface cleanly.

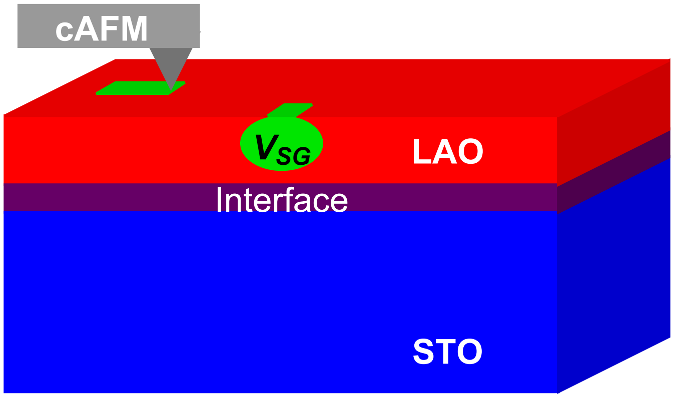

Figure 1.2: Schematic of the setup of the LAO/STO interface. The upper surface of the LAO (pictured in red) is grown on top of the STO bulk (in blue). This is then protonated in a narrow channel (green) by the cAFM tip to tune the LAO/STO interface (purple) from insulating to conducting. The side gate voltage V_{SG} controls the chemical potential in the waveguide region.

One thing to note is the geometry of the nanowire devices, which is illustrated in Fig. 1.3. The two leads are written on either side of the device, each with two terminals for four terminal measurements. The reasoning behind having a separate set of terminals for current and voltage measurements is that it means that the resistance of the leads does not contribute to the measured resistance (source: wikipedia). In order to observe clean conductance features, it is required that each of the leads is separated from the nanowire region by a transparent tunnelling barrier. The reason for this is not fully understood, but the barrier geometry was fully investigated in the

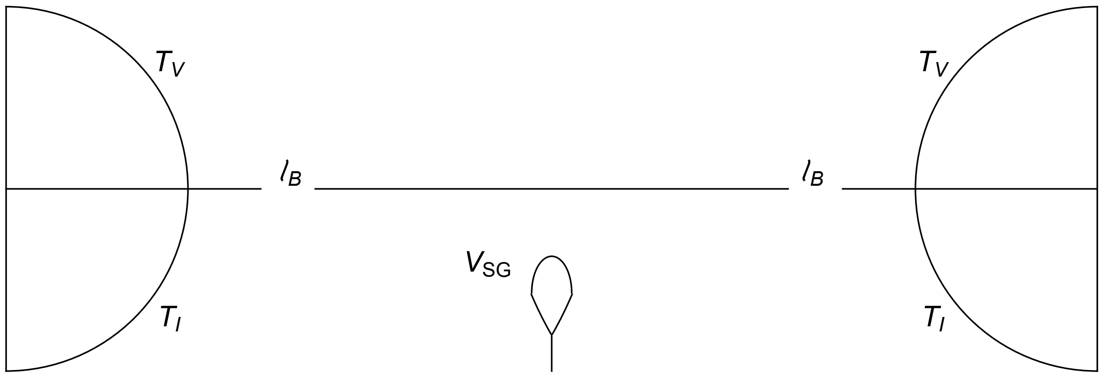

Figure 1.3: Sketch of the geometry of the LAO/STO devices created for the experiments that inspired this thesis. The waveguide region has four terminals, two to control voltage (T_V) and two to measure current (T_I). These are connected to the leads which are separated from the nanowire by a tunnelling barrier of length l_B. The voltage V_{SG} is the side gate which controls the chemical potential in the nanowire.

supplemental material of [22] finding that two barriers led to much cleaner quantised conductance measurements than only one or zero barriers.

It should be mentioned that when referring to results in LAO/STO nanowires, the word conductance refers specifically to conductance at zero-bias. These measurements are taken by making small variations in the voltage around zero and measuring the resulting current in order to calculate the derivative of the voltage with respect to current at $V = 0$. This will be reiterated in Ch. 2, but all calculations of conductance in the thesis unless specifically mentioned otherwise refer to zero-bias conductance.

Additionally, there is the inclusion of a side gate. This is an independent conductive region which generates an electric field in the waveguide region when a voltage V_{SG} is applied. This effectively tunes carrier density in the conducting region, and thus is used to control the chemical potential in the nanowire [22]. By tuning the chemical potential, a large degree of control is possible over the conductive properties of the one-dimensional channels.

1.5 Overview Of This Thesis

In this thesis, the goal is to develop a theoretical understanding of how interacting transport features are affected by periodic modulations. This is connected to LAO/STO through an engineered spin-orbit coupling that results from the modulations, which is also included in the formalism developed. The motivation for this thesis is a series of experiments from the group of Prof. Jeremy Levy at University of Pittsburgh ([47], [48], [49]) on periodically modulated nanowires in LAO/STO, in which unusual transport phenomena were observed. This includes electron pairing up to extremely high magnetic fields ($> 18T$), and conductance oscillations. This thesis lays the groundwork for understanding these effects, showing that a potential modulation along with its spin-orbit coupling in LAO/STO leads to enhanced pairing. Additionally, we propose that the scattering of triplets at the interface between helical and unmodulated regions in helically-modulated nanowires is responsible for the oscillations in conductance.

In Ch. 1, the thesis is outlined, and we review the literature. While the models used within this thesis are general enough to be applied outside of the specific material, the work was performed in close collaboration with experiments on these structures performed by the group of Prof. Jeremy Levy at the University of Pittsburgh.

In Ch. 2, we begin with the details of the quantum transport models used in the thesis. A derivation of the Landauer current and conductance formulae is shown. We then discuss the physics of Rashba spin-orbit coupling, an effect which occurs when there is the lack of inversion symmetry, like at the LAO/STO interface. We then discuss how to treat periodic potentials analytically, presenting the case of a cosine potential included in the Hamiltonian. This section concludes with an introduction to the mean-field theory used to treat interactions, making reference to the BCS theory of superconductivity, finishing with a brief description of the iterative procedure we use to solve and analyse the model.

Ch. 3 is dedicated to the physics of straight waveguides. We first include the effects on the kinetic energy as a result of an external magnetic field perpendicular to the conducting region, and show how this leads to a suppression of the kinetic energy term along with an increase in the confinement frequency and how these effects change the band structure. The single particle conductance and transconductance features of an unmodulated LAO/STO waveguide are then detailed. In the final part of the section, the mean-field techniques covered in the previous chapters are used construct phase diagrams of the interactions between various bands to identify where the single particle Landauer formula should be used to calculate conductance, and where one must resort to the Maslov-Stone theorem.

In Ch. 4, the work produced for the papers *One dimensional Kronig-Penney nanowires at the* $LaAlO_3/SrTiO_3$ *interface* [47] and *Spin-orbit assisted pairing in modulated electron waveguides* [50] is detailed. The Kronig-Penney modulation is included in the waveguide model via scattering arguments, and this leads to very similar features in the band-structure as a cosine wave. We then discuss how the modulations lead to an engineered spin-orbit coupling. Following this, the spin-orbit coupling is introduced into the Kronig-Penney model in order to write down the full single electron model for the waveguide. Neglecting the form of the potential to focus on the effects of the spin-orbit couplings, we study individually their effects. Additionally, the same features are studied for the inclusion of a lateral modulation in the waveguide centre, and we analyse the difference in physics between the lateral and vertical modulations.

In Ch. 5, we discuss quantum transport in a helical waveguide. Two approaches are taken. First, the periodic modulations are included in the mean-field model to systematically study the effects this has on correlation functions and phase diagrams. Secondly, we introduce a phenomenological pair-scattering model which suggests that the stable pair-singlet phase could be complemented by an oscillating pair-triplet phase.

This thesis concludes in Ch. 6 by summarising the material of the thesis and giving an outlook.

During my PhD, I have had two papers published in high quality journals. These are *One dimensional Kronig-Penney nanowires at the* $LaAlO_3/SrTiO_3$ *interface* [47] and *Spin-orbit assisted pairing in modulated electron waveguides* [50]. Another, *Engineered chirality of one-dimensional nanowires* [51], has been submitted for publication, and a follow-up paper is in preparation on the remaining unpublished material in Ch. 5. Additionally, I gave the oral presentation *Quantum transport in periodically modulated electron waveguides* at the APS March Meeting 2021. Finally, I presented the following posters: *Quantum Transport in Modulated Electron Waveguides* (PQI 2019); *Effects of Kronig-Penney Potential on Quantum Transport* (PQI 2020); *Controlling Quantum Transport in Electron Waveguides by Periodic Modulation* (PQI Quantum2020); *Controlling Quantum Transport in Modulated Electron Waveguides* (PQI 2021); *Electron Pair Transport in Periodically Modulated Waveguides* (DES-OEQ/QSUM 2022).

Chapter 2

Background

This chapter gives an overview on the background material that will be used in the thesis. We introduce the important electronic transport properties that are studied in the thesis, namely the current, conductance and transconductance, and include a derivation of how the conductance is obtained from the current. We will discuss how to obtain the conductance from single particle band structures. Following this, we will cover two important single-particle features: the effect of periodic potentials on the transport channel, and the effects of Rashba spin-orbit coupling on the band structure and conductance signatures. Finally, we include electron-electron interactions at the mean-field level and summarise the techniques used for determining the excitation spectra and quantum phases of interacting systems under this approximation.

2.1 Transport Properties

To describe clearly the transport properties of interest, it is useful to consider the system introduced in Fig. 2.1, of two leads (often called the source and drain for the

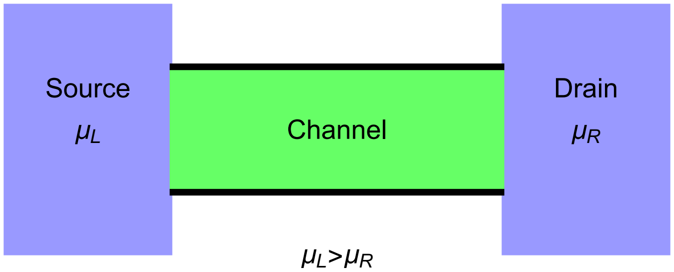

Figure 2.1: Sketch of the simplest model able to capture the essential physics of the transport properties of interest througout the thesis. The source (left lead, higher chemical potential μ_L) is connected to the drain (right lead, lower chemical potential μ_R) via a channel that allows the transport of electrons.

high chemical potential and low chemical potential leads, respectively) connected by a channel. This channel could in principle be any type of system that allows the transport of electrons from source to drain. However, to illustrate the main tools that allow for the study of electron transport, the simplest model is a one dimensional ballistic channel with spin-degeneracy, with a voltage difference $V = \mu_\Delta/e \equiv (\mu_L - \mu_R)/e$ for $\mu_L > \mu_R$, where μ_L and μ_R are the chemical potentials in the left and right leads, and e is the charge of an electron. In the channel, the energy is that of a free particle in one dimension, with energy given by

$$E(k) = \frac{\hbar^2 k^2}{2m_e}, \tag{2.1}$$

with m_e the mass of an electron and k wavenumber corresponding to the momentum eigenvalue $\hbar k$.

2.1.1 Current

The following derivation is adapted from [52]. The current can be written as $I = env$, where e is the charge of an electron, n is the carrier density and v is the group velocity.

However, this is the case where all of the carriers have the same velocity, or if we can work with one average velocity. For different velocity carriers, this equation must be integrated over all momenta, giving

$$I = \frac{e}{\pi} \int_{-\infty}^{\infty} \mathrm{d}k v(k) n_F(E(k) - \mu), \tag{2.2}$$

where $n_F(E(k) - \mu) = 1/(1 + \exp((E(k) - \mu)/(kBT))$ is the Fermi distribution describing the probability of occupancy of the electronic state at energy $E(k)$ and chemical potential μ at temperature T, where k_B is Boltzmann's constant. The velocity here is the group velocity, defined as

$$v(k) = \frac{1}{\hbar} \frac{\mathrm{d}E}{\mathrm{d}k}. \tag{2.3}$$

In the system depicted in Fig. 2.1, the total current is written as $I = I_R - I_L$, where I_R and I_L are the right- and left-moving currents. The right moving current is the current moving out of the left lead, and vice versa, so this becomes

$$I = \frac{e}{\pi} \int_{-\infty}^{\infty} \mathrm{d}k v(k) \left[n_F(E(k) - \mu_L) - n_F(E(k) - \mu_R) \right], \tag{2.4}$$

which upon inserting the group velocity becomes

$$\begin{aligned} I =& \frac{2e}{\hbar} \int_{-\infty}^{\infty} \mathrm{d}E \left[n_F(E - \mu_L) - n_F(E - \mu_R) \right] \\ =& \frac{2e}{\hbar} \left[\mu_L - \mu_R \right]. \end{aligned} \tag{2.5}$$

2.1.2 Landauer Formula For Conductance

The current can be related to another property known as the conductance, which is the inverse of resistance. This is given by the derivative of the current with respect to the voltage:

$$G = \frac{\mathrm{d}I}{\mathrm{d}V}, \tag{2.6}$$

where the voltage is related to the chemical potential bias by $eV = \mu_\Delta \equiv \mu_L - \mu_R$. Therefore, using Eq. (2.6) and Eq. (2.5), the conductance through a single channel is

$$G = e\frac{\mathrm{d}I}{\mathrm{d}\mu_\Delta} = \frac{2e^2}{h}. \tag{2.7}$$

This value is known as the quantum of conductance, G_0. One important point is that this value is obtained for degenerate spins. In the presence of a magnetic field, this channel is split into two channels, one for each spin, and Eq. (2.2) becomes

$$I_\sigma = \frac{e}{2\pi}\int_{-\infty}^{\infty} \mathrm{d}k v_\sigma(k) n_f(E_\sigma(k) - \mu_\Delta), \tag{2.8}$$

where $\sigma = \{\uparrow, \downarrow\}$ designates the two spin channels. The conductance obtained for each of these channels is e^2/h. Despite this, a standard quantum of conductance is still generally referred to as $G_0 = 2e^2/h$.

If there are many channels, the conductance is the sum over the available channels [52]. For N perfectly conducting channels available with degenerate spin states, the conductance is

$$G = N\frac{2e^2}{h}. \tag{2.9}$$

However, real systems are not always perfectly ballistic [1]. Electrons can backscatter in the channel as a result of impurities, causing some electrons originating from the source to be reflected back to the source. This leads to two parameters modelling the probabilities of each case: the transmission probability T is the probability the electron (if measured) is found in the channel, and R is the probability that instead the electron is found to have been reflected. A finite reflection probability means a reduced transmission.

These effects are accounted for by ascribing to each channel some transmission probability $0 \leq T_j \leq 1$, which accounts for both scattering phenomena in the channel and thermal effects, the determination of which is system-dependent. In this case, the equation becomes

$$G = \sum_j T_j \frac{2e^2}{h}, \tag{2.10}$$

which is known as the Landauer formula [53, 54], and is the general formula for conductance in any ballistic channel. As above, this assumes degenerate spins. In the presence of a magnetic field, this is modified to read

$$G = \sum_{j\sigma} T_{j\sigma} \frac{e^2}{h}, \tag{2.11}$$

where again σ labels the spin-dependency of the channels. It is this equation we are going to use throughout to determine the conductance of single-electron transport. In the case where transmission is perfect, there is a straight-forward way to determine the number of available channels for transport based on the band structure. At zero temperature and at zero-bias, electrons fill up the available channels up to the Fermi energy (see Fig. 2.2). This means that the only states available for transport are those at the Fermi energy as all the lower energy states are already filled, and there are no energy excitations to populate higher energy states.

This property is why conductance measurements in the experiments relevant to this work are performed at zero-bias. It offers the cleanest way to study the band structure of the nanowires. As mentioned in Ch. 1, the current is measured at small (such that $eV \ll E$, where E is the energy spacing of the bands) values of positive and negative bias voltage in order to calculate the derivative of the voltage

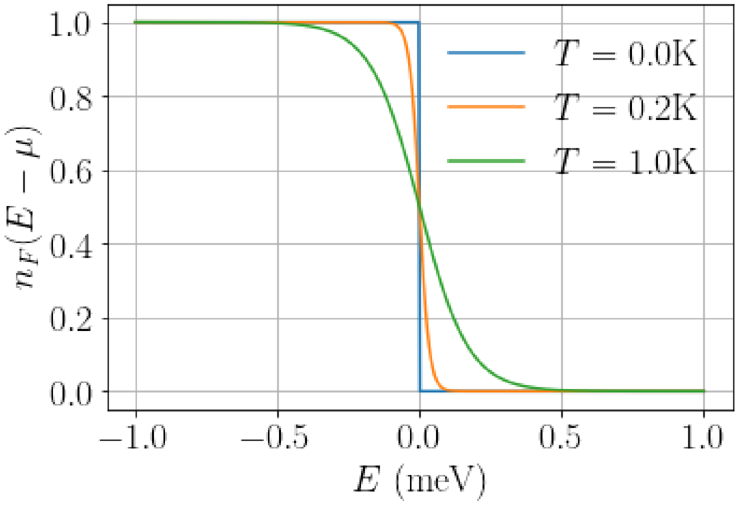

Figure 2.2: The Fermi distribution at $\mu_{SG} = 0$ displayed at various temperatures, showing how states are completely filled until the energy approaches the Fermi energy, above which the occupation drops to zero. The temperature smooths out the step, meaning that a transport channel is available for a range of energies as the width of the curve. The experiments this work is based on take place at much lower temperatures than the orange line (25 mK instead of 200 mK), and so the zero temperature approximation is suitable for the purpose of this work [22].

at zero-bias

To illustrate this, we take a simple 2D case where electrons are confined in a harmonic trap along the direction transverse to propagation. In this system, the energy is

$$E_{n_y,k} = \frac{\hbar^2 k^2}{2m_e} + \hbar\omega\left(n_y + \frac{1}{2}\right), \tag{2.12}$$

where ω is the trapping frequency and n_y labels the energy levels of the trap. ω is determined from the effective mass and nanowire width in the confinement direction as $\omega = \hbar/(m_y l_y^2)$. In the LAO/STO nanostructures of interest, typical values of these are $l_y = 26$ nm and $m_y = 1.9m_e$ [22], so I utilise these values in the following illustrative figures.

Fig. 2.3 provides a clear way to illustrate the physics. Consider starting at $\mu_{SG} = 0$ and scanning up the Fermi energy on Fig. 2.3a. For $\mu_{SG} < 0.03$ meV, the chemical potential is below the band, so there are no bands available for transport and $G = 0$. Then, as this reaches the bottom of the lowest band, in blue at $E_k = 0.03$ meV, two transport channels (spin-up and spin-down for the lowest band) become available at the Fermi energy, and so assuming perfect transmission there is a step up to $G = 2e^2/h$, as is seen in 2.3b at the same value of energy. As μ_{SG} is increased further, more bands become available for transport, and each band contributes $2e^2/h$. From this, the total conductance is $2e^2/h \times$ (the number of occupied bands). In simple terms, the conductance can essentially be counted from the band structure by counting the number of times the Fermi energy crosses a line representing an energy band. This will be useful throughout this thesis.

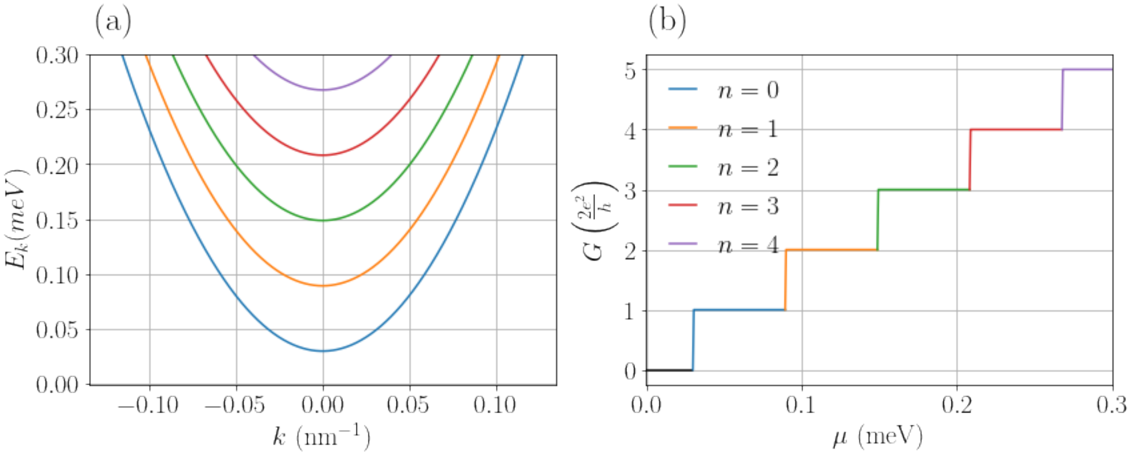

Figure 2.3: The quantization of conductance illustrated: (a) Shows the energy spectrum of such a system for a given frequency $\omega = \hbar/(m_y l_y^2)$ for $m_y = 1.9 m_e$ (m_e is the mass of an electron) and $l_y = 26$nm, with the colours representing different values of n. (b) The zero temperature conductance associated with this spectrum, assuming perfect transmission. The different colours correspond to the highest energy partially-filled band, which is the band responsible for the step in conductance.

In LAO/STO, there are three dimensions. The convention we use is displayed in Fig. 2.4. To summarise, x is the direction of transport, y is the in-plane dimension of the interface (lateral), and z is the out-of-plane dimension with respect to the

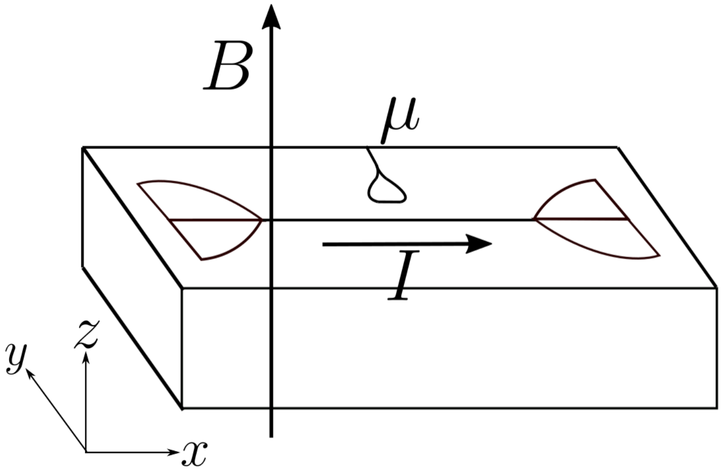

Figure 2.4: A diagram of the LAO/STO interface showing the convention taken within this thesis to the labelling of the position dimensions (x, y, z). I refers to the direction of current flow, and μ_{SG} the chemical potential as tuned by the side gate.

interface (vertical). Modelling both trapping dimensions as harmonic traps, we find there are now two different indices labelling the bands in the band structure, n_y and n_z.

2.2 Rashba Spin-Orbit Coupling

Since the motivation of this thesis is the modelling of transport experiments in LAO/STO nanowires, it is necessary to introduce a very important concept, that of Rashba spin-orbit coupling. This effect occurs when there is an inversion asymmetry around the crystal surface, which in this case is the heterointerface between LAO and STO [55, 56]. The breaking of the inversion symmetry leads to a finite electric field, which interacts with the electron spins. Spin-orbit coupling has various potential applications. For example, the Datta-Das transistor uses spin-orbit coupled regions and spin-polarized leads to build a spin transistor [57]. Additionally, spin-orbit coupling in quantum wires could potentially result in a realization of Majorana fermions [58]. As shall be seen later, the interplay between spin-orbit coupling and electron pairing is also a feature of great interest in one dimensional systems as it can lead to an enhancement of the pairing strength [47, 50].

Due to relativistic effects, electrons (charged particles) moving in an electric field feel a magnetic field, $\vec{B} \propto \vec{p} \times \vec{E}$. In our crystal, this means that higher momentum states generate a larger magnetic field. This magnetic field then interacts with the spin of the electrons, resulting in an overall Hamiltonian given by

$$H_R = \frac{\lambda}{\hbar} \left(\vec{p} \times \vec{E} \right) \cdot \vec{\sigma}, \tag{2.13}$$

where λ is a coupling constant dependent on the properties of the material, and $\vec{\sigma}$ is the 3-dimensional vector of Pauli matrices. This equation is known as the Rashba spin-orbit coupling [59]. The reason that this effect is important in LAO/STO wires is that the LAO/STO interface exhibits a strong Rashba spin-orbit coupling due to the broken surface inversion symmetry. The two metal-oxides have different surface properties which leads to a potential gradient, generating an electric field along the z direction. The Hamiltonian can be rewritten by evaluating the cross product to obtain

$$H_R = \frac{\alpha}{\hbar} (p_x \sigma_y - p_y \sigma_x), \tag{2.14}$$

where $\alpha = \lambda E_z$ is called the Rashba spin-orbit coupling strength [59].

When working with one dimensional waveguides, there is a strong 1D confinement on the electrons. As a result of this, $\langle p_y \rangle \approx 0$ (and additionally $\langle p_z \rangle \approx 0$) and so the contribution of p_y to the energy is neglected to simplify the spin-orbit coupling calculations. This results in the form used throughout the thesis for the Rashba term, which is

$$H_R = \frac{\alpha}{\hbar} p_x \sigma_y. \tag{2.15}$$

The full Hamiltonian is then written as

$$H = \frac{p_x^2}{2m} \mathbb{I} + \frac{\alpha}{\hbar} p_x \sigma_y, \tag{2.16}$$

where $\mathbb{I}$ is the 2×2 identity matrix in the spin degree of freedom. Then, since $[H, p_x] = 0$, p_x is conserved and we can identify simultaneous eigenstates of momentum and energy, and replace p_x by its eigenvalue $\hbar k$ with eigenfunction e^{ikx}, obtaining

$$H = \frac{\hbar^2 k^2}{2m} \mathbb{I} + \alpha k \sigma_y. \tag{2.17}$$

The energy eigenvalues of this are

$$E = \frac{\hbar^2 k^2}{2m_x} \pm \alpha k = \frac{\hbar^2}{2m_x} \left(k \pm \frac{m}{\hbar^2} \alpha \right)^2 - \frac{\alpha^2 m}{2\hbar}. \tag{2.18}$$

Thus, aside from the shift down in energy proportional to α^2, the effect of the spin-orbit coupling is to split the parabola into two, one for each eigenstate (which are now superpositions of $\uparrow$ and $\downarrow$), with minima at $k_c = \pm \frac{m}{\hbar^2} \alpha$, which is displayed in Fig. 2.5a-b.

Using the Landauer formula shows that the conductance is not strongly affected by the presence of the spin-orbit coupling alone, other than by the energy shift bringing down in energy the plateau of $2e^2/h$. This is due to the fact that there are still two electronic channels available, but rather than being spin-up and spin-down, each channel is a superposition of the two. If the system could, for any reason, only inject spin-up electrons and receive spin-up electrons in the drain, then there would

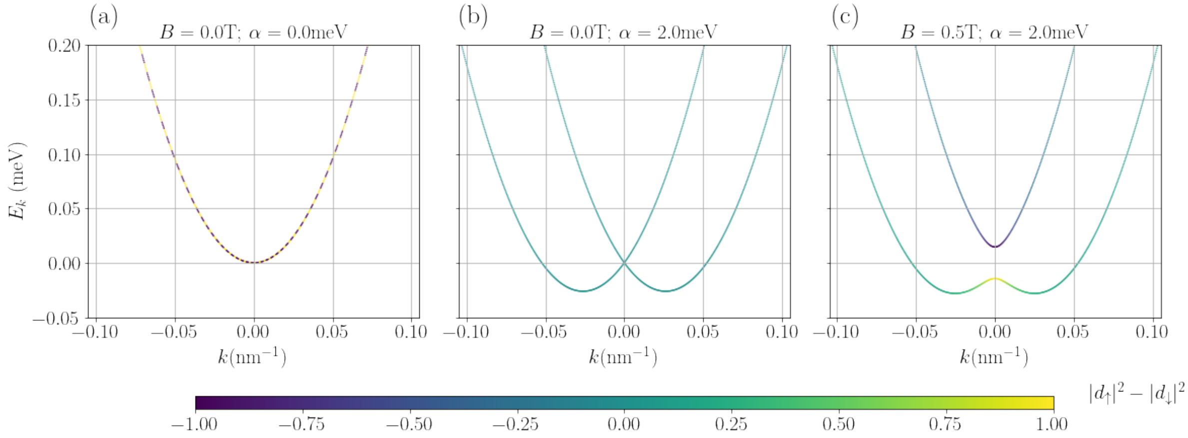

Figure 2.5: The effect of introducing spin-orbit coupling to the band structure. $d_\uparrow$ refers to the $(1,0)^T$ component of the eigenvector corresponding to the eigenvalue E_k, and $d_\downarrow$ to the $(0,1)^T$ component. Thus, the line colour shows the spin-texture of each eigenvalue. (a) The band structure before any spin-orbit coupling is included. The dashed line indicates the spin-degeneracy in this instance. (b) The minimum at $k = 0$ without spin-orbit coupling is split in two at $\pm k_c$ with the spin-orbit coupling, as well as a shift in the energy of the minimum to $-\frac{\alpha^2 m}{2\hbar}$. The spin-orbit coupling results in an equal superposition of the spins except directly at $k = 0$ where the energy of the Rashba term is zero. (c) The effect of including the Zeeman splitting along z on the dispersion relation keeps the positions of the minima at around $k = 0.03\text{nm}^{-1}$, but a gap between the two energy bands opens up at $k = 0$. The magnetic field results in a preference for aligning the spins with the magnetic field at low momentum, before the Rashba energy dominates the spin-texture at higher energies. Throughout, $m = m_e$.

be a reduction in the transmission of spin-up in the spin-orbit case compared to without. This reduction could be calculated from the eigenvectors of Eq. (2.17).

However, the features become more interesting when an additional Zeeman splitting is included. With the inclusion of this term, the Hamiltonian becomes

$$H = \frac{p_x^2}{2m}\mathbb{I} + \frac{\alpha}{\hbar}p_x\sigma_y - \frac{g\mu_B}{2}B\sigma_z, \tag{2.19}$$

where g is the Lande g-factor and μ_B is the Bohr magneton, with eigenvalues

$$E = \frac{\hbar^2 k^2}{2m} \pm \sqrt{\alpha^2 k^2 + \left(\frac{g\mu_B}{2}B\right)^2}. \tag{2.20}$$

By setting $k = 0$, the non-spin-orbit case with a Zeeman shift is recovered, which means there is no spin-degeneracy. This effect of this is illustrated in Fig. 2.5c. where at $k = 0$, a finite gap is observed between the two different energies, with magnitude proportional to B.

This effect manifests strongly in the conductance, as displayed in Fig. 2.6. First, as the Fermi energy reaches the minima of the band structure, the conductance reaches $2e^2/h$ due to the contributions of both spins. Then, as the Fermi energy lies in the magnetic field induced gap between $E_k = \pm g\frac{\mu_B}{2}B$, the conductance is reduced to only e^2/h, before increasing once more to $2e^2/h$ for $E_k > g\frac{\mu_B}{2}B$.

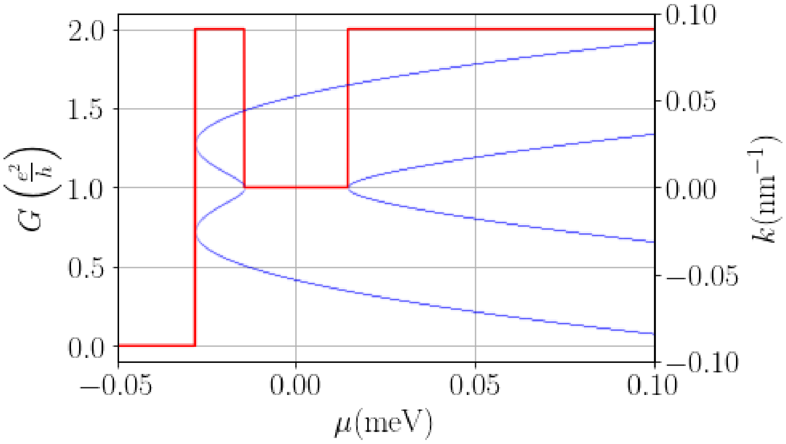

Figure 2.6: Conductance of a 1D system with $m = m_e$ including both Rashba spin-orbit coupling (σ_y) and an external magnetic field (σ_z), displayed in red. The decrease from $2e^2/h$ to e^2/h corresponds to where the Fermi energy lies in the gap induced between the energy bands due to the magnetic field. Alongside this on the right hand y-axis is displayed the band structure (in blue) to demonstrate the relationship between the conductance and the band structure.

2.3 Electrons In Periodic Potentials

The motivation for this thesis is recent experiments on LAO/STO waveguides with periodic potentials applied in the waveguide region. Thus, the study of periodic potentials is central to this thesis, and so an introduction to the physics of these is important to remain as self-contained as possible.

In a periodic potential, the solution to the Schrödinger equation changes from being a plane wave to being of the form

$$\psi_{nk}(x) = u_{nk}(x)e^{ikx}, \tag{2.21}$$

where $u_{nk}(x)$ is a function with the same periodicity as the potential, k is the wavenumber, n indexes all remaining quantum numbers. This is known as Bloch's theorem, and the functions $u_{nk}(x)$ which form the basis as the Bloch functions.

This form of the solution leads to an interesting observation in reciprocal space. Translating by the reciprocal lattice vector of the potential Q, it can be seen that $\psi_{nk}(x) = \psi_{nk+Q}(x)$. This means that only momenta in the range $k \in [-Q/2, Q/2)$ are unique. This range of values is known as a Brillouin zone (abbreviated B.Z.).

Since the Bloch functions are periodic, they can be Fourier transformed allowing the Schrödinger equation to be solved in momentum space.

2.3.1 Continuous Potential

A powerful example is the case where a cosine wave potential is applied to the channel, for which the Hamiltonian is

$$H = \frac{p_x^2}{2m_x} + V\cos Qx, \tag{2.22}$$

where Q is the wavenumber and V is the amplitude of the of the periodic potential $V(x) = V\cos Qx$. The eigenvalues of this are then determined by expanding the wavefunction in the Fourier basis $\psi_k(x) = \sum_G u_k^G e^{i(k+G)x}$ where $G \in$

{set of all reciprocal lattice vectors}, to obtain

$$-\sum_G u_k^G \frac{\hbar^2 \partial_x^2}{2m_x} e^{i(k+G)x} + V \sum_G u_k^G \cos Qx e^{i(k+G)x} = E \sum_G u_k^G e^{i(k+G)x}. \tag{2.23}$$

The cosine is expanded as the sum of exponentials, and this is multiplied by a single exponential e^{-iRx}, before integrating with respect to x (exploiting orthogonality conditions) to obtain a series of equations for each k in the first Brillouin zone

$$u_k^G \left(E - \frac{\hbar^2 (k+G)^2}{2m_x} \right) - \frac{V}{2}(u_k^{G-Q} + u_k^{G+Q}) = 0, \tag{2.24}$$

which can then be written as a matrix with the block structure

$$\begin{pmatrix} E - t_k^{G+2Q} & -\frac{V}{2} & 0 & 0 & 0 \\ \frac{-V}{2} & E - t_k^{G+Q} & \frac{-V}{2} & 0 & 0 \\ 0 & -\frac{V}{2} & E - t_k^{G} & -\frac{V}{2} & 0 \\ 0 & 0 & -\frac{V}{2} & E - t_k^{G-Q} & -\frac{V}{2} \\ 0 & 0 & 0 & -\frac{V}{2} & E - t_k^{G-2Q} \end{pmatrix} \begin{pmatrix} u_k^{G+2Q} \\ u_k^{G+Q} \\ u_k^{G} \\ u_k^{G-Q} \\ u_k^{G-2Q} \end{pmatrix} = 0, \tag{2.25}$$

where $t_k^G = \hbar^2 (k+G)^2/(2m_x)$. This can be solved for the energy at individual values of quasimomentum k to generate the band structure in E, with the eigenvectors which make up the Bloch eigenfunctions. This derivation is presented more generally in [60], but here we study the specific case of a cosine potential for illustrative purposes - even with this simple case, the physics manifests strongly when the band structure is displayed.

Illustrated in Fig 2.7a is the effect of this periodic modulation on the band structure. The effect on the features far from the edge of the Brillouin zone is small. However, as the quasimomentum approaches the Brillouin zone edge at $k = \pm Q/2$,

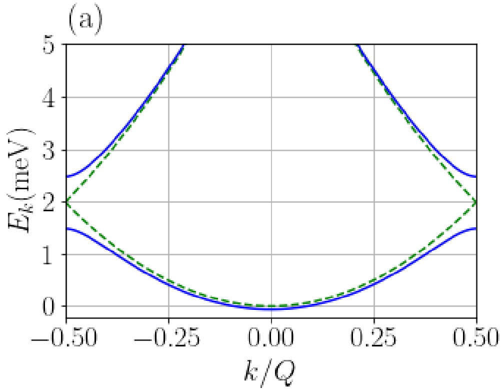

Figure 2.7: a) The effect of the periodic potential with $V = 1.0$ meV and $\lambda = 10$ nm on the band structure. Compared to the case with no potential (green dashed line), there is a gap opening at the edge of the Brillouin zone edge. b) Conductance corresponding to the band structure in (a). The gap in the band structure manifests as a gap in the conductance, which would result in a negative transconductance. $m = 1.9m_e$ in both (a) and (b).

the energy band flattens out until it reaches the B.Z. edge, where a band gap occurs. This feature of band gaps is present in all periodic systems. This will be illustrated for the Kronig-Penney model [61] in the next section, which is a minimal model of a periodic system which also includes a band gap at the Brillouin zone edge.

The question now becomes one of how the gaps in the band structure affect the transport. Using the method presented earlier, the conductance can be determined by determining the number of partially filled bands. When the Fermi energy lies inside a band, this is partially filled and contributes $2e^2/h$ to the transport. However, when the Fermi energy lies in the band gap formed by the potential, the conductance is zero due to the fact that there are no available states around the Fermi energy to populate - the band below is completely filled. This is displayed in Fig. 2.7b.

2.3.2 The Kronig-Penney Model

The Kronig-Penney model is a textbook example used to study the energetic properties of electrons in crystals. It is simple to understand and visualise, yet the physics manifests clearly and dramatically, capturing the introduction of band gaps into the spectrum. It was first presented in 1939 as an approximation to a lattice potential, and has become one of the most notable models in solid-state physics [61].

The Kronig-Penney model is essentially a series of square potential barriers with energy V_0, width d, and period λ, as presented in Fig. 2.8. This can describe a lattice potential in a crystal where the atomic nuclei form an infinite series of potential wells, which are approximated as rectangular. It is known what happens to electrons incident on a single square barrier (to recap, see Griffiths [62]). Here, we will see what changes when there are an infinite series of these. This derivation is adapted from Kittel [60].

We begin by dividing this into two regions: region I inside the barrier, and region II outside. The Hamiltonian is

$$H_I = \frac{p_x^2}{2m} + V(x), \tag{2.26}$$

with energy eigenvalue

$$E = \frac{\hbar^2 k_I^2}{2m} + V_0 \tag{2.27}$$

in region I, and

$$E = \frac{\hbar^2 k_{II}^2}{2m} \tag{2.28}$$

in region II. We use a plane wave ansatz for the wavefunction in each region, which

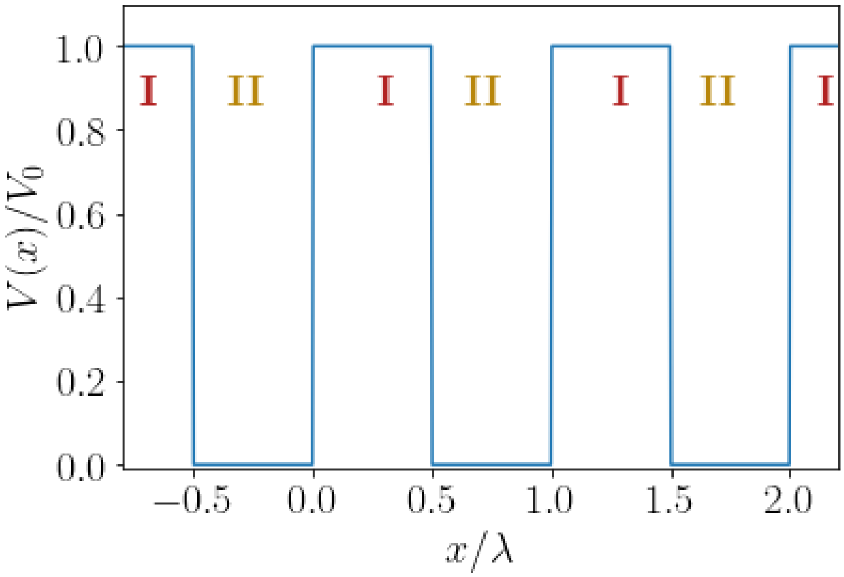

Figure 2.8: Kronig-Penney potential with x scaled by λ and $V(x)$ scaled by V_0, and barrier width d. Here, $\lambda = 2d$ has been chosen for illustrative purposes, but this is not a requirement.

is useful in one dimension as it allows the wavefunction to be split into left- and right-moving parts. These read

$$\psi_I(x) = Ae^{ik_I x} + Be^{-ik_I x} \tag{2.29}$$

in region I, and

$$\psi_{II}(x) = Ce^{ik_{II} x} + De^{-ik_{II} x} \tag{2.30}$$

in region II. The wavefunction and its derivative must be continuous at every point in space, and so these constraints give two equations at $x = 0$:

$$A + B = C + D, \tag{2.31}$$

and

$$k_I(A - B) = k_{II}(C - D). \tag{2.32}$$

However, there are four unknowns, and so far only two equations, so more constraints must be used to solve this model. Since the model describes an infinite periodic array of barriers, Bloch's theorem [63] can be applied to include the necessary extra constraints. Recall that Bloch's theorem states that a periodic potential ensures that the wavefunction is periodic with the same period as the potential. So, using the property

$$\psi(x + \lambda) = \psi(x)e^{ik\lambda}, \tag{2.33}$$

where k is the quasimomentum which will define the band structure, two more equations can be obtained (as this should also hold for the derivative): by looking at points $-d$ and $\lambda - d$, it holds that

$$Ae^{-ik_I d} + Be^{ik_I d} = \left[Ce^{ik_{II}(\lambda-d)} + De^{-ik_{II}(\lambda-d)}\right] e^{ik\lambda}, \tag{2.34}$$

and

$$k_I(Ae^{-ik_I d} - Be^{ik_I d}) = k_{II} \left[Ce^{ik_{II}(\lambda-d)} - De^{-ik_{II}(\lambda-d)}\right] e^{ik\lambda}. \tag{2.35}$$

Since there are four equations, the system can be solved. To do this, it is expressed as

$$\begin{pmatrix} 1 & 1 & -1 & -1 \\ kI & -k_I & -k_{II} & k_{II} \\ e^{-ik_I d} & e^{ik_I d} & -e^{ik_{II}(\lambda-d)}e^{ik\lambda} & -e^{-ik_{II}(\lambda-d)}e^{ik\lambda} \\ k_I e^{-ik_I d} & -k_I e^{ik_I d} & -k_{II}e^{ik_{II}(\lambda-d)}e^{ik\lambda} & k_{II}e^{-ik_{II}(\lambda-d)}e^{ik\lambda} \end{pmatrix} \begin{pmatrix} A \\ B \\ C \\ D \end{pmatrix} = 0. \tag{2.36}$$

This can be solved analytically, resulting in

$$\cos k\lambda = \cos k_I(\lambda - d)\cos k_{II}d - \frac{k_I^2 + k_{II}^2}{2k_I k_{II}} \sin k_I(\lambda - d)\sin k_{II}d, \tag{2.37}$$

where k_I and k_{II} are determined for a given energy by Eq. (2.27) and Eq. (2.29) respectively.

From this, a band structure can be derived by solving Eq. (2.37) for a given energy to determine the allowed k values. These can be real or complex, with real k values constituting allowable k values for electronic energy bands. The complex values of k are where no electronic states are available for transport, and correspond to band gaps.

Using the free electron mass, and parameters $\lambda = 20$nm, $d = \lambda/2$, and $V_0 =$ 0.5meV (chosen such that they are in the same regime as experimental parameters while most clearly highlighting the relevant physics), we analyse a band structure for the Kronig-Penney model in Fig. 2.9. First of all, this is the same physics as was seen in the previous section for a simple cosine wave potential. There is a slight shift in the energy, but the main feature is the band gap occuring at the Brillouin zone edge $k/Q = 0.5$, at around $E_k =$1meV. In a scattering model, the parameters of interest for transport are the transmission coefficients, which feed directly into the Landauer formula Eq. (2.10). The transmission coefficients go to zero in the band gap region (total reflection) due to interference between right- and left-moving waves.

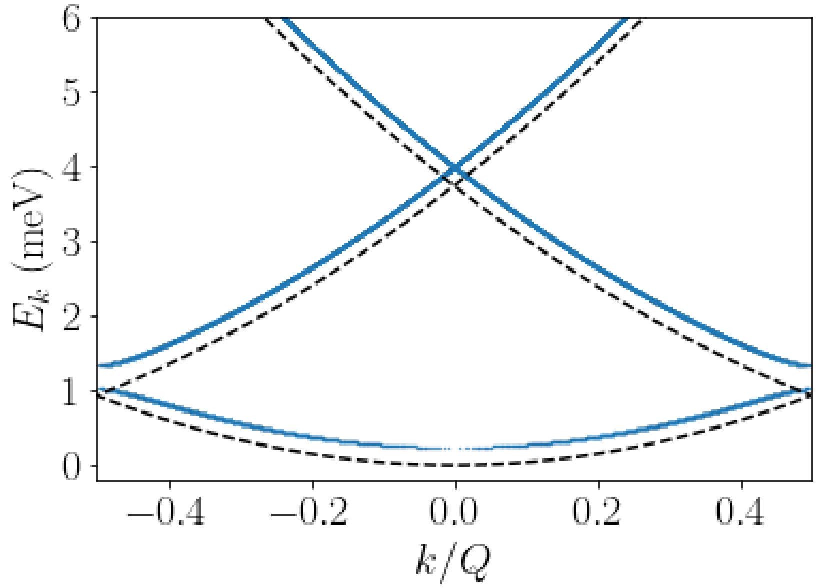

Figure 2.9: Band structure of the Kronig-Penney model for $\lambda = 20\text{nm}$, $d = \lambda/2$, and $V_0 = 0.5\text{meV}$ (blue), compared to the band structure of a free electron (black-dashed). The gap around $q = 0$ arises from the difficulty of sampling the infinite density of states around this point rather than being indicative of any physics.

2.4 Mean-Field Treatment Of Electron-Electron Interactions

As discussed in Sec. 1.2, there is strong evidence of electron-electron interactions in LAO/STO interfaces. As such, to model the behaviour of electrons in waveguides in these systems, an approach must be taken to include interactions in the waveguide Hamiltonian. To do this, the Hamiltonian is written in second quantization, introducing field operators

$$\Psi(x) = \begin{pmatrix} \Psi_\uparrow(x) \\ \Psi_\downarrow(x) \end{pmatrix} = \frac{1}{\sqrt{L}} \sum_k e^{ikx} \begin{pmatrix} c_{k\uparrow} \\ c_{k\downarrow} \end{pmatrix}, \tag{2.38}$$

where $c^\dagger_{k\sigma}$ is an operator that creates an electron with wavenumber k and spin σ. These operators have the anticommutation relations $\left\{c_{k,\sigma}, c^\dagger_{q,\tau}\right\} = \delta_{\sigma\tau}\delta(k-q)$ and $\{c_{k,\sigma}, c_{q,\tau}\} = \left\{c^\dagger_{k,\sigma}, c^\dagger_{q,\tau}\right\} = 0$. To determine the interacting behaviour of the system, it is necessary to include every electronic state available. This is done by integrating over all of the available electron states, which leads to the many-body Hamiltonian

$$\mathcal{H} = \int \mathrm{d}x \Psi^\dagger(x) H \Psi(x), \tag{2.39}$$

for the single electron Hamiltonian H.

Inserting Eq. (2.38) into this for a Hamiltonian with no spin-orbit coupling results in

$$\mathcal{H} = \sum_k \epsilon_{k\sigma} c^\dagger_{k\sigma} c_{k\sigma} = \sum_k \begin{pmatrix} c^\dagger_{k\uparrow} & c^\dagger_{k\downarrow} \end{pmatrix} \mathcal{H}_k \begin{pmatrix} c_{k\uparrow} \\ c_{k\downarrow} \end{pmatrix}, \tag{2.40}$$

where the $\epsilon_{k\sigma}$ are the eigenvalues of the Hamiltonian corresponding to a state with momentum k and spin σ, and

$$\mathcal{H}_k = \begin{pmatrix} \epsilon_{k\uparrow} & 0 \\ 0 & \epsilon_{k\downarrow} \end{pmatrix}. \tag{2.41}$$

There are various ways to treat interactions using these tools. One method for illustrative purposes is the contact interaction between electrons of different spins. In practice, a contact interaction is most commonly used when dealing with cold atoms, and electron-electron interactions in materials are often more complicated than this, and depend on the material. However, since the nature of the interaction in LAO/STO is still an active topic of research, we take a contact interaction as a first model. This is written as [64]

$$\mathcal{H}_I = U \int \mathrm{d}x \Psi^\dagger_\uparrow(x)\Psi^\dagger_\downarrow(x)\Psi_\downarrow(x)\Psi_\uparrow(x). \tag{2.42}$$

Since Eq. (2.42) is quartic in the field operators, it cannot be diagonalised exactly. Thus, the interactions are treated using a technique called mean field theory. This approach supposes that operators have some mean value, and they do not vary much from this value. Mathematically, this can be stated as $\hat{A} = \langle\hat{A}\rangle + \delta\hat{A}$, where $\langle\hat{A}\rangle$ is the expectation value of the operator, and $\delta\hat{A}$ describes small fluctuations around this expectation value. The problem is made tractable by studying pairs of operators, resulting in

$$\hat{A}\hat{B} \approx (\langle\hat{A}\rangle + \delta\hat{A})(\langle\hat{B}\rangle + \delta\hat{B}) = \langle\hat{A}\rangle\langle\hat{B}\rangle + \delta\hat{A}\langle\hat{B}\rangle + \delta\hat{B}\langle\hat{A}\rangle + \delta\hat{A}\delta\hat{B}.$$

Since $\delta\hat{A}$ and $\delta\hat{B}$ are small, the product of these is extremely small, so this is neglected. Rearranging the mean-field expansion for the fluctuations to $\delta\hat{A} = \hat{A} - \langle\hat{A}\rangle$ and reinserting this obtains

$$\hat{A}\hat{B} \approx \hat{A}\langle\hat{B}\rangle + \hat{B}\langle\hat{A}\rangle - \langle\hat{A}\rangle\langle\hat{B}\rangle.$$

The third term here is a number, and corresponds to an energy shift in the Hamiltonian but has no effect on the physics, so this is neglected for now, giving

$$\hat{A}\hat{B} \approx \hat{A}\langle\hat{B}\rangle + \hat{B}\langle\hat{A}\rangle. \tag{2.43}$$

Eq. (2.43) describes the mean-field decomposition of pairs of operators. Applying this to Eq. (2.42), if operators are grouped into pairs and applied to this formalism, the contact interaction can be made quadratic by enclosing two of the four operators in each term in an expectation value and turning them into a number.

Mean-field theory works best for weak interactions and high dimensions $d \geq 2$. However, even in one-dimension, provided the interaction energy is kept low compared to the other energy scales of the system, it can be used to determine the nature of electronic interactions. However, the fluctuations around these mean values tend to be quite large in one-dimension, meaning it is not as useful in making quantitative predictions.

Performing a mean-field decomposition over all pairs of operators leads to

$$\begin{aligned}\Psi_\uparrow^\dagger\Psi_\downarrow^\dagger\Psi_\downarrow\Psi_\uparrow \approx & \Psi_\uparrow^\dagger\Psi_\downarrow^\dagger\langle\Psi_\downarrow\Psi_\uparrow\rangle + \Psi_\downarrow\Psi_\uparrow\langle\Psi_\uparrow^\dagger\Psi_\downarrow^\dagger\rangle \\ & -\Psi_\uparrow^\dagger\Psi_\downarrow\langle\Psi_\downarrow^\dagger\Psi_\uparrow\rangle - \Psi_\downarrow^\dagger\Psi_\uparrow\langle\Psi_\uparrow^\dagger\Psi_\downarrow\rangle \\ & +\Psi_\uparrow^\dagger\Psi_\uparrow\langle\Psi_\downarrow^\dagger\Psi_\downarrow\rangle + \Psi_\downarrow^\dagger\Psi_\downarrow\langle\Psi_\uparrow^\dagger\Psi_\uparrow\rangle,\end{aligned} \tag{2.44}$$

where $\langle\cdot\rangle\langle\cdot\rangle$ terms are neglected as they just contribute a shift in the zero of energy. The above expression contains three types of terms

1. Terms like $\langle\Psi_\uparrow^\dagger\Psi_\uparrow\rangle$. These are known as the Hartree terms, and shift the zero of energy of the spectrum.

2. Terms like $\langle\Psi_\uparrow^\dagger\Psi_\downarrow\rangle$. These are known as the Fock terms, and are responsible for spin-exchange interactions. These are zero without a term to mediate this process.

3. Terms like $\langle\Psi_\uparrow^\dagger\Psi_\downarrow^\dagger\rangle$. These are the Bogoliubov terms, and are responsible for electron pairing. They correspond to the expectation values of creating (or annihilating) an electron pair. In higher dimensions, this would be associated with superconductivity, but in 1D this association cannot be made.

It is these three types of terms that give the name to the method of solving the system used: the Hartree-Fock-Bogoliubov self-consistent mean-field approach.

The Hartree terms are denoted by $\Sigma_\sigma = U\langle\Psi^\dagger_{-\sigma}\Psi_{-\sigma}\rangle$, Fock by $\chi = U\langle\Psi_\downarrow^\dagger\Psi_\uparrow\rangle$ and Bogoliubov by $\Delta = U\langle\Psi_\downarrow\Psi_\uparrow\rangle$ to write Eq. 2.42 using Eq. (2.44) and Eq. (2.38) as

$$\mathcal{H}_I = \sum_k \Sigma_\uparrow c_{k\uparrow}^\dagger c_{k\uparrow} + \Sigma_\downarrow c_{k\downarrow}^\dagger c_{k\downarrow} - \chi c_{k\uparrow}^\dagger c_{k\downarrow} - \chi^* c_{k\downarrow}^\dagger c_{k\uparrow} + \Delta c_{k\uparrow}^\dagger c_{-k\downarrow}^\dagger + \Delta^* c_{k\downarrow} c_{-k\uparrow}. \quad (2.45)$$

For illustrative purposes, the effects of the Hartree and Fock terms can be neglected to focus solely on the pairing term (though in Ch. 3 and Ch. 4, these will be reintroduced as they become relevant to the physics), which is assumed to be real. Additionally, looking at the zero spin-orbit and magnetic field case, $\epsilon_{k\sigma} = \frac{\hbar^2 k^2}{2m} - \mu_{SG} \equiv \xi_k$, the total Hamiltonian is

$$\mathcal{H} = \sum_{k} \sum_{\sigma} \xi_k c^{\dagger}_{k\sigma} c_{k\sigma} + \Delta(c^{\dagger}_{k\uparrow} c^{\dagger}_{-k\downarrow} - c_{k\uparrow} c_{-k\downarrow}). \tag{2.46}$$

Throughout the text, we solve these models in two ways: the first, for Hamiltonians that can be written as 2×2 matrices in some basis, an analytical treatment can be performed. However, this becomes much harder to do in moving to larger bases, and so numerical methods must be used. This shall be introduced at the end of the section.

For both analytical and numerical methods, a Bogoliubov transformation is used [65] to write the Hamiltonian as

$$\mathcal{H} = \sum_{k} \begin{pmatrix} c^{\dagger}_{k\uparrow} & c_{-k\downarrow} \end{pmatrix} \begin{pmatrix} \xi_k & \Delta \\ \Delta & -\xi_{-k} \end{pmatrix} \begin{pmatrix} c_{k\uparrow} \\ c^{\dagger}_{-k\downarrow} \end{pmatrix} = \sum_{k} \vec{c_k}^{\dagger} H_k \vec{c_k}, \tag{2.47}$$

where the basis vector is $\vec{c_k} = (c_{k\uparrow}, c^{\dagger}_{-k\downarrow})$. This is diagonalised by inserting copies of $U_k U_k^{\dagger} = \mathbb{I}$ as

$$\mathcal{H} = \sum_{k} \vec{c_k}^{\dagger} U_k U_k^{\dagger} H_k U_k U_k^{\dagger} \vec{c_k} = \sum_{k} \vec{c_k}^{\dagger} U_k E_k U_k^{\dagger} \vec{c_k}, \tag{2.48}$$

where E_k is a diagonal matrix containing the eigenvalues of H_k. From this, the Bogoliubov transformation is defined as $\vec{\gamma_k} = U_k^{\dagger} \vec{c_k}$ and the Hamiltonian becomes

$$\mathcal{H} = \sum_{k\sigma} E_{k\sigma} \gamma^{\dagger}_{k\sigma} \gamma_{k\sigma}. \tag{2.49}$$

The Hamiltonian can be diagonalised to obtain the energies $E_{k\sigma} = \sqrt{\xi_k^2 + \Delta^2}$, which is minimal at $E_{k\sigma} = |\Delta|$, which is why Δ is given the name "pairing gap" - even at the Fermi energy the excitation spectrum has non-zero energy gap for finite Δ. Physically, this is the energy associated to breaking an electron pair, meaning that the ground state of the system in this configuration is a paired state.

However, $\Delta = U\langle\Psi_\downarrow\Psi_\uparrow\rangle = U\sum_{kk'} e^{i(k+k')x}\langle c_{k\prime\downarrow}c_{k\uparrow}\rangle$, and for a homogeneous system, this should be constant as a function of x, reducing to

$$\Delta = U\sum_k \langle c_{-k\downarrow}c_{k\uparrow}\rangle. \tag{2.50}$$

To calculate this, the Bogoliubov transformation is inverted to obtain

$$\begin{pmatrix} c_{k\uparrow} \\ c^\dagger_{-k\downarrow} \end{pmatrix} = U_k \begin{pmatrix} \gamma_{k\uparrow} \\ \gamma^\dagger_{-k\downarrow} \end{pmatrix}. \tag{2.51}$$

For this system, the properties of the SU(2) group can be exploited to write this as

$$c_{k\uparrow} = u_k^*\gamma_{k\uparrow} + v_k\gamma^\dagger_{-k\downarrow} \tag{2.52}$$

and

$$c^\dagger_{-k\downarrow} = -v_k^*\gamma_{k\uparrow} + u_k\gamma^\dagger_{-k\downarrow}, \tag{2.53}$$

allowing the Hamiltonian to be rewritten as

$$\begin{aligned}\mathcal{H} =& \sum_k \left[\xi_k(|u_k|^2 - |v_k|^2]) - \Delta(u_k v_k^* + u_k^* v_k)\right] (\gamma_{k\uparrow}^\dagger \gamma_{k\uparrow} + \gamma_{\downarrow-k}^\dagger \gamma_{\downarrow-k}) \\ &+ \sum_k \left[(2\xi_k u_k v_k + \Delta(u_k^2 - v_k^2)\right] \gamma_{k\uparrow}^\dagger \gamma_{-k\downarrow}^\dagger \\ &+ \sum_k \left[(2\xi_k u_k^* v_k^* + \Delta(u_k^{*2} - v_k^{*2})\right] \gamma_{-k\downarrow} \gamma_{k\uparrow}.\end{aligned} \tag{2.54}$$

In order for this to be diagonalised, the terms proportional to $\gamma_{k\uparrow}^\dagger \gamma_{-k\downarrow}^\dagger$ and $\gamma_{-k\downarrow}\gamma_{k\uparrow}$ must vanish resulting in the polynomial $2\xi_k u_k v_k + \Delta(u_k^2 - v_k^2) = 0$, which is solved for the ratio v_k/u_k as

$$2\xi_k u_k v_k + \Delta(u_k^2 - v_k^2) = 0 \implies \frac{v_k}{u_k} = \frac{\xi_k \pm \sqrt{\xi_k^2 + \Delta^2}}{\Delta}. \tag{2.55}$$

Taking the negative root to minimize the absolute value, using $|u_k|^2$ and $|v_k|^2$ and the normalization $|u_k|^2 + |v_k|^2 = 1$, $|u_k|^2$ and $|v_k|^2$ can be determined as

$$|u_k|^2 = \frac{|u_k|^2}{|u_k|^2 + |v_k|^2} = \frac{1}{1 + \left|\frac{v_k}{u_k}\right|^2} = \frac{1}{2}\left(1 + \frac{\xi_k}{\sqrt{\xi_k^2 + \Delta^2}}\right) \tag{2.56}$$

and

$$|v_k|^2 = \frac{1}{2}\left(1 - \frac{\xi_k}{\sqrt{\xi_k^2 + \Delta^2}}\right). \tag{2.57}$$

The quasiparticles follow a thermal distribution, meaning that $\langle \gamma_{kj}^\dagger \gamma_{kj'} \rangle = n_f(E_k)\delta_{jj'}$, $\langle \gamma_{kj}\gamma_{kj'} \rangle = \langle \gamma_{kj}^\dagger \gamma_{kj'}^\dagger \rangle = 0$. The gap equation Eq. (2.50) then becomes

$$\Delta = -U \sum_k u_k^* v_k (n_f(E_{k\uparrow}) + n_f(E_{k\downarrow}) - 1), \tag{2.58}$$

which can be rewritten as

$$1 = -\frac{U}{2}\sum_k \frac{2n_f(E_k) - 1}{\sqrt{\xi_k^2 + \Delta^2}}. \tag{2.59}$$

This form shows that Δ depends on the spectrum of the system, but the spectrum is in turn proportional to Δ. While more could be done by converting to an integral and assuming zero temperature, this is most easily solved numerically through a self-consistent approach.

The idea is as follows:

1. Begin with an initial trial value of Δ, call it Δ_0.
2. Diagonalize the Hamiltonian in Eq. (2.47) to find the eigenvalues and eigenvectors with $\Delta = \Delta_0$.
3. Determine the value of Δ that is given by Eq. (2.59) (or Eq. (2.50) in a more general case where a simplified gap equation is less easy to obtain), call it Δ_1.
4. Calculate the difference $|\Delta_1 - \Delta_0|$. If this is less than some specified precision ϵ, then the numerical simulation has converged and $\Delta = \Delta_1$ is the final gap.
5. If $|\Delta_1 - \Delta_0| > \epsilon$, then repeat 1-4 until convergence, with Δ_1 becoming the new Δ_0.

This scheme is how the strength of pairing is determined in the systems of interest. In practice, the precision ϵ is on the order of the energy of thermal fluctuations. At the minimum temperature of 25 mK, this is around 0.001 meV. This method shall be presented in the following chapter, and utilised in all of the interacting calculations performed in the later chapters of the thesis.

2.5 Summary

This chapter began with a general overview on quantum transport and introducing conductance. Following this, two single-electron effects on the conductance were introduced - Rashba spin-orbit coupling, and periodic modulations - and their effects on the conductance were explained. Finally, a treatment of electron-electron interactions was discussed. All of these will be utilised in Ch. 4 and Ch. 5 where we will study in detail the conductance of interacting periodically modulated waveguides.

Chapter 3

Electron Waveguides Without Modulation

Before presenting the material on modulated electron waveguides that forms the main body of the thesis, it is helpful to show the unmodulated effects. This is both to clearly show the techniques used and how they translate into results, but also for a foundation as to what can be expected from the conductance and transconductance behaviour in these systems, to study how they change when including the effects of modulation. To that end, this short chapter discusses the straight waveguide. This is mostly based on recalculating the results of previous work [22], with some additional insights from further study of these systems.

3.1 Single Electron Physics

In this section, we will derive the basic energy spectrum for an electron in a non-interacting waveguide, based on [16]. The standard waveguide model involves electrons propagating "nearly free" along the waveguide direction (x in this work) and harmonically confined along the transverse directions y and z.

By introducing a magnetic field $\vec{B} = (0, 0, B)$ into the waveguide, the physical momentum of the electrons in the system is shifted by the Lorentz force according to $\vec{p} \to \vec{\Pi} = \vec{p} + e\vec{A}$ where $\vec{\Pi}$ is the physical momentum, $\vec{p}$ is the canonical momentum, and $\vec{A}$ is the vector potential. There exists a gauge freedom, as $\vec{B} = \vec{\nabla} \times \vec{A}$. To solve the 1D waveguide model, the simplest choice is $\vec{A} = (-By, 0, 0)$. Thus, the Hamiltonian of the waveguide becomes

$$H = \frac{(p_x - eBy)^2}{2m_x} + \frac{p_y^2}{2m_y} + \frac{p_z^2}{2m_z} + \frac{m_y}{2}\omega_y^2 y^2 + \frac{m_z}{2}\omega_z^2 z^2 - \frac{g\mu_B}{2} B\sigma_z. \tag{3.1}$$

Since $[H, p_x] = 0$, we can again work with simultaneous eigenstates of H and p_x and replace p_x its eigenvalue $\hbar k$. Introducing the cyclotron frequency $\omega_c = eB/\sqrt{m_x m_y}$ and centre of motion $y_0 = eB/\hbar k$, the Hamiltonian becomes

$$H = \left(1 - \frac{\omega_c^2}{\Omega^2}\right) \frac{\hbar^2 k^2}{2m_x} + \frac{p_y^2}{2m_y} + \frac{m_y}{2}\Omega^2 \left(y - \bar{y}_0\right)^2 + \frac{p_z^2}{2m_z} + \frac{m_z}{2}\omega_z^2 z^2 - \frac{g\mu_B}{2} B\sigma_z, \tag{3.2}$$

where $\bar{y}_0 = (\omega_c/\Omega)^2 y_0$ and $\Omega = \sqrt{\omega_c^2 + \omega_y^2}$. Now, recognising the harmonic confinements along y and z, the eigenenergies can be calculated as

$$E(k, n_y, n_z, \sigma) = \left(1 - \frac{\omega_c^2}{\Omega^2}\right) \frac{\hbar^2 k^2}{2m_x} + \hbar\Omega \left(n_y + \frac{1}{2}\right) + \hbar\omega_z \left(n_z + \frac{1}{2}\right) - \frac{g\mu_B}{2} B\sigma, \tag{3.3}$$

which correspond to separable eigenfunctions of the form

$$\psi(k, n_y, n_z, \sigma) = \langle x, y, z | k, n_x, n_y, \sigma\rangle = e^{ikx} \phi_{n_y}(y - \bar{y}_0) \phi_{n_z}(z) \left|\sigma\right\rangle.$$

The inclusion of the magnetic field into the basic waveguide model makes three changes to the energies: Firstly, it lifts the spin-degeneracy via the Zeeman term -

this causes spin-up to become more energetically favourable. Secondly, it increases the y-confinement frequency Ω, which shifts apart the energy levels along y. Finally, it flattens out the kinetic term by decreasing the prefactor $1 - \frac{\omega_c^2}{\Omega^2}$.

In LAO/STO interfaces, the z-trapping is best modelled by a half-harmonic oscillator rather than a harmonic oscillator as used above. A half-harmonic oscillator is characterised by a potential

$$V(x) = \begin{cases} \frac{m_z}{2}\omega_z^2 z^2 & z > 0 \\ \infty & z < 0. \end{cases}$$

This is due to the fact that the potential is infinite on one half of the well due to the inability of electrons to penetrate into the material (since the LAO layer is three layers thick, this amounts to only ∼1nm, far less than the relevant widths, and so the electron wavefunction must end before this). The effect of this is to only allow odd harmonic modes, as the presence of nodes at $z = 0$ allows the wavefunction to be continuous.

Throughout the thesis, $\omega_y \ll \omega_z$. However, magnetic fields can be tuned as high as 16T in the experiment, at which point the increase in confinement energy is larger than the increase in Zeeman energy. In the large field limit, the energy of both spins increases, but more rapidly for spin-up. So in these quasi 1D waveguides, the spin-splitting is not a straight-forward linear relationship of the spin-dependent energies as a function of magnetic field. This is displayed in Fig. 3.1 a.

Additionally at high fields, the lowest energy excited state is $|k, 0, 1, \sigma\rangle$, as shown in Fig. 3.1 b where $|k, 1, 0, \uparrow\rangle$ and $|k, 0, 1 \uparrow\rangle$ cross between $B = 5$ T and $B = 6$ T. At these magnetic fields, the kinetic term is also heavily suppressed, with the prefactor $\left(1 - \frac{\omega_c^2}{\Omega^2}\right) \sim 10^{-3}$.

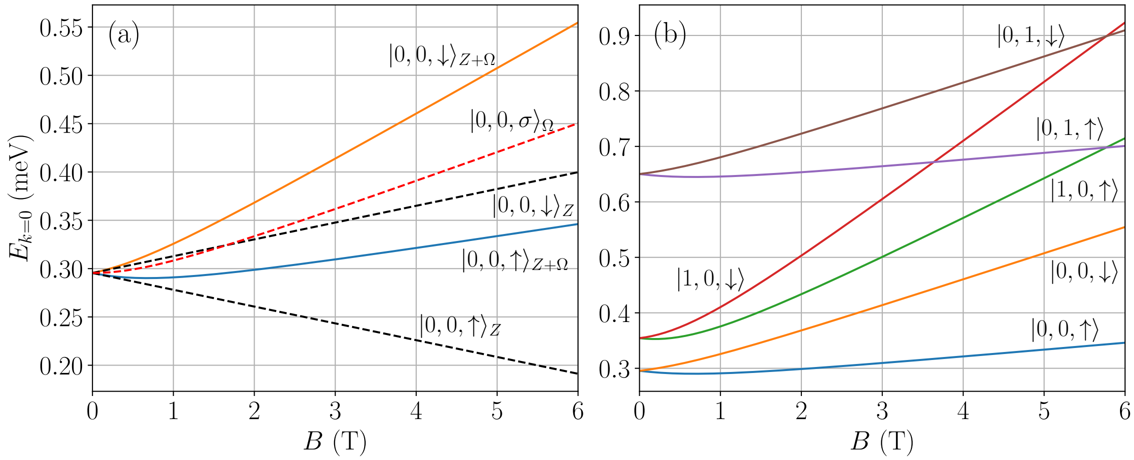

Figure 3.1: (a) Plots of the $k = 0$ energy of each band as a function of magnetic field with both the magnetic field dependence on the trapping frequency Ω and the Zeeman shift, showing the deviation of the spectrum from simply the Zeeman split case and the case with only the effect on the trapping, with σ taking the place of a spin labelling here due to the spin-degeneracy of the Lorentz force. This corresponds to the minimum energy as a function of k of the band. The subscripts on the kets refer to the terms included, with Ω denoting lines with the effect of the confinement increase included, and Z denoting terms with the Zeeman shift included. (b) The minimum energies of various bands as a function of magnetic field, displayed to show the crossing of two bands at finite magnetic fields. The labeling of the bands is in the form $|n_y, n_z, \sigma\rangle$. Parameters used are $m_x = m_y = 1.9m_e$, $m_z = 6.5m_e$, $l_y = 26$ nm, $l_z = 8.1$ nm, and $g = 0.6$.

3.2 Conductance spectrum Of Unmodulated Waveguides

All of the information presented above culminates in non-interacting conductance and transconductance spectra. The waveguide model describes quantised conductance in units of e^2/h, with each eigenstate $|n_y, n_z, \sigma\rangle$ contributing an additional transport channel and thus e^2/h conductance. The spectrum can then be temperature broadened according to [1] via

$$G(\mu_{SG}) = \int \mathrm{d}E G_{T=0}(\mu_{SG}) F_T(E - \mu_{SG}), \tag{3.4}$$

where

$$F_T(E) = \frac{\partial n_f(E)}{\partial E} = \frac{1}{4k_BT}\,\mathrm{sech}^2\left(\frac{E}{2k_BT}\right)$$

is the thermal broadening function.

To compare to experimental results, we introduce a new quantity called the *transconductance* F. This is defined as the derivative of the conductance with respect to the chemical potential μ_{SG} in the system, or

$$F = \frac{\mathrm{d}G}{\mathrm{d}\mu_{SG}}. \tag{3.5}$$

Intuitively, this quantity can be used to show the positions of the bands in the system in a similar way to the conductance calculations presented in Fig. 3.1. However, this quantity is routinely measured in experiment, making it an excellent way to visualise the spectrum of these waveguides.

In Fig. 3.2, the conductance spectrum in the (B, μ_{SG}) parameter space is displayed before (a) and after (b) broadening with the Fermi distribution at $k_BT =$ 50mK. The quantized conductance steps can be cleanly seen in both cases, while in the broadened case the steps are smoothed. This is additionally displayed in Fig. 3.3, where we show line cuts of these conductance plots at various magnetic fields, at both $T = 0$ mK and $T = 50$ mK. This illustrates well the smoothing effect that a finite temperature has on the conductance features of the system. In Fig. 3.2c, we then show transconductance of the broadened spectrum in Fig. 3.2b. In transconductance plots, a step up in conductance is represented as a strong peak at the given (B,μ_{SG}) configuration. As discussed in Ch. 1, the LAO/STO devices that inspired the work offer the ability to tune the chemical potential in the waveguides using a side gate, making this prospect possible to physically realise.

In [22], it is shown that clean 1D transport features can be observed in experi-

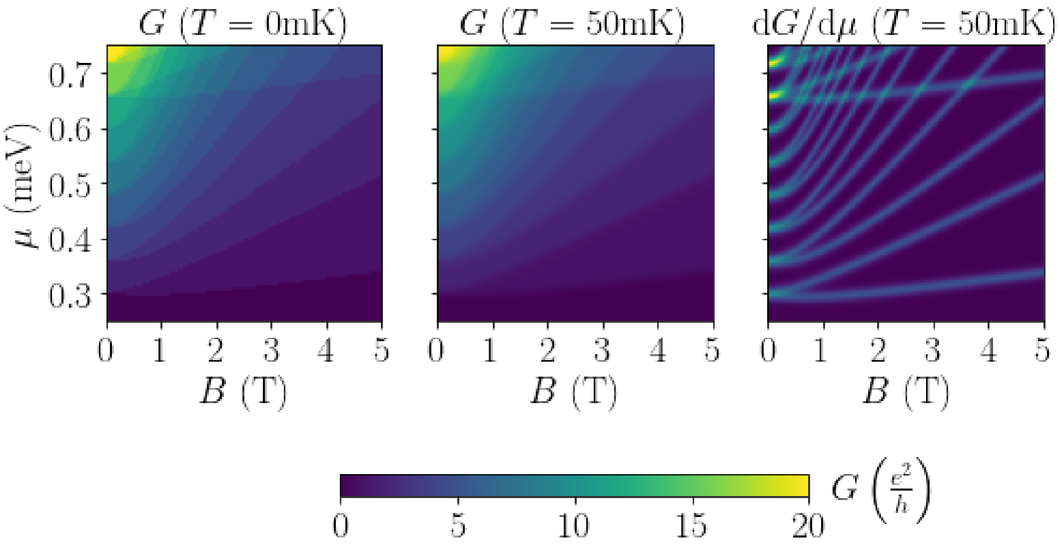

Figure 3.2: Conductances and transconductances for the straight waveguide as a function of B and μ_{SG}. (a) Unbroadened conductance spectrum of the straight waveguide as described by the above set of parameters. (b) Same conductance spectrum broadened by a 50mK Fermi distribution which accounts for thermal effects. (c) Transconductance spectrum obtained by taking the derivative with respect to $\mu_S G$ of (b). Parameters used are $m_x = m_y = 1.9m_e$, $m_z = 6.5m_e$, $l_y = 26$ nm, $l_z = 8.1$ nm, and $g = 0.6$.

ment and are described well by this model. Their results are displayed in Fig. 3.4. They compare transconductance measured for one of these devices as a function of magnetic field B and chemical potential μ_{SG} with the model as described in the previous section with those same parameters. A 65μeV Lorentzian has been used to broaden the peaks in the theoretical model to match with the widths obtained by those in the experiment. In regions with large separation between the bands, the waveguide model provides an excellent description of the transport physics.

Cleanly shown is the subband structure of the waveguide. Each peak in the transconductance spectrum can be associated to a transverse mode and spin by comparing to the waveguide model. For example, the lowest two bands are the $|0, 0, \uparrow\rangle$ and $|0, 0, \downarrow\rangle$. The parameters utilised here are fitted using the experimentally-

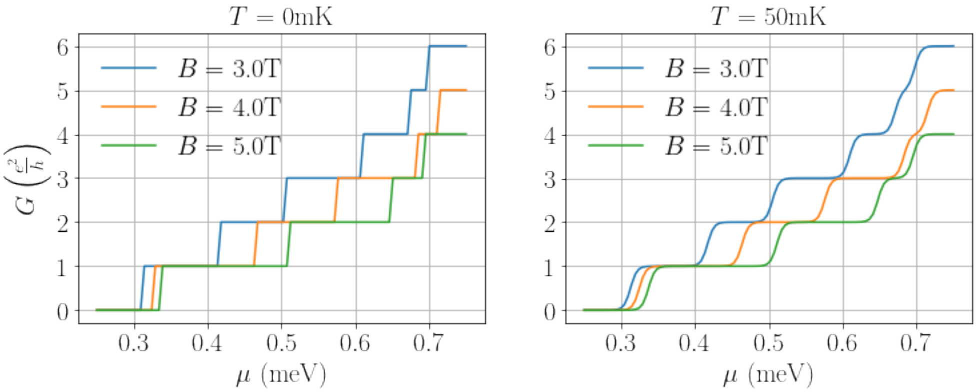

Figure 3.3: Line cuts of the conductance corresponding to (a) and (b) of Fig. 3.2 respectively, showing cleanly the conductance plateaux. Parameters used are $m_x = m_y = 1.9m_e$, $m_z = 6.5m_e$, $l_y = 26$ nm, $l_z = 8.1$ nm, and $g = 0.6$.

obtained conductance features at both zero-bias and finite bias, which is demonstrated in the supplementary material of [22].

In regions where the bands are close together, this model appears to break down. This is due to the strong interactions which are known to be present in LAO/STO [9]. These will be discussed in the following section. For now, we will focus on the regions where the single electron model provides an excellent description of the physics.

One complicating factor is that this model has a large number of free parameters which drastically affect the physics and depend on the details of the material properties which are not well-known ab-initio. These are the effective masses m_x, m_y, and m_z, the trapping widths l_y and l_z, and the Lande g-factor g. Thus, before proceeding, it may be useful to map out the effects of these at this stage before introducing more complicating factors. For clarity, only the two lowest energy trapping states of each mode are plotted.

Firstly, in the top row of Fig. 3.5 we vary the effective mass along the propagation direction m_x. Since the energy bands appear at $k = 0$, the kinetic energy term is

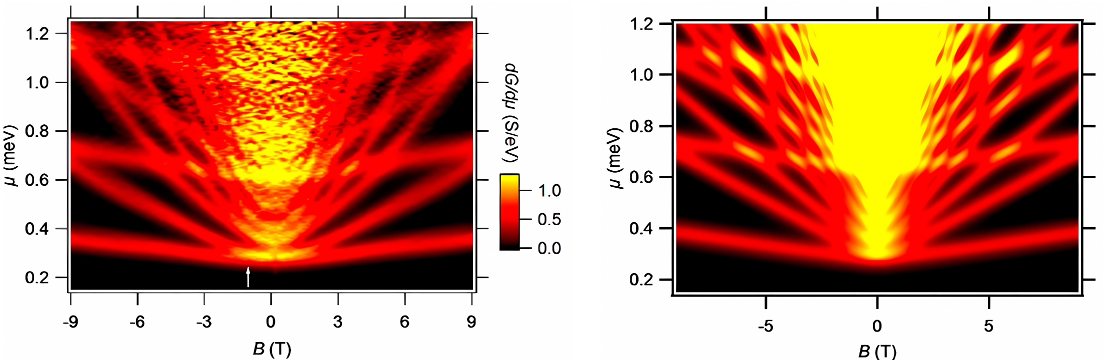

Figure 3.4: Plots of the transconductance of a straight waveguide, as published in [22]. a) Experimental transconductance measurements broadened by a 65meV Lorentzian from one of their devices. b) Theoretical transconductance calculations with the above parameters fitted to closely match the spectrum. Adapted with permission from Anil Annadi, Guanglei Cheng, Hyungwoo Lee, Jung-Woo Lee, Shicheng Lu, Anthony Tylan-Tyler, Megan Briggeman, Michelle Tomczyk, Mengchen Huang, David Pekker, Chang-Beom Eom, Patrick Irvin, and Jeremy Levy: *Quantized Ballistic Transport of Electrons and Electron Pairs in* $LaAlO_3/SrTiO_3$ *Nanowires* ,Nano Letters 2018 18 (7), 4473-4481. Copyright 2022 American Chemical Society.

unchanged by the change in effective mass. However, what is changed is the cyclotron frequency $\omega_c = eB/\sqrt{m_x m_y}$. As such, increasing this flattens out the spectrum by decreasing the effective confinement frequency as a function of magnetic field B.

In the middle row of Fig 3.5 we now vary the effective mass along the in-plane lateral direction. Since the surface properties of LAO/STO are the same along x and y, it would be expected that these two have similar effective masses, but the effect of this can be studied numerically without the constraint. Similarly to the top row of Fig. 3.5, the effective confinement frequency is modified by ω_c. However, since the $B = 0$ confinement frequency is given by $\omega_y = \hbar/(m_y l_y^2)$, increasing the effective mass also decreases the $B = 0$ confinement frequency, bringing the y-bands closer together as can be seen in the figure.

Finally, in the bottom row of Fig. 3.5 we vary m_z, the out-of-plane effective mass of the electrons. This only enters into the Hamiltonian in the term $\omega_z = \hbar/(m_z l_z^2)$ and so the effect of this term is to lower the energy of the z-bands, since ω_z is

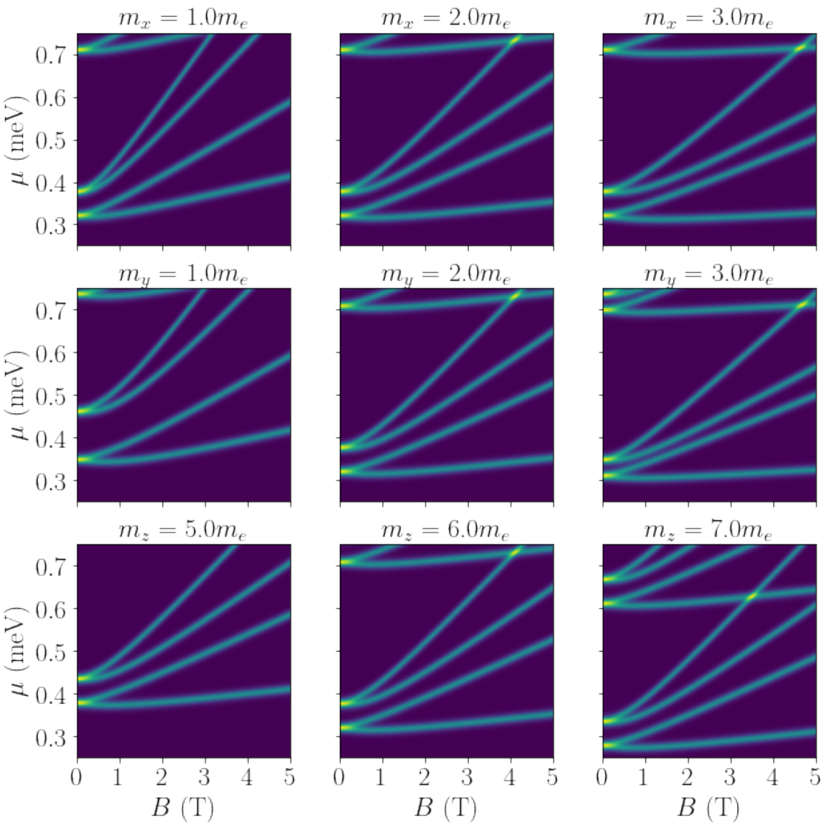

Figure 3.5: Transconductance as a function of magnetic field B and chemical potential μ_{SG} at $T = 50$mK for various values of m_x (top row), m_y (middle row) and m_z (bottom row). Default values are $m_x = 1.9m_e$, $m_y = 1.9m_e$, and $m_z = 6.5m_e$. Other parameters used are $l_y = 26$ nm, $l_z = 8.1$ nm, and $g = 0.6$.

inversely proportional to m_z.

In the top row of Fig. 3.6, we vary the trapping length along y, denoted l_y. This shares the closening and lowering of the y band energies with the effects of m_y, but since l_y only appears in the term $\omega_y = \hbar/(m_y l_y^2)$, it does not affect higher magnetic fields differently. Additionally, the bottom row of Fig. 3.6 which displays the effect of increasing the z trapping length l_z shows similar behaviour to the effect of increasing m_z, since they only appear in the same term.

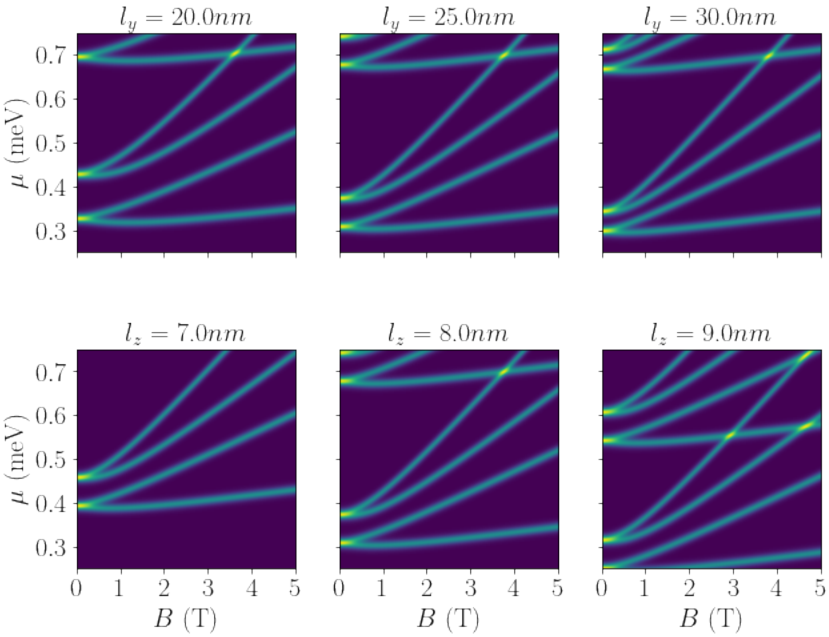

Figure 3.6: Transconductance as a function of magnetic field B and chemical potential μ_{SG} at $T = 50$ mK for various values of l_y (top row) and l_z (bottom row). Default values are $l_y = 26$ nm and $l_z = 8.1$ nm. Other parameters used are $m_x = m_y = 1.9m_e$, $m_z = 6.5m_e$, and $g = 0.6$.

Finally, we study the effect of changing the Lande g-factor, g, which is displayed in Fig. 3.7. This enters the Hamiltonian through the Zeeman term $g\mu_B/2B\sigma_z$. As expected, increasing the strength of this term leads to an increase in the splitting between the spin-subbands and thus the gradient of the transconductance peaks as a function of B.

3.3 Pairing Effects In Unmodulated waveguides

However, the above analysis does not tell the whole story. In regions where multiple bands would cross, bands with opposite spins are drawn closer together, and bands with same spins repel each other, which can be seen in Fig. 3.4. This is not described by single particle physics, a fact which is unsurprising given that it occurs only when

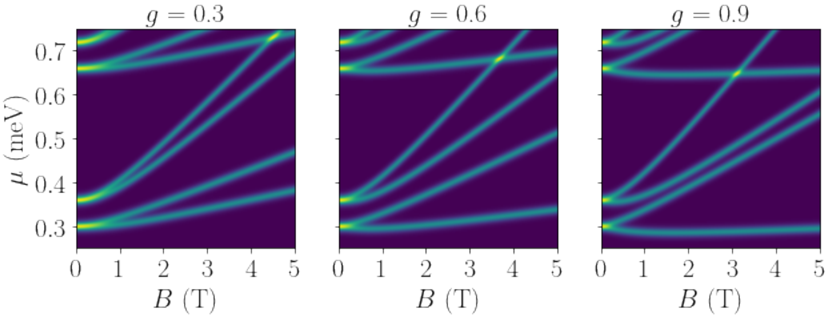

Figure 3.7: Transconductance as a function of magnetic field B and chemical potential μ_{SG} at $T = 50$ mK for various values of g. Other parameters used are $m_x = m_y = 1.9m_e$, $m_z = 6.5m_e$, $l_y = 26$ nm, and $l_z = 8.1$ nm.

two electrons have similar energies. It suggests the presence of electron-electron interactions.

Electron-electron interactions are well known to be present in LAO/STO [9]. While the origin is not known in detail, and the exact form is not known ab-initio (although there are some interesting hypotheses, such as the theory of ferroelastic domain walls mediating pairing [66]), there are numerous studies of the resulting behaviour, including tuneable interactions (even between attractive and repulsive phases) [15], and multi-electron bound states [67].

In order to treat these interactions, the same approach is taken as in [22], and the mean-field Bogoliubov-Degennes Hamiltonian in the presence of a magnetic field is calculated, which reads

$$\mathcal{H} = \sum_k \vec{c}_k^{\dagger} \begin{pmatrix} \xi_{\uparrow k} & 0 & 0 & \Delta \\ 0 & -\xi_{\uparrow -k} & -\Delta & 0 \\ 0 & -\Delta & \xi_{\downarrow k} & 0 \\ \Delta & 0 & 0 & -\xi_{\downarrow -k} \end{pmatrix} \vec{c}_k, \tag{3.6}$$

where $\xi_{\sigma,k} = E_0(k, n_y, n_z, \sigma) + \Sigma_\sigma$, for

$$\Sigma_\sigma = \frac{U}{2\pi} \int \mathrm{d}k \langle c^\dagger_{k\bar{\sigma}} c_{k\bar{\sigma}} \rangle$$

and

$$\Delta = \frac{U}{2\pi} \int \mathrm{d}k \langle c_{-k\downarrow} c_{k\uparrow} \rangle,$$

with interaction strength U. In this case, there is no process to mediate the spin-flip operation corresponding to the Fock terms, so these have been neglected.

In order to calculate these mean-fields, it is necessary to perform the Bogoliubov transformation $\vec{\gamma}_k = U^\dagger_k \vec{c}_k$. This is difficult to solve analytically, but some progress can still be made by noting the eigenvalue ordering structure $(E_{\downarrow,k}, E_{\uparrow k}, -E_{\uparrow -k}, -E_{\downarrow -k})$, so the eigenvectors are $\vec{\gamma}_k = (\gamma_{\downarrow k}, \gamma_{\uparrow k}, \gamma_{-\uparrow k}, \gamma_{-\downarrow k})$, and so in principle the Bogoliubov transformation can be constructed like this.

Generally, however, these are determined numerically. Using these methods, the behaviour of electrons in the straight waveguide can be determined. However, when calculating the conductance in the paired phase, the gap in the conductance spectrum leads to a case where we have no crossings of the Fermi energy, which would suggest no conductance. The reason for this is that the eigenenergies form the excitation spectrum of quasiparticles. That is, these are the energies of excited quasi-particle states on top of the zero energy ground state. In the gapped region, there are no possible transport channels for the quasi-particles, and it is known that the ground state is made up of pairs [65]. As a result, it is not possible to use the standard Landauer formula to calculate conductance in the presence of pairing interaction.

Another formalism can shed light on this quandary. Due to the Maslov-Stone theorem [24], it can be deduced that the conductance in this paired phase is equal to $2e^2/h$. This is because the conductance of interacting systems is determined by their dissipation into the leads. Since the leads are generally non-interacting, pairing is unsupported in the leads, and so electrons moving into the leads return to being unpaired giving a conductance of e^2/h per electron.

The proof of this theorem uses Luttinger-Liquid theory, which is beyond the scope of this work. However, using these concepts, they calculate the current, and then the conductance from this, showing that the conductance only depends on the Luttinger parameter K (where $K < 1$ for attractive and $K > 1$ for repulsive interactions) in the leads. Since the leads are non-interacting, this is 1, and so e^2/h per spin is obtained for the conductance of an electron pair.

Using the interacting method, the conductance with non-interacting leads can be determined purely from information contained by the phase diagrams. In this thesis, these are defined as plots which show the state of transport electrons as a function of magnetic field B and chemical potential μ_{SG}. Thus, when purely studying the interacting features, we will generally study phase diagrams and describe how they lead to the conductance features as observed in experiment.

For the single particle parameters in the following plots, the same parameters are used as in [22], with $m_x = m_y = 1.9m_e$, $m_z = 6.5m_e$, $l_y = 26\text{nm}$, $l_z = 8.1\text{nm}$, and $g = 0.6$ which were either measured or calculated to be the best experimental match for a single-electron model. For the interacting case, we choose interaction strengths which are low enough to be well described by a mean-field model, but large enough to easily see the features that are induced.

The phase diagram is constructed as follows, with respect to the thermal cutoff ϵ: any region with $\Delta > \epsilon$ is a paired phase - the ground state of the wavefunction is composed entirely of pairs. A non-zero Δ does not necessarily imply superconductivity in one dimension, unlike in higher dimensions. Outside of this region, the populations of the single particle bands can be seen from the Hartree terms: if

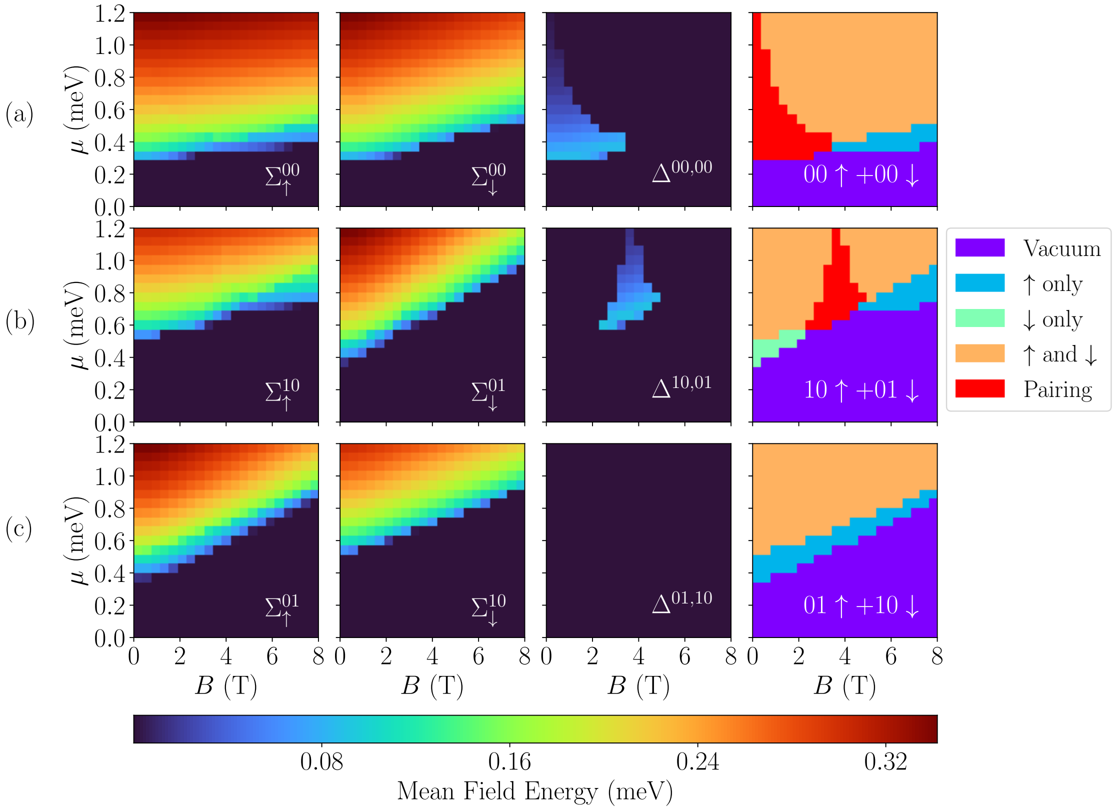

Figure 3.8: Mean fields and phase diagrams for the interaction with strength $U = -4.5$ meV·nm between a) $|0,0,\uparrow\rangle$ and $|0,0,\downarrow\rangle$, b) $|1,0,\uparrow\rangle$ and $|0,1,\downarrow\rangle$, and c) $|0,1,\uparrow\rangle$ and $|1,0,\downarrow\rangle$. Parameters used are $m_x = m_y = 1.9m_e$, $m_z = 6.5m_e$, $l_y = 26$ nm, $l_z = 8.1$ nm, and $g = 0.6$. The first three columns describe the mean-fields $\Sigma_\uparrow$, $\Sigma_\downarrow$, and Δ for the relevant bands labelled by the rows. The final column illustrates the phase diagrams, labelled by the colour scheme on the far right of the grid, constructed from the non-zero areas of the mean-fields in the first three columns.

$\Sigma_\sigma > \epsilon$, then the band corresponding to $\bar{\sigma}$ is available for transport. This latter fact only holds if the bands are continuous (i.e. no band gaps), which they are in the straight waveguide.

In Fig. 3.8, we study these for the interaction between three different types of bands. Firstly, for the interaction between $|0,0,\uparrow\rangle$ and $|0,0,\downarrow\rangle$, the pairing appears at around $B = 0$ T. This is where the two bands, in the single particle case, are closest in energy. As B is increased to around 2 T, the pairing eventually breaks, leading to single particle phases.

In the non-interacting case, the bands $|1,0,\uparrow\rangle$ and $|0,1,\downarrow\rangle$ cross each other at a finite magnetic field. This can be seen in the interacting case where a large paired phase occurs at a finite value of magnetic field. This type of pairing is known as re-entrant pairing as it occurs at magnetic fields $B > 0$ T.

In contrast, $|0,1,\uparrow\rangle$ and $|1,0,\downarrow\rangle$ do not cross in the single particle case, at least in the range of $B \in [0,8]$ T. This is reflected in the phase diagram, as there are no regions in this parameter space where pairing occurs.

3.4 Conclusion

In this section, we have seen that relatively straight-forward models can well describe the conductance features displayed in the straight waveguide, both in single particle and interacting regimes. In the following chapters, this analysis will form the basis of the extension of these techniques to modulated waveguides as in Ch. 4 we include spin-orbit coupling into these models, and in Ch. 5 the modulation potentials will also be included in the interacting calculations.

Chapter 4

Modulated Electron Waveguides

In this chapter of the thesis, we discuss the work undertaken for the papers *One dimensional Kronig-Penney nanowires at the $LaAlO_3/SrTiO_3$ interface* [47] and *Spin-orbit assisted pairing in modulated electron waveguides* [50]. This is split into two sections: the Kronig-Penney waveguide, and the laterally-modulated waveguide. The Hartree-Fock-Bogoliubov model is extended to include spin-orbit couplings which result from these two separate modulations. Through this, it is found that a vertical (coming from a Kronig-Penney modulation) σ_y spin-orbit coupling leads to an increase in the pairing of the lowest two energy bands. The lateral spin-orbit coupling (coming from the sinusoidal modulation of the position of the waveguide centre) along σ_z instead results in triplet pairing.

4.1 Kronig-Penney Waveguides

This section on the Kronig-Penney modulation in electron waveguides begins with a presentation of the experimental method used to introduce a Kronig-Penney potential into the LAO/STO waveguides. We add spin-orbit coupling to the Kronig-

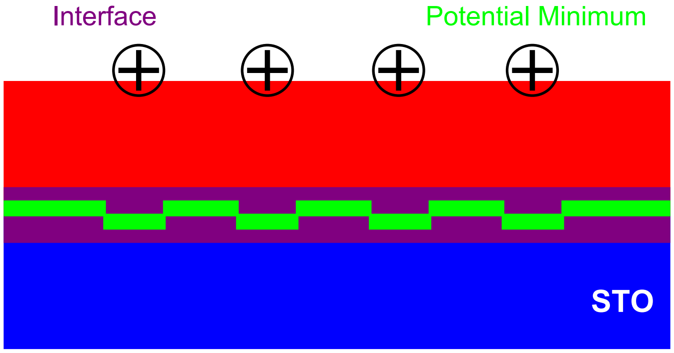

Figure 4.1: Graphic depicting the effect of positive charges on the potential minimum in the interfacial region.

Penney model and derive from it a band structure using a scattering method. Following this, an extension to the mean-field model is presented, neglecting the form of the potential to focus solely on the interplay between interactions and the spin-orbit coupling. Finally, we will see the enhancement of pairing as a result of the spin-orbit coupling, and compare this with experimentally-obtained conductances in $LaAlO_3/SrTiO_3$ nanowires [47].

4.1.1 Kronig-Penney Model In LAO/STO

Before continuing to describe the physics in these nanowires, a description of the experimental setup is provided. The basic devices are grown and written as described in Ch. 1.4. Following this, the waveguide is rewritten with an AC voltage V_{AFM} applied to the AFM tip [47]. The effect of this is to protonate ($V_{AFM} > 0$) and deprotonate ($V_{AFM} < 0$) the surface of the LAO, with the protonated regions being highly conductive and the deprotonated regions acting as barriers (see Fig. 4.1).

In the waveguide model, the exact barrier height introduced by the protonation and deprotonation of the LAO surface is unknown. The magnitude of the gap measured in experiment suggests that this is on the order of $V = 0.01 - 0.1$meV [47], and so values are selected in the full quasi-1D regime to be on this order of magnitude. The wavelength of the modulation is exceptionally well controlled in experiment, with $\lambda = 10$nm the most common [47, 48]. As such, we will restrict analyses to wavelengths of this order.

4.1.2 Vertical-Modulation-Induced Spin-Orbit Coupling

While the potential engineered along the nanowire by this modulation is proportional to x, physically there is also an effect along z, the direction perpendicular to the interface. Consider taking a slice at a constant value of x in Fig. 4.2. The electrostatic potential in this slice varies as a function of x depending on how far away from the (de)protonated LAO surface the nanowire centre is, and thus there is an induced electric field along z. While the exact first-principles physics to calculate the resulting spin-orbit coupling from this is beyond the scope of this thesis, the argument for why we would expect a spin-orbit coupling is similar to that presented in Sec. 2.3. The potential gradient results in an electric field, which interacts with the moving electronic spins through a magnetic field in the electron's frame of reference. This results in an effective spin-orbit coupling introduced by this, which is written as

$$H_{vSOC} = \frac{\alpha_v}{\hbar} p_x \sigma_y, \tag{4.1}$$

where α_v is the unknown spin-orbit coupling strength engineered by the vertical modulation. The form of this is the same form as the Rashba spin-orbit coupling discussed in Sec. 2.3, and so the physics displayed should be similar. However, it must be emphasised that this spin-orbit coupling considered here arises from the

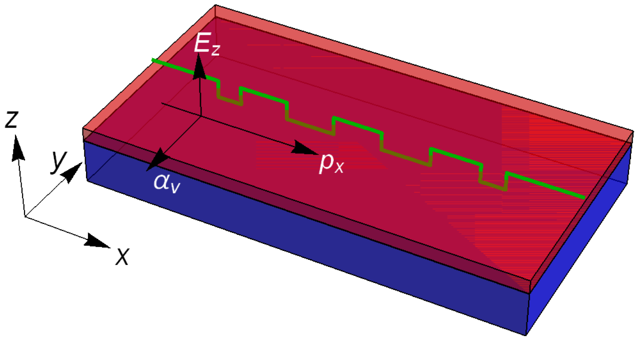

Figure 4.2: Diagrammatic representation of the vertical-modulation-induced spin-orbit coupling. The electrical potential gradient along z as a result of the modulation couples to the momentum of the spins along x, resulting in a spin-orbit coupling along y.

periodic potential and not from the native spin-orbit coupling in the interface. In fact, when confining electrons such that they effectively move along one dimension as in this thesis, the native spin-orbit coupling of the interface is dramatically reduced [50]. This means that being able to re-engineer this in these systems is an extremely interesting prospect for realising many of the one-dimensional applications of spin-orbit coupling such as the Datta-Das spin transistor [57] and Majorana fermions [58].

4.1.3 Kronig-Penney Model With Spin-Orbit Coupling

First, we will calculate the band structure of the Kronig-Penney model with spin-orbit coupling without magnetic field to illustrate the procedure for a single spin-dependent term for which everything remains completely one-dimensional. Following this, the changes resulting from the full quasi-1D case of interest, including the full effects of the magnetic field, shall be summarised.

We begin with the wavefunction eigenvalue equations in each region, where addition of the spin orbit coupling turns these into matrix equations in the spin degree of freedom

$$\left\{\left[\frac{p_x^2}{2m_x} + V[x]\right]\mathbb{I} + \frac{\alpha}{\hbar}p_x\sigma_y\right\}\psi(x) = E\psi(x), \tag{4.2}$$

where $\psi(x)$ is now a vector. Since the Hamiltonian is now expressed as a 2×2 matrix, there are two eigenvalues and eigenvectors. While these can still be split into left-moving and right-moving terms, it is useful to introduce an alternate formalism for obtaining the solutions, as in more complicated cases the k values are not nicely separated into pairs as $\pm k$. This formalism is found in Ref. [68] among others. To do this, we first write Eq. (4.2) in terms of k_J (where J denotes the region, either I or II) by making a plane wave ansatz $\psi_J = \sum_{\beta,\sigma} d_J^{\beta\sigma} e^{ik_J x} |\sigma\rangle$, where $|\sigma\rangle$ is the spin eigenstate and $d_J^{\beta\sigma}$ are the coefficients of the eigenvectors, giving

$$\left[\frac{\hbar^2 k_J^{\beta\,2}}{2m_x} + V_J - E\right] d_J^{\beta\sigma} - i\sigma\alpha k_J^{\beta} d_J^{\beta\bar{\sigma}} = 0, \tag{4.3}$$

where $\bar{\sigma}$ is the opposite spin (i.e. $\bar{\uparrow} = \downarrow$ and $\bar{\downarrow} = \uparrow$). Essentially, this is a rewriting of the usual plane wave in each region but taking into account the spin-mixing which occurs due to the spin-orbit coupling by weighting according to eigenvectors d_J^{β}.

To solve this, we introduce auxiliary coefficients $f_J^{\beta\sigma} = k_J^{\beta} d_J^{\beta\sigma}$ and write Eq. (4.3) as an eigenvalue equation in k_J^{β}:

$$\begin{pmatrix} 0 & \mathbb{I} \\ S^{\beta} & T^{\beta} \end{pmatrix} \begin{pmatrix} d_J^{\beta} \\ f_J^{\beta} \end{pmatrix} = k_J^{\beta} \begin{pmatrix} d_J^{\beta} \\ f_J^{\beta} \end{pmatrix}, \tag{4.4}$$

where

$$S_J = \frac{2m_x}{\hbar^2}(E - V_J)\mathbb{I}, \tag{4.5}$$

and

$$T_J = -\frac{2m_x}{\hbar^2}\alpha\sigma_y. \tag{4.6}$$

From Eq. 4.4, the eigenvalues (k_J^β) and eigenvectors ($d_J^{\beta\sigma}$) can thus be fully determined for a given energy in each region. These are then split into two groups: L for left-moving (negative) and diverging (negative imaginary part) values of k_J^β and R for right-moving (positive) and decaying (positive imaginary part) values of k_J^β. Now terms are relabeled such that β counts only within these groups, and we write k_{JM}^β and $d_{JM}^{\beta\sigma}$, where $M \in \{L, R\}$ labels left- and right- moving groups. However, now right-moving and left-moving are not determined from the sign of k but from the corresponding velocity. This complicates both this procedure and the boundary conditions, which must also be calculated based on the velocity.

The velocity operator can be obtained from the Heisenberg equation as $\hat{v}_x = \frac{i}{\hbar}[H, x]$. This is the same in both regions as the potential in each region commutes with x, and reads

$$\hat{v}_x = \frac{p_x}{m}\mathbb{I} + \frac{\alpha}{\hbar}\sigma_y. \tag{4.7}$$

The wavefunction can be separated into left and right moving terms and is rewritten as

$$\psi_J(x) = \sum_{\beta,\sigma,M} a_{J,M}^\beta d_J^{\beta\sigma} e^{ik_J^\beta x} \left|\sigma\right\rangle, \tag{4.8}$$

where $a_{J,M}^\beta$ denotes the coefficients of the M-moving part of the wavefunction.

This information is then used in writing down the scattering equations. If there is no spin-orbit coupling, the scattering model describes two uncoupled equations, one for each spin. When the spin-orbit coupling is turned on, it essentially couples these two equations, and the strength of the coupling is determines the eigenvectors. There are now eight unknowns and eight equations, as all of the couplings can be determined using the above method. As such, the scattering model now has the spin dependent continuity condition $\psi_I^\sigma(0) = \psi_{II}^\sigma(0)$, and the velocity operator forming the second boundary condition $v_x\psi_I^\sigma(0) = v_x\psi_{II}^\sigma(0)$ giving the two boundary conditions as

$$\sum_\beta a_{LI}^\beta d_{LI}^{\beta\sigma} \left|\sigma\right\rangle + a_{RI}^\beta d_{RI}^{\beta\sigma} \left|\sigma\right\rangle = \sum_\beta a_{LII}^\beta d_{LII}^{\beta\sigma} \left|\sigma\right\rangle + a_{RII}^\beta d_{RII}^{\beta\sigma} \left|\sigma\right\rangle , \tag{4.9}$$

and

$$\begin{aligned}&\sum_\beta a_{LI}^\beta d_{LI}^{\beta\sigma} \left(\frac{\hbar k_{LI}^\beta}{m} \left|\sigma\right\rangle + i\sigma\frac{\alpha}{\hbar} \left|\bar{\sigma}\right\rangle\right) + a_{RI}^\beta d_{RI}^{\beta\sigma} \left(\frac{\hbar k_{RI}^\beta}{m} \left|\sigma\right\rangle + i\sigma\frac{\alpha}{\hbar} \left|\bar{\sigma}\right\rangle\right) \\ =&\sum_\beta a_{LII}^\beta d_{LII}^{\beta\sigma} \left(\frac{\hbar k_{LII}^\beta}{m} \left|\sigma\right\rangle + i\sigma\frac{\alpha}{\hbar} \left|\bar{\sigma}\right\rangle\right) + a_{RII}^\beta d_{RII}^{\beta\sigma} \left(\frac{\hbar k_{RII}^\beta}{m} \left|\sigma\right\rangle + i\sigma\frac{\alpha}{\hbar} \left|\bar{\sigma}\right\rangle\right) ,\end{aligned} \tag{4.10}$$

where $\bar{\sigma}$ denotes the opposite spin (i.e. $\bar{\uparrow} = \downarrow$ and $\bar{\downarrow} = \uparrow$). As without spin orbit coupling, Bloch's theorem is used to generate two more conditions:

$$\begin{aligned}&\sum_\beta a_{IL}^\beta d_{IL}^{\beta\sigma} \left|\sigma\right\rangle e^{-ik_{IL}d} + a_{IR}^\beta d_{IR}^{\beta\sigma} \left|\sigma\right\rangle e^{-ik_{IR}d} \\ =&e^{ik\lambda} \sum_\beta a_{IIL}^\beta d_{IIL}^{\beta\sigma} \left|\sigma\right\rangle e^{ik_{IIL}(\lambda-d)} + a_{IR}^\beta d_{IR}^{\beta\sigma} \left|\sigma\right\rangle e^{ik_{IIR}(\lambda-d)},\end{aligned} \tag{4.11}$$

and

$$
\begin{aligned}
&\sum_{\beta} a^{\beta}_{LI} d^{\beta\sigma}_{LI} \left(\frac{\hbar k^{\beta}_{LI}}{m} \left|\sigma\right\rangle + i\sigma \frac{\alpha}{\hbar} \left|\bar{\sigma}\right\rangle \right) e^{-ik_{IL}d} + a^{\beta}_{RI} d^{\beta\sigma}_{RI} \left(\frac{\hbar k^{\beta}_{RI}}{m} \left|\sigma\right\rangle + i\sigma \frac{\alpha}{\hbar} \left|\bar{\sigma}\right\rangle \right) e^{-ik_{IR}d} \\
=&e^{ik\lambda} \sum_{\beta} a^{\beta}_{LII} d^{\beta}_{LII} \left(\frac{\hbar k^{\beta}_{LII}}{m} \left|\sigma\right\rangle + i\sigma \frac{\alpha}{\hbar} \left|\bar{\sigma}\right\rangle \right) e^{ik_{IIL}(\lambda-d)} \\
+&e^{ik\lambda} \sum_{\beta} a^{\beta}_{RII} d^{\beta}_{RII} \left(\frac{\hbar k^{\beta}_{RII}}{m} \left|\sigma\right\rangle + i\sigma \frac{\alpha}{\hbar} \left|\bar{\sigma}\right\rangle \right) e^{ik_{IIR}(\lambda-d)},
\end{aligned}
\tag{4.12}
$$

which also hold. This can then be written as a matrix equation in the same way as before, using a basis of the scattering coefficients a^{β}_{JM} and solved for the Bloch quasimomenta k:

$$
\begin{pmatrix}
d^{\beta\sigma}_{RI} & d^{\beta\sigma}_{LI} & -d^{\beta\sigma}_{RII} & -d^{\beta\sigma}_{LII} \\
f^{\beta\sigma}_{RI} & f^{\beta\sigma}_{LI} & -f^{\beta\sigma}_{RII} & -f^{\beta\sigma}_{LII} \\
p^{\beta\sigma}_{RI} & p^{\beta\sigma}_{LI} & -q^{\beta\sigma}_{RII} e^{ik\lambda} & -q^{\beta\sigma}_{LII} e^{ik\lambda} \\
r^{\beta\sigma}_{RI} & r^{\beta\sigma}_{LI} & -s^{\beta\sigma}_{RII} e^{ik\lambda} & -s^{\beta\sigma}_{LII} e^{ik\lambda}
\end{pmatrix}
\begin{pmatrix}
a^{\beta}_{RI} \\ a^{\beta}_{LI} \\ a^{\beta}_{RII} \\ a^{\beta}_{LII}
\end{pmatrix}
= 0,
\tag{4.13}
$$

where $f^{\beta\sigma}_{MJ} = d^{\beta\sigma}_{MJ} \frac{\hbar k^{\beta}_{MJ}}{m} + i\sigma \frac{\alpha}{\hbar} d^{\beta\bar{\sigma}}_{MJ}$, $p^{\beta\sigma}_{MJ} = d^{\beta\sigma}_{MJ} e^{-ik^{\beta}_{MJ}d}$, $q^{\beta\sigma}_{MJ} = d^{\beta\sigma}_{MJ} e^{ik^{\beta}_{MJ}(\lambda-d)}$, $r^{\beta\sigma}_{MJ} = \left(d^{\beta\sigma}_{MJ} \frac{\hbar k^{\beta}_{MJ}}{m} + i\sigma \frac{\alpha}{\hbar} d^{\beta\bar{\sigma}}_{MJ} \right) e^{-ik^{\beta}_{MJ}d}$ and $s^{\beta\sigma}_{MJ} = \left(d^{\beta\sigma}_{MJ} \frac{\hbar k^{\beta}_{MJ}}{m} + i\sigma \frac{\alpha}{\hbar} d^{\beta\bar{\sigma}}_{MJ} \right) e^{ik^{\beta}_{MJ}(\lambda-d)}$. By requiring a determinant of zero for the system, an equation in k can be obtained, and the band structure determined.

In Fig. 4.3, the effect of adding the Kronig-Penney potential to a spin-orbit coupled system is displayed. Firstly, the features far from the band gap are extremely similar, displaying the familiar double minimum expected from a system with spin-orbit coupling, albeit shifted in energy by the potential. However, rather than appearing directly at the Brillouin zone edge, the band gap is opened inside

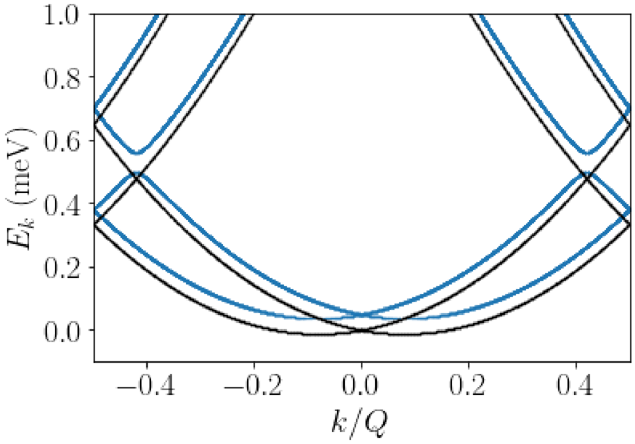

Figure 4.3: Band Structure of the Kronig-Penney model with spin-orbit coupling $\alpha = 1.0$meVnm (blue) compared to the band structure without Kronig-Penney modulation (black) folded back into a $\lambda = 20$nm Brillouin zone, for $d = \lambda/2$ and $V_0 = 0.1$meV.

the Brillouin zone. This occurs due to the splitting of the dispersion relation into two centred around $\pm k_{min}$. Then, as the band structure is folded back into the first Brillouin zone, the band gaps occur inside rather than at the edge. This is illustrated more cleanly in Fig. 4.4.

When moving to a full quasi 1D picture with magnetic field included, the matrices in each region become

$$S_J = \frac{2m_x\Omega^2}{\hbar^2\omega_y^2}\big[(E - V_J - V_{y,z})\,\mathbb{I} + M\sigma_z\big], \tag{4.14}$$

and T_J unchanged, where $V_{y,z} = \hbar\Omega\,(n_y + 1/2) + \hbar\omega_z(2n_z + 3/2)$ and $M = g\mu_B B/2$. Terms $\mathcal{O}(\alpha^2)$ have been neglected for now as α is assumed to be small due to the modulation amplitude being less than the trapping energy ($\alpha \leq 0.1$meV vs $\alpha \geq 0.6$meV). The velocity operator becomes

$$\hat{v}_x = \frac{\omega_y^2}{\Omega^2}\left[\frac{p_x}{m}\mathbb{I} + \frac{\alpha}{\hbar}\sigma_y\right], \tag{4.15}$$

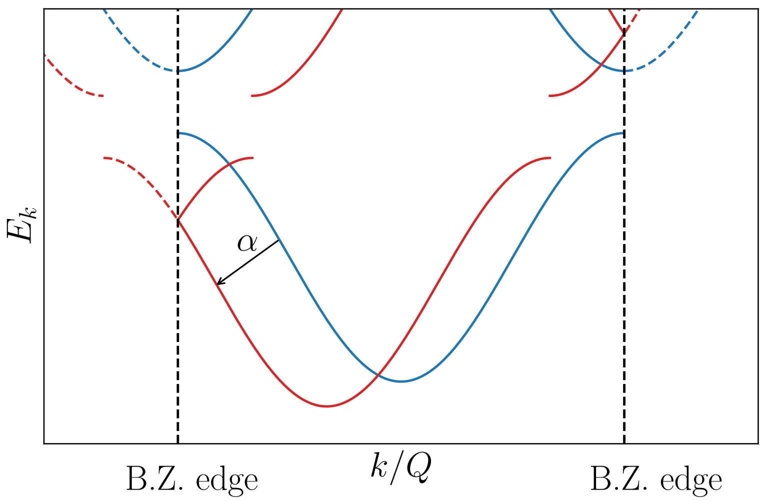

Figure 4.4: Illustration of the effect of spin-orbit coupling on the Kronig-Penney band structure. At $\alpha = 0$ (blue), the band gap lies at the edge of the Brillouin zone. When increasing α (red), the entire band structure is translated left for one energy state (red) and right for the other (not shown for clarity). This causes the lowest band to fold back in to the Brillouin zone and pushes the band gap away from the B.Z. edge.

which means, due to the factor ω_y^2/Ω^2 being a prefactor on both sides of the boundary conditions in Eq. (4.22) and Eq. (4.24), leaving them unchanged. The only difference comes from the modified form of S_J when calculating the momenta in each region. The resulting band structures are displayed in Fig. 4.5, where we see the inclusion of the magnetic field shifts the Kronig-Penney gap in energy, and also introduces a spin-orbit gap at $k = 0$.

When calculating the transconductance spectrum for this model, we obtain Fig. 4.6. With $V = 0$meV, we obtain the standard quantised conductance peaks as displayed in Ch. 3. However, when including $V = 0.075$meV, this introduces a fracturing of these transconductance peaks. This introduces regions of negative transconductance (decreasing conductance with increasing chemical potential), which are displayed in white. This can be directly compared to experiment in Fig. 4.7, where a region of negative transconductance is observed in the blue box, along with a fracturing of the

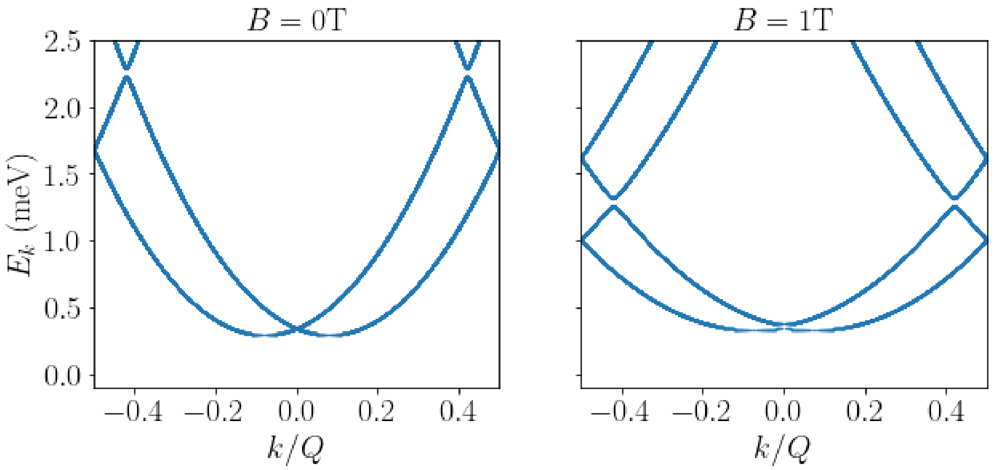

Figure 4.5: Band structures for $n_y = 0$, $n_z = 0$ in the quasi 1D waveguide model including spin-orbit coupling $\alpha_v = 1.0$meVnm and Kronig-Penney modulation $V_0 = 0.1$meV for a) $B = 0$T and b) $B = 1$T. Parameters read $m_x = m_y = 1.9m_e$, $m_z = 6.5m_e$, $l_y = 26$nm, l_z=8.1nm, and $g = 0.6$, with $\lambda = 20$nm and $d = \lambda/2$.

lowest transconductance peak.

4.1.4 Enhanced Pairing In Kronig-Penney Waveguides

To study the interplay between the engineered spin-orbit coupling and electron-electron interactions, the effect of the potential on the band structure is temporarily neglected (this will be reintroduced in the next chapter). Thus, the only effect considered in this section resulting from the potential is the vertical-modulation-induced spin-orbit coupling.

Eq. (4.1) describes this effect at a single particle level. To include it in the mean-field model developed in the previous chapter for studying interactions in electron waveguides, it must be written in second quantization. Using the same definition of

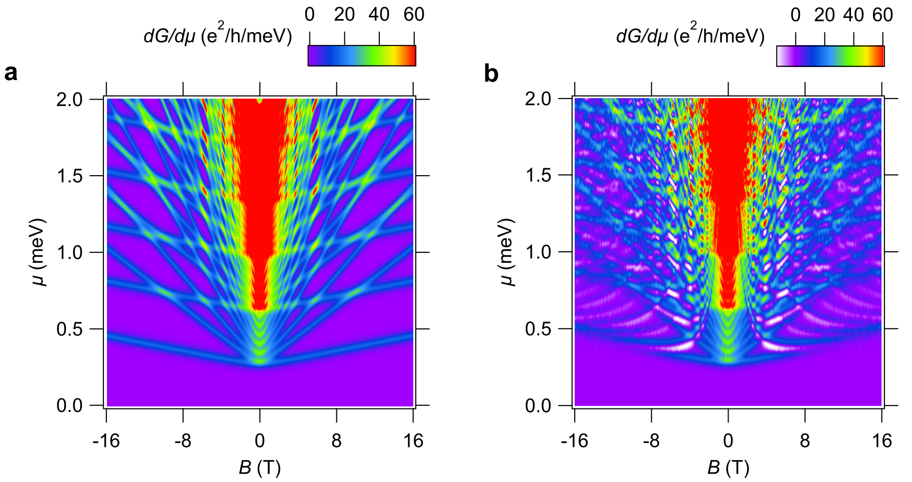

Figure 4.6: Theoretical transconductance calculations of the (a) straight waveguide, and (b) Kronig-Penney Waveguide with $V = 0.075$meV, for $m_x = m_y = 1.9m_e$, $m_z = 6.5m_e$, $g = 0.62$, $l_y = 26$nm, and $l_z = 8.1$nm. The regions in white denote negative transconductance. Figure adapted from *One-dimensional Kronig-Penney superlattices at the LaAlO$_3$/SrTiO$_3$ interface*, Nature Physics volume 17, pages 782–787 (2021) [47]. Permission obtained from Springer Nature and the authors.

the mode operators as Eq. (2.38) results in the form

$$\mathcal{H}_{vSOC} = -i\alpha_v \sum_{k\sigma} \sigma k c^\dagger_{k\sigma} c_{k\bar{\sigma}}. \tag{4.16}$$

This has the same form as the Fock terms described in Eq. (2.45), which are

$$\mathcal{H}_F = \sum_k \chi c^\dagger_{k\downarrow} c_{k\uparrow} + \chi^* c^\dagger_{k\uparrow} c_{k\downarrow}. \tag{4.17}$$

Since these Fock processes are now mediated by the spin-orbit term, they can no longer be neglected. We are still most interested in the pairing, which is given by

$$\Delta = \frac{U}{2\pi} \int \mathrm{d}k \langle c_{-k\downarrow} c_{k\uparrow} \rangle. \tag{4.18}$$

In Sec. 3.3, it was specified that this is a real quantity. This is unchanged by the

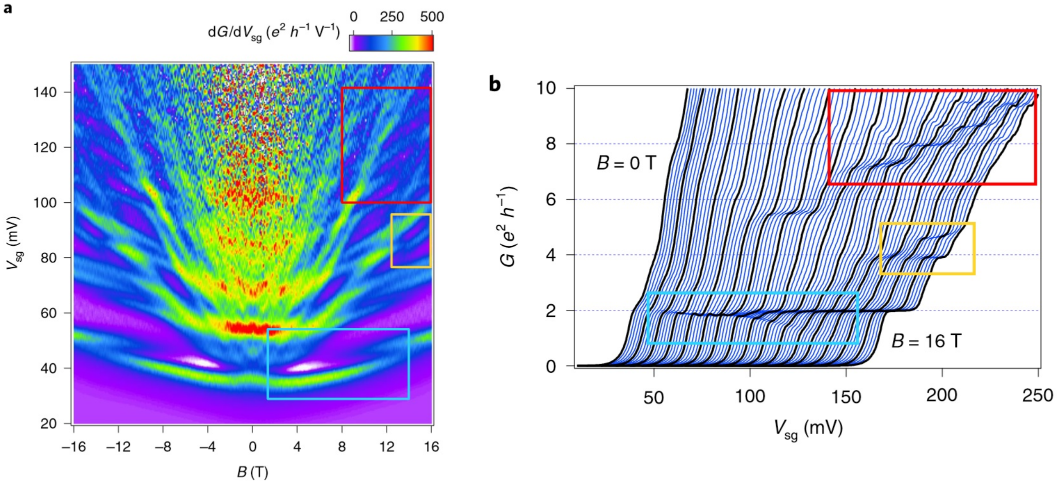

Figure 4.7: Experimental (a) transconductance and (b) conductance plots of the Kronig-Penney waveguide. In the blue boxed region, we observe a strong conductance baseline of $2e^2/h$ which is a signature of electron pairing at such high fields. Additionally, there is a fracturing of this plateau, which we suggest comes from the Kronig-Penney gap in the band structure. Again, the regions in white denote transconductance. The yellow and red boxed regions denote effects which are beyond the scope of this thesis. Figure adapted from *One-dimensional Kronig-Penney superlattices at the* $LaAlO_3/SrTiO_3$ *interface*, Nature Physics volume 17, pages 782–787 (2021) [47]. Permission obtained from Springer Nature and the authors.

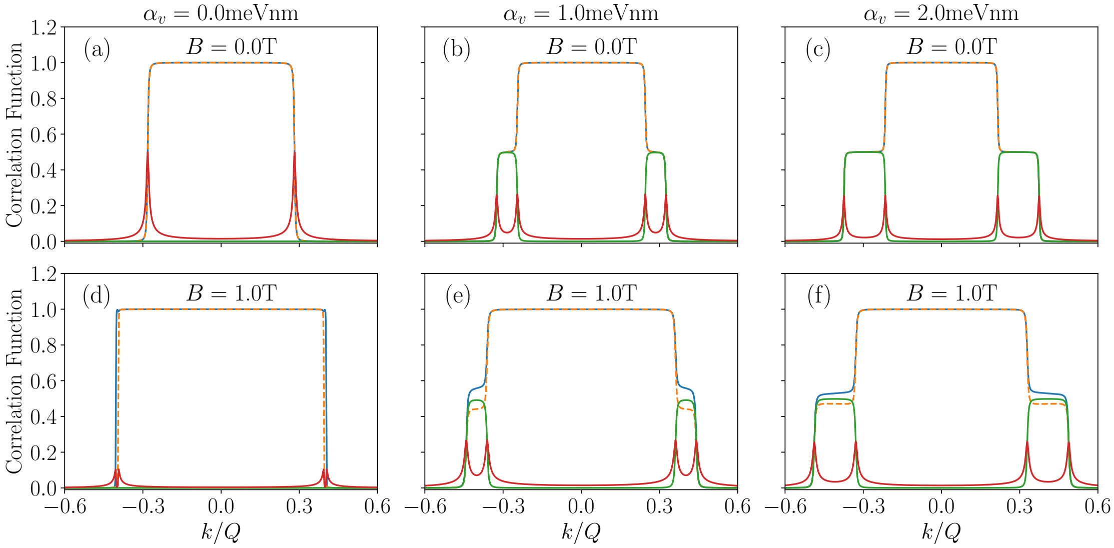

Figure 4.8: Correlation functions for the vertically-modulated waveguide at various different spin-orbit coupling strengths and magnetic fields. The blue and orange lines are the $\langle c^\dagger_{k\uparrow} c_{k\uparrow}\rangle$ and $\langle c^\dagger_{k\downarrow} c_{k\downarrow}\rangle$ respectively (Hartree correlations), the green is the $\left|\mathrm{Im}\left(\langle c^\dagger_{k\downarrow} c_{k\uparrow}\rangle\right)\right|$ (Fock correlation), and the red is the $\langle c_{-k\downarrow} c_{k\uparrow}\rangle$ (pairing correlation). These have been performed with $g = 0.6$, $m_x = m_y = 1.9m_e$, $m_z = 6.5m_e$, $ly = 26$nm, $lz = 8.1$nm, and $U = -4.0$meVnm.

presence of the Fock terms, and thus should still correspond to the appearance of a gap in the excitation spectrum.

To study in more detail how the interactions are affected by the spin-orbit coupling, we analyse the correlation functions $\langle c^\dagger_{k\sigma} c_{k\sigma}\rangle$, $\langle c^\dagger_{k\downarrow} c_{k\uparrow}\rangle$, and $\langle c_{-k\downarrow} c_{k\uparrow}\rangle$ as a function of k. In Fig. 4.8 , these are presented for various values of the spin-orbit coupling strength and two different magnetic fields. First, a general trend is that increasing the spin-orbit coupling strength α splits the peaks in the pairing correlation $\langle c_{-k\downarrow} c_{k\uparrow}\rangle$ (in red). At finite magnetic fields, the height of the peak is also enhanced by this (the height of the peaks in the red curve when going from Fig. 4.8d to Fig. 4.8e), suggesting an enhanced pairing strength occurring as a result of the engineered spin-orbit coupling. Additionally, the inclusion of the spin-orbit coupling leads to two separate plateaux in the Hartree correlations (blue and orange) at approximately half-filling. This is consistent with the spin-mixing effect expected when this kind of spin-orbit coupling is introduced, and occurs alongside the inclusion of the Fock correlations (green). Essentially, the spin-orbit coupling leads to a reduction in the population in the up state to partially populate the down.

Now in order to determine the overall effect of these changes to the correlation functions, we take the integral over k at each point in the (B,μ_{SG}) parameter space, and generate phase diagrams for various values of spin-orbit coupling strength. We generate the mean-fields which describe the interacting effects in the Hamiltonian and allows for the characterisation of the electronic state in each region. Recall from Sec. 3.3 that a finite Δ implies a paired electron ground state, and $\Delta = 0$ but $\Sigma_{\bar{\sigma}} > 0$ implies the single electron state σ is occupied. The result of this procedure is displayed in Fig. 4.9. The main feature that can be seen from these plots is a significant enhancement in the area at which electrons pair when increasing the spin-orbit coupling. Additionally, the Zeeman splitting of the two unpaired bands appears to reduce at higher spin-orbit coupling strengths, as the area of the single-electron phase is reduced (light blue). This does not appear at low fields as the magnetic field is not strong enough to break pairs in the ground state. Both of these observations suggest that the electron-electron interactions are being enhanced by the spin-orbit coupling. At high chemical potentials, pairs are broken to form single electron states. This is due to the fact that pairing is proportional to density of states, and this peaks at the bottom of the single-electron bands and decays as $1/k$ in one dimension.

These results are consistent with experimental transconductance measurements, which are displayed in Fig. 4.7. As is shown in the transconductance plot in Fig. 4.7a, the transconductance forms a (mostly) stable first peak, which the conductance plots

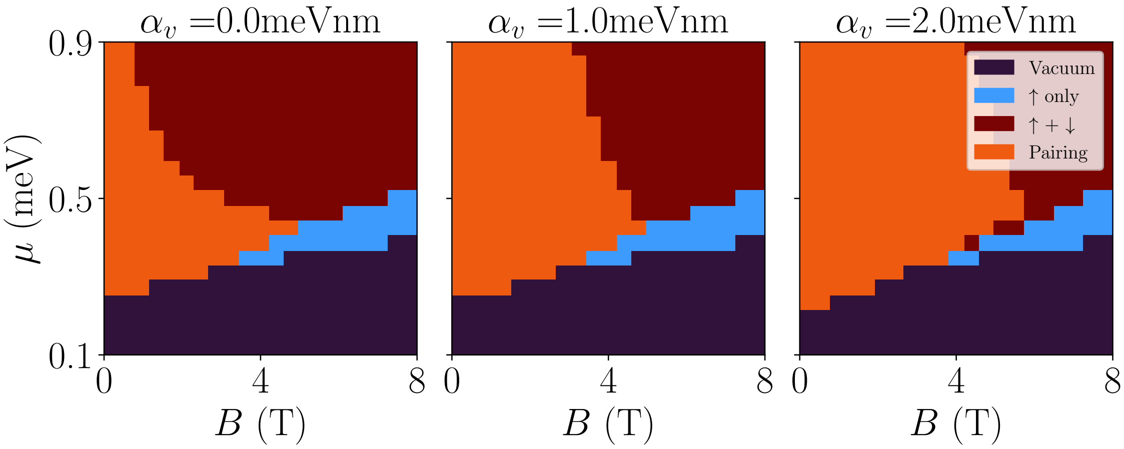

Figure 4.9: Phase diagrams showing the effect of increasing the vertical-modulation-induced spin-orbit coupling strength. Simulations performed with $g = 0.6$, $m_x = m_y = 1.9m_e$, $m_z = 6.5m_e$, $l_y = 26$nm, $l_z = 8.1$nm, and $U = -4.0$meVnm.

in Fig. 4.7b show attains a conductance of $2e^2/h$ up to $B = 16$T. This is significantly enhanced compared to the straight waveguide, where conductances peaks of only e^2/h are observed above $B \sim 2T$ (see Fig. 3.4).

4.2 Laterally-Modulated Waveguides

The second section of this chapter is dedicated to the laterally-modulated waveguide model. We discuss the effects of the sinusoidal modulation of the position of the nanowire in-plane (i.e. along the two-dimensional LAO/STO interface) as a modulation in the centre of the harmonic trap, as visualised in as in Fig. 4.10. Then, focusing on the engineered spin-orbit coupling once more, we see that this gives rise to triplet pairing of electrons in the channel.

4.2.1 Serpentine Modulation

This lateral "serpentine" modulation has the 2D Hamiltonian

$$H = \frac{p_x^2}{2m_x} + \frac{p_y^2}{2m_y} + \frac{m_y}{2}\omega_y^2(y - A_y \sin Qx)^2. \tag{4.19}$$

This is difficult to solve analytically, so the wavefunction is approximated as a harmonic oscillator with a modulated centre of motion. This approximation neglects the coupling between x and y induced by the modulation, and requires A_y be smaller than the width of the nanowire ($A_y = 10\text{nm}$ is common, versus $l_y = 26\text{nm}$).

The main effect of interest appearing from this modulation is an engineered spin-orbit coupling. Following the logic in Sec. 4.2.3, a y-dependent electric field leads to a lateral-modulation-induced spin-orbit coupling given by

$$H_{lSOC} = -\frac{\alpha_l}{\hbar} p_x \sigma_z, \tag{4.20}$$

which resembles the Zeeman shift introduced previously but is proportional to p_x. This is shown in Fig. 4.10 where the effective magnetic field the electron feels from the engineered electric field along y is indeed parallel to the out-of-plane applied external magnetic field.

We study the physics of this lateral-modulation-induced spin-orbit coupling in the same order as the vertical-modulation-induced spin-orbit coupling. First, we will detail the effect of this on the band structure, and then show the interplay between it and the Zeeman field. This is displayed in Fig. 4.11. When introducing the lateral-modulation-induced spin-orbit coupling in the absence of magnetic field, the minimum of the energy band is split into two at $k_0 = \pm\alpha_l m_x/\hbar^2$, which increases linearly with increasing α_l. However, when introducing the magnetic field B, the

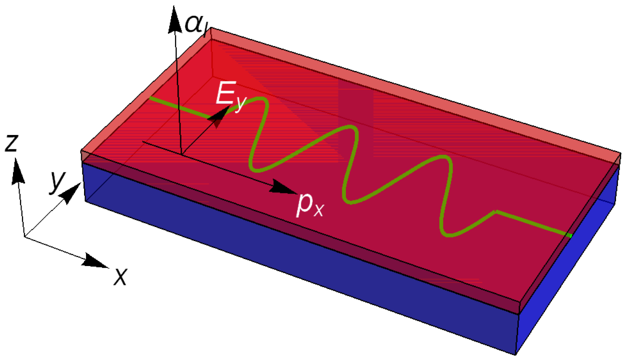

Figure 4.10: Graphical depiction of the engineering of the lateral-modulation-induced spin-orbit coupling. The modulation creates an electrical potential gradient along y, which couples to the motion along x resulting in a spin-orbit coupling along z.

interplay between α_l and B leads to an asymmetry in the energies, which can be seen by inserting k_0 (which is unchanged by the magnetic field) back into the Hamiltonian giving minimal eigenvalues

$$E_k^{min} = -\left(1 - \frac{\omega_c^2}{\Omega^2}\right)\frac{\alpha_l^2 m_x}{2\hbar^2} \pm g\frac{\mu_B}{2}B.$$

This introduced asymmetry in the band structure is important as it breaks a crucial symmetry in the interacting case, allowing for the formation of triplet pairs.

4.2.2 Triplet Pairing In Serpentine Waveguides

In the mean-field theory used so far, triplet pairing does not appear, and only singlet pairing occurs. This is due to the symmetry that $E_p(k) = -E_h(k)$, where p and h refer to the particle and hole sectors respectively. It should be noted that this is not

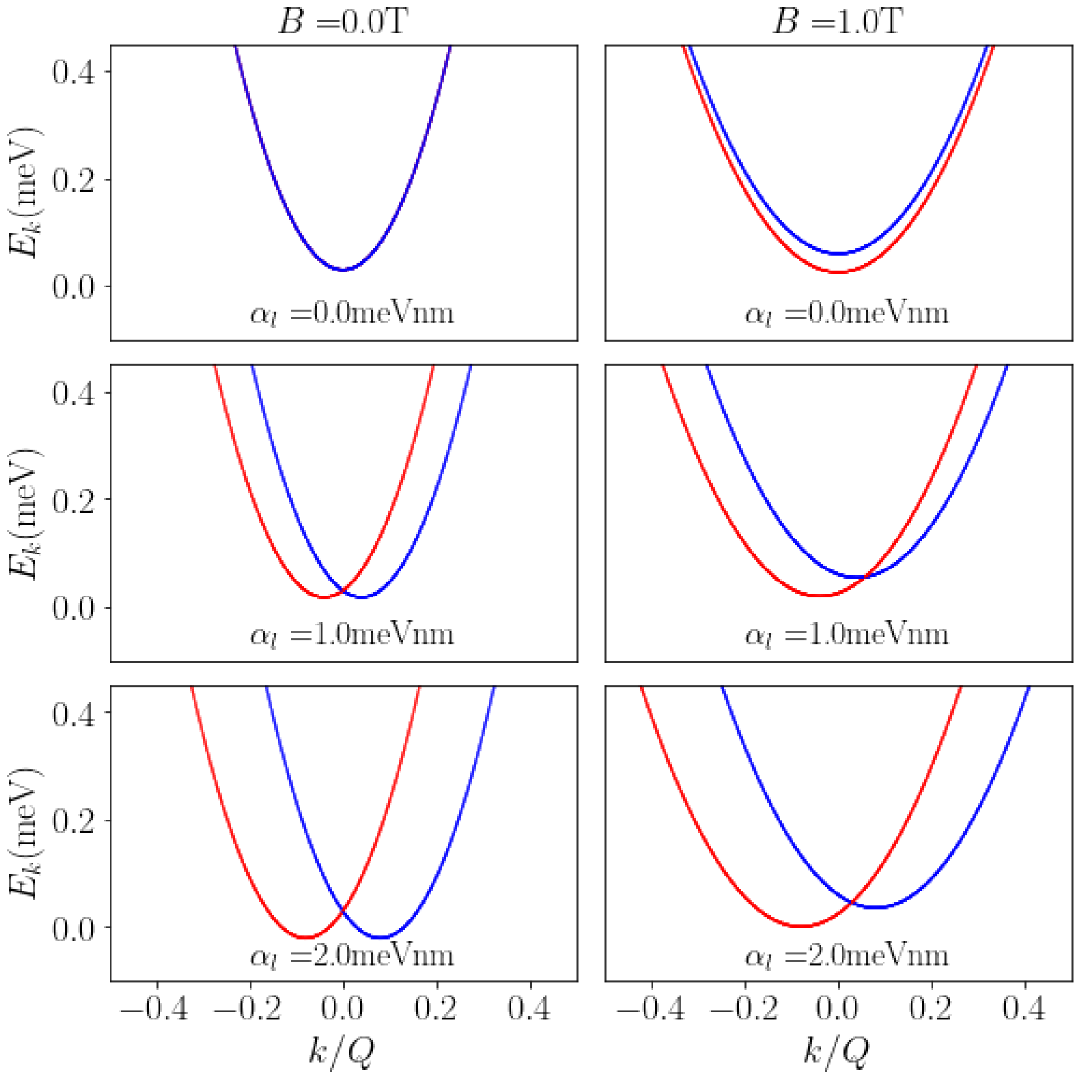

Figure 4.11: Band structures showing the interplay between magnetic field B and lateral-modulation-induced spin-orbit coupling strength α_l. The red lines are spin-up, and the blue lines spin-down. For all of these, $g = 0.6$, $m_x = m_y = 1.9m_e$, $m_z = 6.5m_e$, $l_y = 26$nm, $l_z = 8.1$nm, and $\lambda = 10$nm.

the same as particle-hole symmetry, which is $E_p(k) = -E_h(-k)$. This symmetry holds whenever the band structure is symmetric around $k = 0$.

The influence of this property can be seen by defining the singlet and triplet operators as

$$2\hat{s}_k = c_{-k\downarrow}c_{k\uparrow} - c_{-k\uparrow}c_{k\downarrow}, \tag{4.21}$$

and

$$2\hat{t}_k = c_{-k\downarrow}c_{k\uparrow} + c_{-k\uparrow}c_{k\downarrow}. \tag{4.22}$$

By performing the Bogoliubov transformation as in Sec. 2.4, it can be shown that for a symmetric band structure, $c_{-k\uparrow}c_{k\downarrow} = -c_{-k\downarrow}c_{k\uparrow}$. This means that $\hat{s}_k = c_{-k\downarrow}c_{k\uparrow}$, which is the correlation function which appears in the mean-field energy throughout the thesis. However, if the band structure is asymmetric, $c_{-k\uparrow}c_{k\downarrow} \neq -c_{-k\downarrow}c_{k\uparrow}$. Thus, the lateral-modulation-induced spin-orbit coupling as described in the previous section could stabilise triplet pairing in these systems.

In the interacting formalism as previously introduced, the lateral-modulation-induced spin-orbit coupling reads

$$\mathcal{H}_{lSOC} = \alpha_l \sum_k c^\dagger_{k\downarrow}c_{k\downarrow} - c^\dagger_{k\uparrow}c_{k\uparrow}. \tag{4.23}$$

Upon introducing this to the interacting model, the correlation functions can be studied as in the above section on the vertical modulation. However, in this case the Fock terms are zero since there is no spin-mixing effect, and instead of looking at the pairing correlation function, we include the singlet and triplet correlation functions instead. These are displayed in Fig. 4.12. Firstly, when $\alpha_l = 0.0$meVnm, there are no triplet correlations (in red) and a strong contribution of the singlet correlation

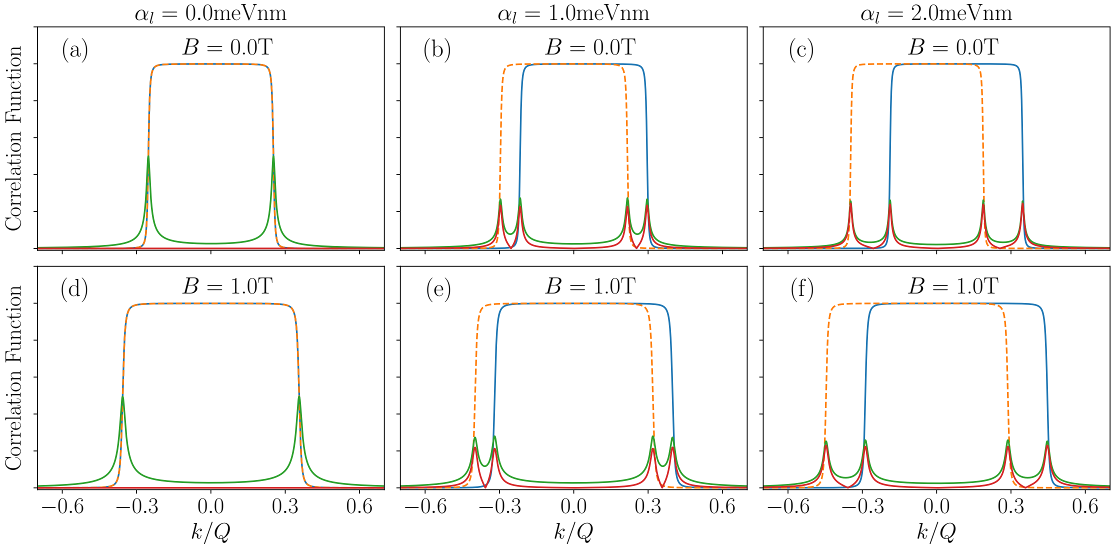

Figure 4.12: Correlation functions for the lateral-modulated waveguide at various different spin-orbit coupling strengths and magnetic fields. The blue and orange lines are the $\langle c^\dagger_{k\uparrow} c_{k\uparrow}\rangle$ and $\langle c^\dagger_{k\downarrow} c_{k\downarrow}\rangle$ respectively (Hartree correlations), the green is the $|\langle s_k\rangle|$ singlet correlation, and the red is the $|\langle t_k\rangle|$ triplet correlation. These have been performed with $g = 0.6$, $m_x = m_y = 1.9m_e$, $m_z = 6.5m_e$, $l_y = 26$nm, $l_z = 8.1$nm, and $U = -4.0$meVnm.

(green), as expected. However, when $\alpha_l > 0$, the pairing correlation is split into two branches corresponding to singlet and triplet pairing correlators, which peak at the momenta where the occupations (which are the Hartree terms in blue and orange) drop significantly. This effect is also stable to the inclusion of the magnetic field. Absolute values are plotted to keep the axes the same, as the triplet correlation is an odd function as shown in Fig. 4.13.

One property of note for the triplet pairing is that there is no specific mean-field pertaining to it. As is shown in Fig. 4.13, the triplet correlation function is odd in k, and thus has an integral of zero. To construct phase diagrams including the triplet

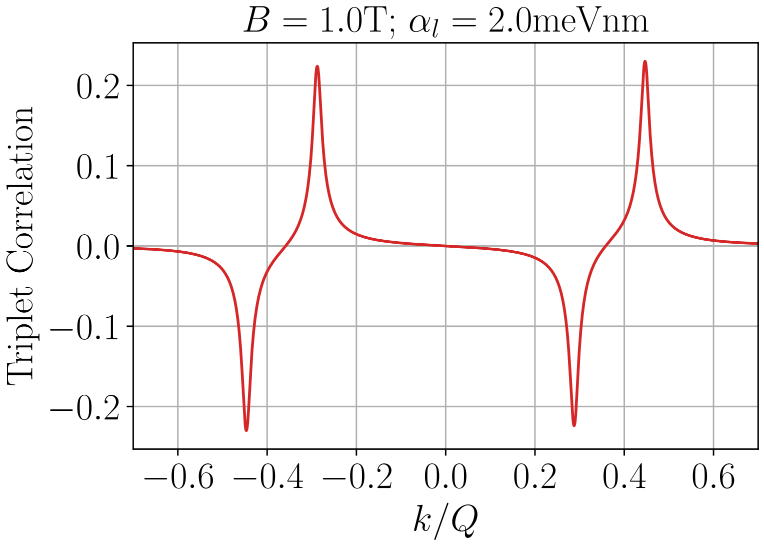

Figure 4.13: Triplet correlation function from Fig. 4.12f plotted in full to show that it is odd. This is important as this means the integral of this correlation function alone is zero, making it necessary to be more careful when defining a triplet energy.

pairing, we define the integrals

$$n_s = \frac{1}{2\pi}\int \mathrm{d}k|\langle\hat{s}_k\rangle| \text{ and } \quad n_t = \frac{1}{2\pi}\int \mathrm{d}k|\langle\hat{t}_k\rangle|. \tag{4.24}$$

which are related to the density of singlet and triplet pairs respectively. Through these, we define the energies

$$\Delta_s = Un_s \text{ and } \quad \Delta_t = Un_t, \tag{4.25}$$

which are now the parameters which will be used to determine the different regions of the phase diagram, in analogy with Fig. 3.8. These have been defined to be consistent with previous calculations in respect to the threshold energy for the numerical calculations.

In Fig. 4.14, the phase diagrams showing the effect of a non-zero lateral spin-orbit

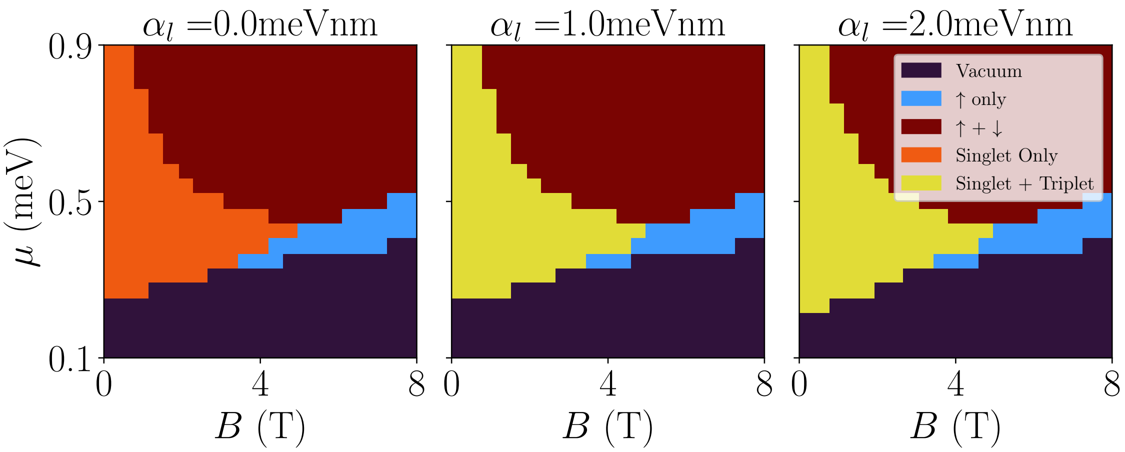

Figure 4.14: Phase diagrams showing the effect of increasing the lateral-modulation-induced spin-orbit coupling strength. Simulations performed with $g = 0.6$, $m_x = m_y = 1.9m_e$, $m_z = 6.5m_e$, $l_y = 26$nm, $l_z = 8.1$nm, and $U = -4.0$meVnm.

coupling are displayed. Fig. 4.14a with zero lateral spin-orbit coupling displays only singlet pairing. However, when the lateral spin-orbit coupling is non-zero, this results in triplet pairing in the same region of parameter space where the singlet pairing is non-zero, giving rise to a combination of the two in the waveguide region. This occurs due to the lateral-modulation-induced spin-orbit coupling producing an asymmetry in the excitation spectrum as a function of k, leading to a non-zero odd part of the wavefunction. Unlike in the case with vertical spin-orbit coupling, the area of the region in parameter space where electron pairing occurs is not significantly affected. The numerical deviations here are likely numerical and may be reduced by increasing the precision of the simulation.

4.3 Conclusion

In this chapter, we have seen that the vertical modulation leads to a significant enhancement in the singlet pairing strength and area when looking solely at the engineered spin-orbit coupling resulting from this. This is in contrast to the lateral modulation, which does not strongly affect the region in the parameter space and the amplitude of Δ_S but instead generates a contribution from the triplet pairing. My hypothesis is that the pairing energy is lowered due to the fact that the triplet energy is zero, and so splitting the total pairing into the two different pieces naturally lowers the energy. These two spin-orbit couplings will be at the forefront of the physics of the helical waveguide in the next chapter.

Chapter 5

Helical Waveguide

One aspect of the applicability of LAO/STO to quantum simulation is the high degree of control over the electrons in the nanowires. In this chapter, I analyse a specific case of this - the helical waveguide. In this system, the minimum of the electronic potential follows a helix along the waveguide.

Chirality is an important property in chemistry. For example, some drugs such as Citalopram are chiral, but only one of its enantiomers is responsible for its medicinal effect [69]. Another is Penicillamine, which is a drug for rheumatoid arthritis in one form, but a potent toxin in another [70]. A more familiar example of a chiral molecule is DNA, where the double-helix structure is right-handed [71].

Electron transport in chiral systems is exciting for many reasons, but one such is the study of quantum effects in DNA. The idea of chiral-induced spin-selectivity (CISS) [72] has long been known to play a role in charge transfer in DNA, but this is extremely difficult to control in the molecules themselves. However, if quantum transport can be simulated in a highly controllable and measurable platform such as LAO/STO nanowires, they would be an attractive prospect for studying CISS via analogue quantum simulation of DNA.

CISS is not only of interest for its role in the function of DNA, but also may underpin new spin-based technologies. For example, one group at National Renewable Energy Laboratory (NREL) created a spin-polarised LED using the effect [73] without the need for magnetic fields. Additionally, CISS can also be used in the separation of the two different enantiomers of drugs in a process known as enantioseparation [74].

When chiral nanowires are made in LAO/STO (with geometry as displayed in Fig. 5.1), compared to the singly-modulated waveguides discussed in the previous chapter, there are both new features and quantitatively more pronounced effects. The experimental transconductance measurements show extremely strong pairing, up to above 18T, which can be seen in Fig. 5.2a,b. This contrasts strongly to the straight (control) waveguide in Fig. 5.2c,d, where the pairing breaks at around $B = 10$T. However, there is no longer the presence of a fracturing of the first transconductance peak (see Fig. 4.7a) - rather, there is a stable plateau of $G = 2e^2/h$. Another main point of interest is the oscillations that take place before the second conductance plateau of $4e^2/h$, which appear to take place on top of a $2e^2/h$ baseline.

It is this effect that the final chapter of my thesis focuses on. We construct a mean-field model which works even in the presence of a periodic potential to study the effect of electron-electron interactions. This provides the numerical data to study in detail the effect of every parameter on the correlation functions obtained from the model. Finally, we develop a phenomenological pair-scattering model, and show that a baseline of $2e^2/h$ with oscillations up to $4e^2/h$ on top of this is consistent with a selective back-scattering of triplet pairs incident on the junction between helical and unmodulated regions.

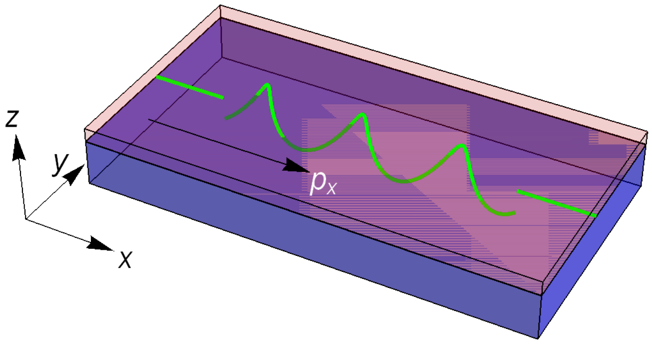

Figure 5.1: Graphical depiction of the geometry of the helical devices of interest to this thesis. The combination of the lateral and vertical modulations results in a helical potential minimum, displayed here by the green line.

5.1 Single Particle Physics

5.1.1 No Spin-Orbit Coupling

We begin with the Hamiltonian for the full straight waveguide

$$H = \left[\frac{(p_x - eBy)^2}{2m_x} + \frac{p_y^2}{2m_y} + \frac{p_z^2}{2m_z} + \frac{m_y}{2}\omega_y^2 y^2 + \frac{m_z}{2}\omega_z^2 z^2 - \mu_{SG}\right]\mathbb{I}_\sigma - \frac{g\mu_B}{2}B\sigma_z. \quad (5.1)$$

The model for the helical waveguide includes both of the modulations discussed in Ch. 4. The vertical modulation, which is modelled by a Kronig-Penney-type potential, reads

$$H_{ver} = A_z \cos Qx\mathbb{I}_\sigma, \quad (5.2)$$

for $Q = 2\pi/\lambda$, where λ is the wavelength of the modulation. Here A_z is the amplitude of the modulation, with units of energy, and $\mathbb{I}_\sigma$ is the identity matrix on the spin degree of freedom. The lateral (serpentine) modulation takes the form of an x

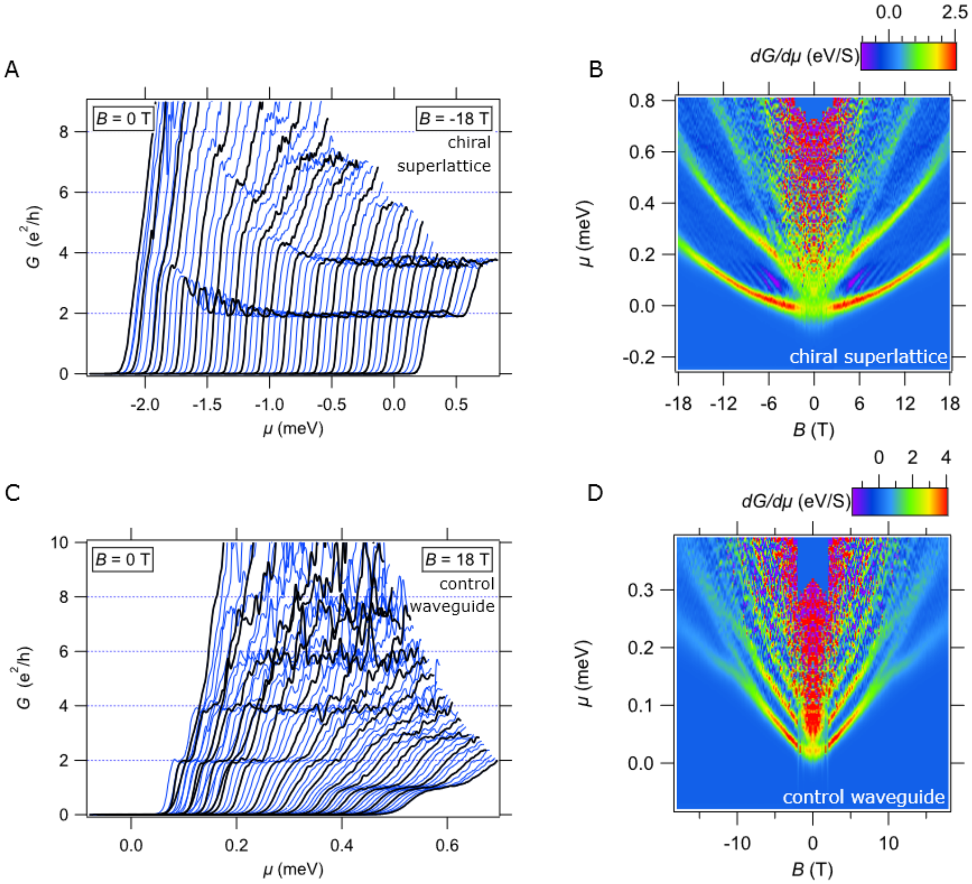

Figure 5.2: Experimental transconductance measurements showing the enhanced pairing and conductance oscillations above $2e^2/h$ in the helical waveguide compared to the control waveguide. Figure adapted from the Doctoral Thesis *Experimental Solid State Quantum Simulation Using 1D Superlattice Structures* by Megan Briggeman [49]. (A) and (C) are measurements of the conductance as a function of magnetic field, with each line representing a different magnetic field. These "waterfall plots" nicely show the plateaus in conductance appearing. (B) and (D) show the respective transconductances in the (B, μ_{SG}) parameter space.

dependent change in the centre of motion of the y trapping potential, reading

$$H_{lat} = \frac{m_y}{2}\omega_y^2(y - A_y \sin Qx)^2 \mathbb{I}_\sigma, \tag{5.3}$$

where A_z is the amplitude of the lateral modulation, with units of position.

$H_0 + H_{ver} + H_{lat}$ is diagonalised similarly to the procedure in Ch. 2.3. The wavefunction is written as a product of harmonic oscillator states and Bloch functions, which forms a convenient basis for this problem

$$\psi \equiv \psi_{k,n_y,n_z,\sigma}(x,y,z) = \sum_G u_{k\sigma}^G e^{i(k+G)x} \phi_{n_y}(y - \tilde{y_0}) \phi_{n_z}(z)|\sigma\rangle, \tag{5.4}$$

where $\phi_{n_y}(y - \tilde{y_0})$ is in principle x dependent (at this stage, $\tilde{y_0}$ is unknown). However, since the modulation amplitude (10nm) is small compared to the width of the waveguide ($l_y = 26$nm), deviations from an x-independent harmonic oscillator are expected to be small, and so this contribution is neglected. Combining the approach to solving for the band structure in Sec. 2.3 with the approach to the straight waveguide shown in Sec. 3.1 leads to the matrix equation

$$\begin{pmatrix} T_{k,n_y,n_z}^{G+2Q} & A_-^{G+2Q} & Y & 0 & 0 \\ A_+^{G+Q} & T_{k,n_y,n_z}^{G+Q} & A_-^{G+Q} & Y & 0 \\ Y & A_+^G & T_{k,n_y,n_z}^G & A_-^G & Y \\ 0 & Y & A_+^{G-Q} & T_{k,n_y,n_z}^{G-Q} & A_-^{G-Q} \\ 0 & 0 & Y & A_+^{G-2Q} & T_{k,n_y,n_z}^{G-2Q} \end{pmatrix} \begin{pmatrix} U_k^{G+2Q} \\ U_k^{G+Q} \\ U_k^G \\ U_k^{G-Q} \\ U_k^{G-2Q} \end{pmatrix} = E \begin{pmatrix} U_k^{G+2Q} \\ U_k^{G+Q} \\ U_k^G \\ U_k^{G-Q} \\ U_k^{G-2Q} \end{pmatrix}, \tag{5.5}$$

where $U_k^R = (u_{k\uparrow}^R, u_{k\downarrow}^R)^T$ for index R denoting the Brillouin zone, $T_{k,n_y,n_z}^R = \text{diag}(t_{k,n_y,n_z,\uparrow}^R, t_{k,n_y,n_z,\downarrow}^R)$

for

$$t^R_{k,n_y,n_z,\sigma} = \left(1-\frac{\omega_c^2}{\Omega^2}\right)\frac{\hbar^2(k+R)^2}{2m_x} + \hbar\Omega\left(n_y+\frac{1}{2}\right) + \hbar\omega_z\left(2n_z+\frac{3}{2}\right)$$
$$-\mu_{SG} + \left(1-\frac{\omega_y^2}{\Omega^2}\right)\frac{m_y}{4}\omega_y^2 A_y^2 - g\frac{\mu_B}{2}B\sigma,$$

$A^R_\pm = \left(\mp i\frac{\omega_c^2\omega_y^2}{\Omega^2}\frac{\hbar m_y A_y}{eB}\left(k+\left(R\pm\frac{Q}{2}\right)\right)+\frac{A_z}{2}\right)\mathbb{I}$, and $Y = \left(1-\frac{\omega_y^2}{\Omega^2}\right)\frac{m_y}{8}\omega_y^2 A_y^2\mathbb{I}$. The y eigenfunction in Eq. (5.4) is, under the approximations previously discussed, found to be

$$\phi_{n_y}(y-\tilde{y_0}) \approx \left(\frac{m_y\Omega}{\pi\hbar}\right)^{\frac{1}{4}}\frac{1}{\sqrt{2^{n_y}n_y!}}e^{-\frac{m_y\Omega}{2\hbar}(y-\tilde{y_0})^2}H_{n_y}\left(\sqrt{\frac{m_y\Omega}{\hbar}}(y-\tilde{y_0})\right), \tag{5.6}$$

where $H_n(\beta)$ denotes the nth Hermite polynomial in β, $\tilde{y}_0 = \frac{\omega_c^2}{\Omega^2}y_0 + \frac{\omega_y^2}{\Omega^2}A_y\sin Qx$, with ω_c, Ω, and y_0 retaining their definitions from Sec. 3.1. This is important to detail as it will be used in the following section when we discuss spin-orbit coupling.

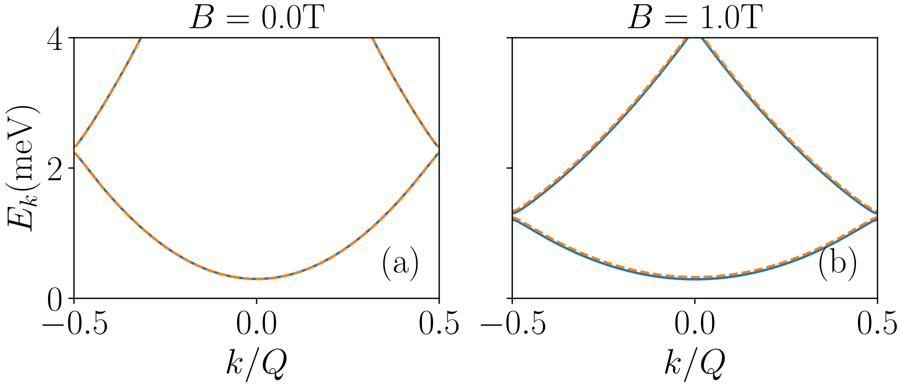

Figure 5.3: Band structures for the helical waveguide ($A_y = 10$nm, $A_z = 0.1$meV for zero spin-orbit coupling (a) without and (b) with magnetic field $B = 1$T. The blue and orange-dashed lines are the spin-down and spin-up respectively. Other parameters are $m_x = m_y = 1.9m_e$, $m_z = 6.5m_e$, $l_y = 26$nm, $l_z = 8.1$nm, $\lambda = 10$nm, and $g = 0.6$.

The band structures are generated by solving Eq. (5.5) for $k \in [-Q/2, Q/2)$. Results of this are displayed in Fig. 5.3. The A_z modulation behaves exactly as expected, opening up a gap on the order of A_z at the Brillouin zone edges $k/Q = \pm 0.5$. Secondly, the magnetic field flattens out the band structure as reported in Sec. 3.1, which has the effect of bringing down the band gap in energy. However, there is no effect from the A_y modulation, which would be expected to introduce band gaps in the centre of the Brillouin zone due to the Q/2 shift in momentum appearing in $A^R_{\pm}$. However, this term is exactly 0 at $B = 0$, and at $B = 1$T is ~ 0.1meV for $A_y = 10$nm, but is stronger at higher k values. Since we restrict to only low energies and thus low k in this thesis, the A_y modulation does not strongly affect the transport features of interest.

5.1.2 Adding Spin-Orbit Coupling

Fully including both the spin-orbit couplings as discussed in Ch. 4 results in the addition of

$$H_{SOC} = \frac{(\alpha_v \sigma_y - \alpha_l \sigma_z)}{\hbar}(p_x - eBy) \tag{5.7}$$

to the Hamiltonian. The same treatment is now performed, but explicitly using Eq. (5.4) as the y basis functions, giving

$$\begin{aligned} E_{SOC} = & \sum_{q'} a_{q',\sigma'} (\alpha_v \langle \sigma | \sigma_y | \sigma' \rangle - \alpha_l \langle \sigma | \sigma_z | \sigma' \rangle) \\ & \times \left(q' \delta_{q,q'} - \frac{eB}{\hbar} \left(\int \mathrm{d}x e^{i(q'-q)x} \tilde{y}_0 + \int \mathrm{d}\beta \phi_n(\beta) \beta \phi_{n'}(\beta) \right) \right), \end{aligned} \tag{5.8}$$

where $\beta = y - \tilde{y}_0$ has been defined for convenience. The last term in this equation is an inter-band coupling which is introduced by the spin-orbit coupling. We neglect this term due to the approximation of the wavefunction as being separable into a harmonic oscillator along y and Bloch waves along x. Relaxing this approximation would lead to a similar effect with coupling between other modes, and since this is assumed to be small due to the modulation (since the amplitude 10nm is small compared to the width 26nm) then the inter-band effects from the associated spin-orbit coupling are expected to also be small. Evaluating the rest of the expression gives

$$\begin{aligned} E_{SOC} =& i\sigma\alpha_v \left[i\frac{eB}{2\hbar}\frac{\omega_y^2}{\Omega^2}A_y \left(a_{q+Q,\bar{\sigma}} - a_{q-Q,\bar{\sigma}}\right) - \left(1-\frac{\omega_c^2}{\Omega^2}\right) q a_{q,\bar{\sigma}} \right] \\ &+ \alpha_l\sigma \left[i\frac{eB}{2\hbar}\frac{\omega_y^2}{\Omega^2}A_y \left(a_{q+Q,\sigma} - a_{q-Q,\sigma}\right) - \left(1-\frac{\omega_c^2}{\Omega^2}\right) q a_{q,\sigma} \right], \end{aligned} \tag{5.9}$$

where $\bar{\uparrow} = \downarrow$ and $\bar{\downarrow} = \uparrow$. This term can then be included in the matrix representation in Eq. (5.5).

Fig. 5.4 shows the effect that including spin-orbit coupling has on the band structure at $B = 1$T. The columns denote two different vertical spin-orbit coupling strengths $\alpha_v = [0.0, 2.0]$meVnm and the rows denote two different lateral spin-orbit coupling strengths $\alpha_l = [0.0, 2.0]$meVnm. In both cases, the spin-orbit coupling essentially splits the single Brillouin-zone into two centered away from $k = 0$, shifting where the band gap occurs in the spectrum. This is the same behaviour as was seen in the Kronig-Penney model when adding spin-orbit coupling. Additionally, the lateral-modulation-induced spin-orbit coupling induces an asymmetry in the band structure as was noted in Ch. 4. The A_y contribution is too small to have a large effect on the band structure in the energy range considered, as discussed also for Fig. 5.3. The amplitude of the modulation could be increased, but this would cause the approximation of small A_y compared to the waveguide width to break down.

5.2 Interacting Helical Waveguide

To include the effects of the periodic modulations and interactions at the same time, we take a different approach to the construction of a mean-field theory than the one

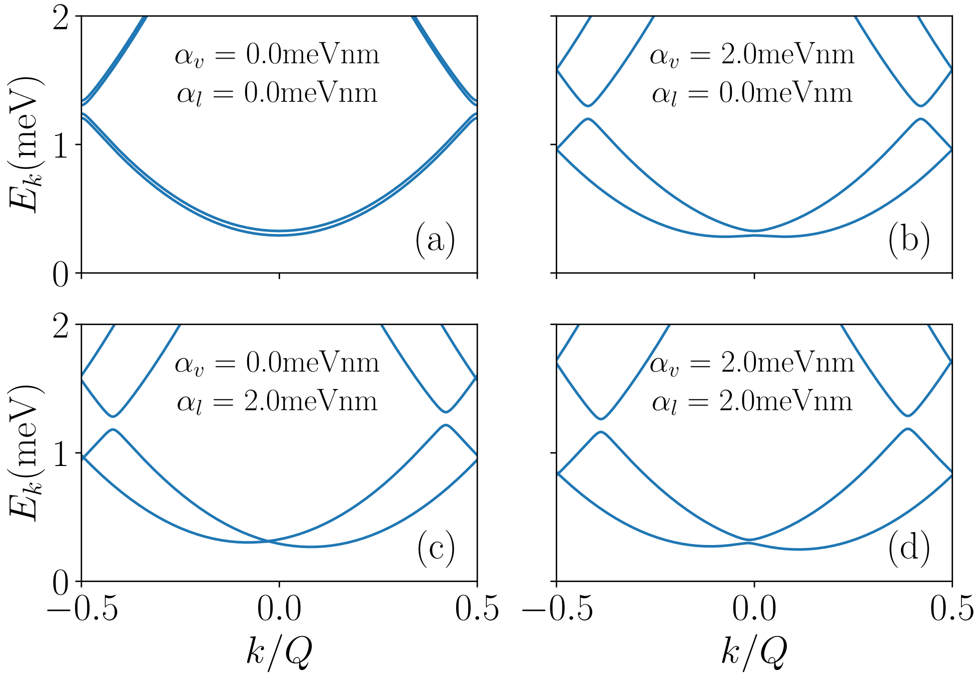

Figure 5.4: Band structures for the helical waveguide as in Fig. 5.3 with the addition of spin-orbit coupling. The left column is for $\alpha_v = 0.0$meVnm and the right for $\alpha_v = 2.0$meVnm. The top row is for $\alpha_l = 0.0$meVnm and the bottom for $\alpha_l = 2.0$meVnm. The other parameters read $m_x = m_y = 1.9m_e$, $m_z = 6.5m_e$, $l_y = 26$nm, $l_z = 8.1$nm, $\lambda = 10$nm, and $g = 0.6$. Throughout, $B = 1$T.

taken in the previous chapters. Recalling Bloch's theorem [63] which reads

$$\psi_k(x) = \sum_G u_k^G e^{i(k+G)x},$$

the goal is to define an operator such that $\Psi(x)\left|0\right\rangle = \psi(x)$, where $\left|0\right\rangle$ is the vacuum state. A natural choice of this definition is

$$\Psi_k(x) = \sum_G c_k^G e^{i(k+G)x}, \tag{5.10}$$

where c_k^G is an operator that creates an electron from the vacuum state at quasimomentum k in Brillouin zone G with weighting u_k^G. In essence, the field operator has been expanded in a basis of Bloch operators rather than plane waves. Including the other quantum numbers of interest (neglecting z direction in the notation as it will not be varied here), the field operator reads

$$\Psi_{k,n_y}(x,y) = \begin{pmatrix} \Psi_{k,n_y,\uparrow}(x,y) \\ \Psi_{k,n_y,\downarrow}(x,y) \end{pmatrix} = \sum_G e^{i(k+G)x}\phi(y) \begin{pmatrix} c_{k,n_y,\uparrow}^G \\ c_{k,n_y,\downarrow}^G \end{pmatrix}, \tag{5.11}$$

and the total many-body Hamiltonian with contact interactions becomes

$$\begin{aligned} \mathcal{H} =& \sum_{k,G}\sum_{\sigma}\left(t_{k,n_y,\sigma}^G + \Sigma_{n_y,\bar{\sigma}} - \sigma A_{k,l}^G\right) c_{k,n_y,\sigma}^{G\dagger} c_{k,n_y,\sigma}^G - (\chi_{n_y}^* - iA_{k,v}^G) c_{k,n_y,\downarrow}^{G\dagger} c_{k,n_y,\uparrow}^G \\ & -(\chi_{n_y} + iA_{k,v}^G) c_{k,n_y,\uparrow}^{G\dagger} c_{k,n_y,\downarrow}^G + \Delta_{n_y}\left(c_{k,n_y,\uparrow}^{G\dagger} c_{-k,n_y,\downarrow}^{-G\dagger} - c_{k,n_y,\uparrow}^G c_{-k,n_y,\downarrow}^{-G}\right) \\ & -\sum_{\sigma} Y c_{k,n_y,\sigma}^{G\dagger}\left(c_{k,n_y\sigma}^{G-2Q} + c_{k,n_y\sigma}^{G+2Q}\right) + \sum_{\sigma,\tau} A_{k,\sigma,\tau}^G c_{k,n_y,\sigma}^{G\dagger} c_{k,n_y,\sigma}^{G+\tau Q} - \sum_{\sigma,\tau} \sigma\tau D_v c_{k,n_y,\sigma}^{G\dagger} c_{k,n_y,\sigma'}^{G-\tau Q}, \end{aligned} \tag{5.12}$$

where $\bar{\sigma}$ denotes the opposite spin to σ. New notations have been defined to keep the equations concise. $A_{k,\eta}^G = J_c\alpha_\eta(k+G)$ is the spin-orbit coupling with $\eta = \{v, l\}$ denoting the direction, and $J_\kappa = 1 - \omega_\kappa^2/\Omega^2$ where $\kappa = \{c, y\}$ denotes whether this refers to the cylotron frequency ω_c or the bare y trapping frequency ω_y. Additionally, we utilise $\tau = \pm 1$ (is not a physical quantity and is used to keep the correct signs) to write $A_{k,\sigma,\tau}^R = A_\tau^R - i\sigma D_l$. $t_{k,n_y,\sigma}^G$, A_τ^R and Y are kept as defined in the single particle case, $D_\eta = \frac{eB}{\hbar}\frac{\omega_y^2}{\Omega^2}\frac{A_y}{2}\alpha_\eta$. The mean fields now read

$$\Sigma_{n_y,\sigma} = \frac{U}{2\pi}\sum_G \int \mathrm{d}k \langle c_{k,n_y,\bar{\sigma}}^{G\dagger} c_{k,n_y,\bar{\sigma}}^G \rangle, \tag{5.13}$$

$$\chi_{n_y} = \frac{U}{2\pi} \sum_G \int \mathrm{d}k \langle c^{G\dagger}_{k,n_y,\downarrow} c^G_{k,n_y,\uparrow} \rangle, \tag{5.14}$$

and

$$\Delta_{n_y} = \frac{U}{2\pi} \sum_G \int \mathrm{d}k \langle c^{-G}_{-k,n_y,\downarrow} c^G_{k,n_y,\uparrow} \rangle. \tag{5.15}$$

Eq. (5.12) is quadratic and can thus be diagonalised, and the self-consistent approach outlined in previous chapters can be used. Throughout, $T = 25\text{mK}$ is used.

First, in order to understand the changes when a periodic potential is introduced into the interacting calculation, we study solely the interplay between a Kronig-Penney type potential ($A_z > 0$) and electron-electron interactions. Fig. 5.5 displays the correlation functions which make up the mean fields as a function of quasimomentum k around the Brillouin zone edge, with the band structure in each regime displayed below.

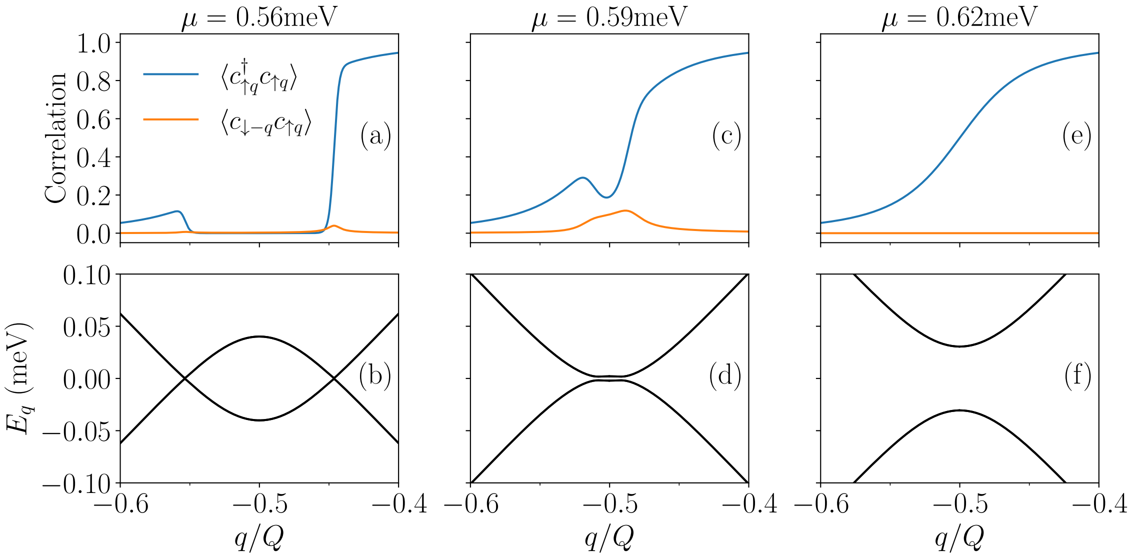

Figure 5.5: Correlation functions and excitation spectra as a function of q around the left edge of the Brillouin zone at $\mu_{SG} = 0.56$, $\mu_{SG} = 0.59$meV, and $\mu_{SG} = 0.62$meV for vertical modulation only. Waveguide parameters are $m_x = m_y = 1.9m_e$, $m_z = 6.5m_e$, $l_y = 26$nm, $l_z = 8.1$nm, $B = 0$T, $\lambda = 10$nm, and $U = -2.0$meVnm.

In Fig. 5.5a, far from the Kronig-Penney gap ($\mu_{SG} = 0.56$meV) but also far from the bottom of the energy band, the pairing (orange) is small, even at its peak at $q/Q = -0.45$. Also seen are effects from the periodic structure appearing in the occupation (blue), as there is a contribution from a Fermi point on the other side of the Brillouin zone edge at $q/Q = -0.56$. As the chemical potential is increased to just below the gap in Fig. 5.5c ($\mu_{SG} = 0.59$meV), a pairing peak appears around the B.Z. edge ($q/Q = -0.5$), which also appears to have a double peak structure coming from contributions either side of the B.Z. edge at roughly $q/Q = -0.48$ and $q/Q = -0.52$. Finally in Fig. 5.5e, as the chemical potential enters the band gap ($\mu_{SG} = 0.62$meV), the pairing completely vanishes and the occupation smooths out over the Brillouin zone edge $q/Q = -0.5$. This can be related to the the band structures corresponding to each correlation plot. The two Fermi points in Fig. 5.5b occur at the same values of momentum as the edges seen in the occupation correlations in Fig. 5.5a, at approximately $q/Q = -0.56$ and $q/Q = -0.44$. In Fig. 5.5d, a gap centred around the B.Z. edge $q/Q = -0.5$ forms, which is consistent with Fig. 5.5c having a non-zero pairing correlation. Finally in Fig. 5.5f, there is a large gap in the band structure at the B.Z. edge $q/Q = -0.5$. This is the Kronig-Penney gap and is the reason behind the disappearance of the pairing in Fig. 5.5e.

This gives a strong foundation for looking at the correlations for the helical waveguide. While these are more complicated, the basic features are the same, with additional features which were discussed in Sec. 4.3. These are displayed in Fig. 5.6. First, at both values of the chemical potential, a depletion of the occupations is observed, at $q/Q = \pm 0.2$ and $q/Q = \pm 0.4$ in Fig. 5.6c and at $q/Q = \pm 0.38$ $q/Q = \pm 0.59$ in Fig. 5.6d . In the case without spin-orbit coupling and interactions, these would be the Fermi edges at which the occupations would drop down to zero, but due to the spin-orbit coupling mixing the spins, they become associated with a superposition of both spins. This was also reported in [50], and is marked by the appearance of Fock terms.

Secondly, the appearance of triplet pairing (in green), which has been shown to arise from the σ_z spin-orbit coupling, is observed in Fig. 5.6e and Fig. 5.6f. This peaks at the Fermi points, around $q/Q = \pm 0.2$ and $q/Q = \pm 0.41$ in Fig. 5.6e, and around $q/Q = \pm 0.38$ and $q/Q = \pm 0.59$ in Fig. 5.6f. These can be associated to the Fermi points by looking at the Fermi energy in the band structures in Fig. 5.6a and Fig. 5.6b, respectively. This appearance of triplet pairing is due to the asymmetry introduced into the spectrum by the interplay between the lateral-modulation-induced spin-orbit coupling and the magnetic field, which breaks the symmetry $E_k = -E_k$ (note that we still have particle hole symmetry $E_k = -E_{-k}$). As in the previous section, when the Fermi energy is far from the Brillouin zone edges, we do not see strong changes to the expected correlation spectrum in Fig. 5.6c and Fig. 5.6e. However, when we approach the band gap we begin to see contributions from both sides of the Brillouin zone edge Fig. 5.6d and Fig. 5.6f, seeing peaks at $k/Q = \pm 0.42$ and $k/Q = \pm 0.62$. All of these features can be matched to the interacting equivalent of Fermi points in the excitation spectra in Fig. 5.6a, marking closest approaches of the bands to the Fermi energy.

Notable also is the splitting of the pairing peaks into two in Fig. 5.6f. This also occurs due to the asymmetry - the offset of the bands results in a double-crossing of the Fermi energy centred around the aforementioned points, as each gap point no longer occurs at the Fermi energy but rather is slightly offset from the Fermi energy.

Now that the correlation functions have been understood in detail, the overall mean fields can be studied. We display these in the full (B, μ_{SG}) parameter space in Fig. 5.7. First, turning on just the spin-orbit couplings leads to a slight enhancement of the pairing area and pairing field, but this is not extremely large due to the splitting

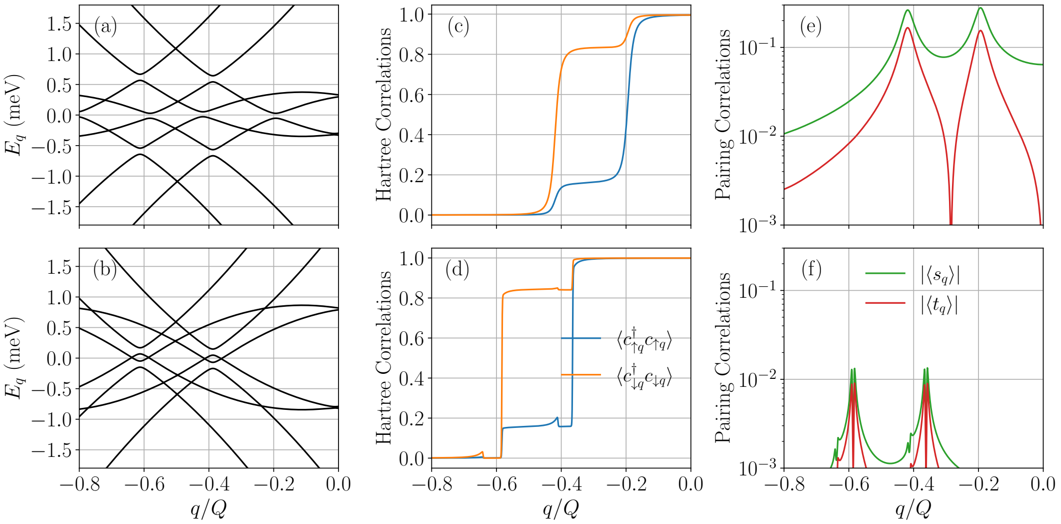

Figure 5.6: Excitation spectra and band structures for the helical waveguide with $U = -4.0$meVnm, $\alpha_l = \alpha_v = 2.0$meVnm, $A_y = 10$nm, and $A_z = 0.2$meV, as a function of the momentum q in an extended zone scheme, focusing on one side of the Fermi surface. a) Excitation spectrum at $\mu_{SG} = 0.45$meV. b) Excitation spectrum at $\mu_{SG} = 0.85$meV. c) Hartree correlations at $\mu_{SG} = 0.45$meV. d) Hartree correlations at $\mu = 0.85$meV. e) Pairing correlations on a log scale at $\mu_{SG} = 0.45$meV. f) Pairing correlations on a log scale at $\mu_{SG} = 0.85$meV. In orange and blue, we display the occupations of spin-up and spin-down respectively, and in red and green the absolute value of the expectation of the singlet and triplet pair operators defined as $s_q = c_{-q\downarrow}c_{q\uparrow} - c_{-q\uparrow}c_{q\downarrow}$ and $t_q = c_{-q\downarrow}c_{q\uparrow} + c_{-q\uparrow}c_{q\downarrow}$. Waveguide parameters are $m_x = m_y = 1.9m_e$, $m_z = 6.5m_e$, $l_y = 26$nm, $l_z = 8.1$nm, $\lambda = 10$nm, and $g = 0.6$.

into the singlet and triplet components, with the triplet energy contributing zero due to it averaging out in the integration [50]. This can be seen by looking at the furthest extension of the pairing as a function of magnetic field between Fig. 5.7a and Fig. 5.7b. However, when the associated modulations are introduced together with this in Fig. 5.7c, a very significant enhancement of the pairing area up to over 6T is observed, which is consistent with experiment [47]. Additionally, the effect of the Kronig-Penney gap on the pairing is strongly seen as it produces a curve in the phase boundary from around (B =1.6T, $\mu_{SG} = 0.8$meV) to approximately ($B = 4$T, $\mu_{SG} = 0.4$meV) where the pairing drops, in some regions to zero. The value of this trough seems to be related to the value of the pairing around it since the regions where the original pairing is lower are where we obtain precisely zero pairing in the gapped region (compare the region around (B =1.8T, $\mu_{SG} = 0.8$meV) to the region around (B = 2T, $\mu_{SG} = 0.5$meV). This is likely due to a competition between the Kronig-Penney gap, which suppresses the transport, and the pairing gap which leads to transport of pairs.

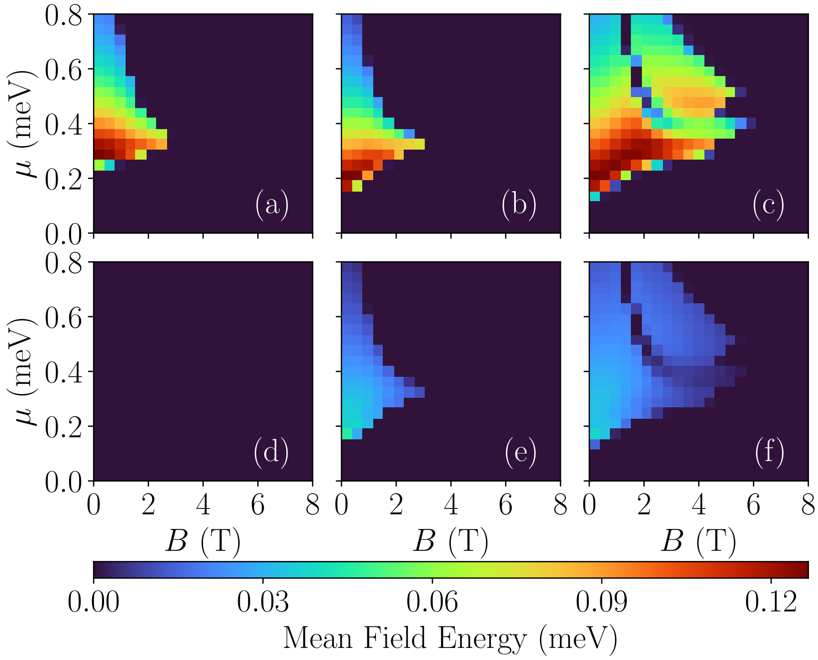

Figure 5.7: Singlet pairing as a function of magnetic field B (x axis) and chemical potential μ_{SG} (y-axis) at $U = -5.0$meVnm for (a) straight waveguide, (b) Spin-orbit coupled waveguide with $\alpha_v = \alpha_l = 2.0$meVnm, and (c) helical waveguide with $A_y = 10$nm and $A_z = 0.2$meV (including spin-orbit couplings in (b). (d) is the triplet pairing corresponding to singlet pairing (a), (e) is the triplet pairing corresponding to singlet pairing in (b), and (f) is the triplet pairing corresponding to the singlet pairing in (c). Waveguide parameters are $m_x = m_y = 1.9m_e$, $m_z = 6.5m_e$, $l_y = 26$nm, $l_z = 8.1$nm, $\lambda = 10$nm, and $g = 0.6$.

Additionally, the same effects are analysed for the triplet pairing. This does not appear when spin-orbit coupling is not present, as in Fig. 5.7d, and appears in the region of pairing in Fig. 5.7e and Fig. 5.7f. A gap occurs in Fig. 5.7f in the same position in parameter space as Fig. 5.7e. Thus, in this model for the helical waveguide, there is a significant conversion of singlet pairs into triplet pairs as a result of the σ_z spin-orbit coupling, which is stable up to high magnetic fields and sensitive to the Kronig-Penney gap.

While the distinction between singlet and triplet pairing cannot be seen in experiment by looking at the conductance baseline, these plots show that the potential modulation does significantly enhance the pairing in the waveguide region. In order to show that triplet pairs do indeed occur experimentally, a more complicated theoretical model is required. This is the goal of the next section, where we will see that triplet pairing could be the cause of the conductance oscillations.

5.3 Scattering Calculations

The goal of this section is to model the oscillations in conductance seen in experiment. These take place on a baseline of $2e^2/h$ up to $4e^2/h$ in a region that appears to be strongly paired, so a natural assumption is that these oscillations are due to the effects of electron-electron interactions. This is made more convincing by the fact that these oscillations do not appear in straight waveguides. However, due to the mean-field approximation, it is not straight-forward to write down a first-principles time dependent model for these features. In order to build on the mean-field theory discussed in the rest of the chapter, a phenomenological model for these conductance oscillations is introduced.

Oscillations in transport phenomena are often the result of scattering. In order to study the oscillations in the conductance, we utilise a scattering model based on [75]. However, unlike in Ref. [75], which considers single particle scattering, the waveguide electrons are paired. Thus, some changes must be made to the model in order to make sure this is used correctly.

The phenomenological scattering model considers mean-field theory as determining which pairing channels are available. If Δ is above the thermal threshold, then this allows the singlet pair channel to support transport. Additionally, if triplet pairing is supported by the waveguide in a parameter regime, this too is considered available. Each electron, however, can only contribute a maximum of e^2/h to the conductance. Using these rules, a properly normalized input state for right-moving channels is produced (the left-moving input state is assumed to be zero). Then, it evolves under a single scattering "event", which is described by the scattering matrix

$$\mathcal{S} = e^{ia}, \tag{5.16}$$

where the coefficients of the off diagonal blocks of the matrix a are given by

$$a^J_{m,n} = -\frac{m_x}{\hbar^2}\frac{1}{\sqrt{k^J_m k^J_n}}\int \mathrm{d}x \psi^{J\dagger}_m(x)V(x)\psi^J_n(x). \tag{5.17}$$

There are three points to address here. The first is the nature of the scattering event, which will be discussed in 5.3.1. The second is the definition of k^J_m in the case where the scattered particles are electron pairs, and is the subject of 5.3.2. The third and final is the definition of $\psi^J_m(x)$, which will be provided in 5.3.3.

5.3.1 Physical Model – Triplet Scattering

Regarding the scattering that occurs in the waveguide, we refer back to the experimental setup. As discussed in Sec. 1.3, the waveguide region is attached to two leads. In the helical waveguide experimental setup, the helical region is only a portion of the full waveguide, with the rest being unmodulated.

Only the helical region supports triplet pairing, with the unmodulated regions on either side only having singlet channels available. Thus, the proposed model is that triplet pairs in the helical region are scattered upon contact with the interface between helical and unmodulated regions. Triplet pairs can be backscattered, reducing the conductance. As such, in order to obtain conductances of up to $4e^2/h$, the lowest two energy bands $n_y = 0$ and $n_y = 1$ must be included. This idea is illustrated in Fig. 5.8.

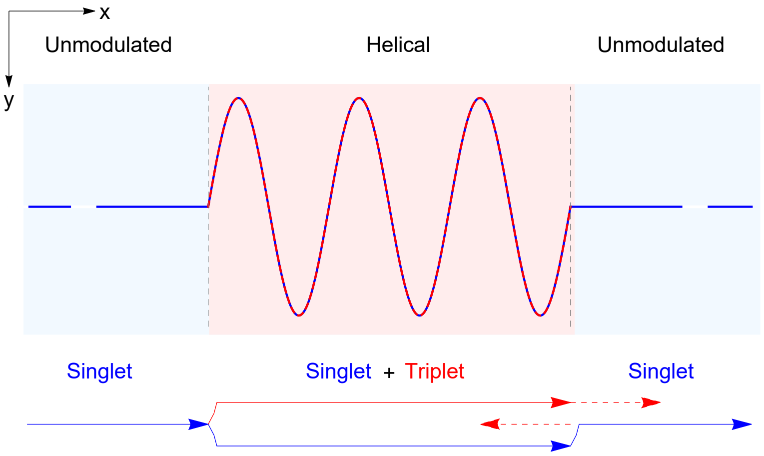

Figure 5.8: Diagram of the scattering setup considered in the phenomenological model described in this section. Triplet pairs incident on the boundary between helical (allowed) and unmodulated (disallowed) regions can be backscattered by an effective potential at the boundary. The broken sections in the left and right unmodulated regions denote the transparent tunnelling barriers required in experiment to observe clean quantised conductance features, but are not relevant to the calculations performed within this work.

Using this setup, the scattering model is expected to give conductance oscillations between 0 and 4 in units of e^2/h, with the singlets giving a stable total of $2e^2/h$. So in principle, the experimental features we aim to describe could be reproduced by this model.

5.3.2 Scattering Momentum

The goal of the current section is to determine a suitable momentum for the scattering calculations. In the singlet case, it is clear that this should be proportional to Δ. But the Δ for triplet pairing is zero. This must be generalised. Here, we propose that

$$k_\Delta = \frac{1}{2\pi}\int_{-\infty}^{\infty} \mathrm{d}k\, |\langle c_{-k\downarrow} c_{k\uparrow}\rangle| \tag{5.18}$$

is a suitable momentum to use within this scattering model.

To justify this, we begin with a standard BCS theory [65] with the chemical potential rescaled by the Hartree shifts. The Hamiltonian takes the form

$$H = \sum_k \varepsilon_k c^\dagger_{\sigma k} c_{\sigma k} + \Delta(c^\dagger_{k\uparrow} c^\dagger_{-k\downarrow} + c_{k\downarrow} c_{-k\uparrow}), \tag{5.19}$$

which in matrix form is

$$H = \begin{pmatrix} \varepsilon_k & \Delta \\ \Delta & -\varepsilon_k \end{pmatrix}, \tag{5.20}$$

where $\varepsilon_k = \epsilon_k - \tilde{\mu}$, ϵ_k is the usual kinetic energy term, $\tilde{\mu}$ is the rescaled chemical potential including the Hartree shifts, and Δ is the pairing gap, obeying the self-consistent equation

$$\Delta = \frac{U}{2\pi}\int \mathrm{d}k \langle c_{-k\downarrow} c_{k\uparrow}\rangle. \tag{5.21}$$

First, the coherence length, roughly the "size" of a Cooper pair, is defined as [65]

$$\xi = \frac{\hbar v_F}{\pi\Delta} = \frac{\hbar^2 k_F}{m\pi\Delta}, \tag{5.22}$$

where v_F and k_F are the Fermi velocity and momentum respectively. This is much more complicated to determine outside of BCS theory, where there are multiple Fermi velocities, and non-zero values of Δ for triplet pairs. However, this allows an effective momentum for pairs to be defined as

$$k_\xi = 1/\xi = \frac{m\pi\Delta}{\hbar^2 k_F}. \tag{5.23}$$

The results of this are displayed in Fig 5.9. The inverse of the coherence length behaves very similarly to the integral of the absolute value of the pairing correlation.

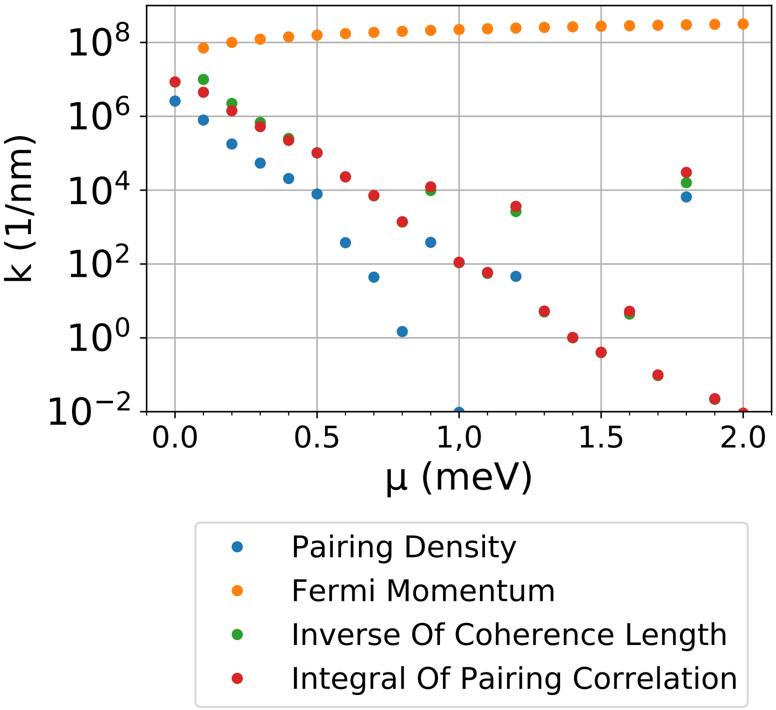

Figure 5.9: Plots of possible quantities that could work as momenta for the scattering calculations, as a function of chemical potential μ_{SG}. The original idea of using the pair density (blue), has the same trend as the inverse of coherence length (green), but is quite far away in magnitude. However, the same integral but without the square (red) is much closer. This simulation uses $m = m_e$ and $U = -2.0$meVnm.

To integrate this, the standard BCS Bogoliubov transformation is performed, turning the integral into

$$k_\Delta = \frac{|\Delta|}{2\pi}\int_0^\infty \frac{\mathrm{d}k}{\sqrt{\varepsilon_k^2+\Delta^2}}. \tag{5.24}$$

We make a change in variables using the density of states $\rho(\varepsilon_k) = \frac{\mathrm{d}k}{\mathrm{d}\varepsilon_k} = \frac{m}{\hbar^2 k}$. Inserting this and imposing a high frequency cutoff at the Debye frequency gives

$$k_\Delta = \frac{|\Delta| m\pi}{\hbar^2 k_F}\frac{1}{2\pi^2}\int_0^{\hbar\omega_D} \frac{\mathrm{d}\varepsilon_k}{\sqrt{\varepsilon_k^2+\Delta^2}} = \frac{k_\xi}{2\pi^2}\int_0^{\hbar\omega_D} \frac{\mathrm{d}\varepsilon_k}{\sqrt{\varepsilon_k^2+\Delta^2}}. \tag{5.25}$$

Performing the integral gives

$$k_\Delta = \frac{k_\xi}{2\pi^2}\tanh^{-1}\left(\frac{\hbar\omega_D}{\sqrt{\hbar^2\omega_D^2+\Delta^2}}\right). \tag{5.26}$$

This can vary a lot depending on the Debye frequency and Δ. However, the zero pairing cutoff is defined as $\Delta = 10^{-3}$meV as this is the order of the thermal fluctuations in the experimental parameter regimes. In bulk STO, the value of the Debye energy is 34.5meV [76]. Using these parameters gives

$$\frac{1}{2\pi^2}\tanh^{-1}\left(\frac{\hbar\omega_D}{\sqrt{\hbar^2\omega_D^2+\Delta^2}}\right) \lesssim 1.77.$$

This shows that k_Δ and k_ξ are approximately proportional to each other, and of the same order of magnitude, making k_Δ a suitable momentum which can be generalised to the case beyond BCS theory.

As such, we define

$$k_m^J = \frac{1}{2\pi}\int \mathrm{d}k\,\left|\langle c_{\downarrow -km} c_{\uparrow km}\rangle + \mathrm{sgn}(J)\langle c_{\uparrow -km} c_{\downarrow km}\rangle\right|, \tag{5.27}$$

where J denotes singlet versus triplet, with $\mathrm{sgn}(\text{singlet}) = -1$ and $\mathrm{sgn}(\text{triplet}) = 1$, to be our scattering momentum.

5.3.3 Overlap

In order to solve the scattering model, a pair wavefunction must be defined. The wavefunction of interest can be written as

$$\psi_{m,J}(x) = \Psi^{\dagger}_{m,J}(x)\left|0\right\rangle = \sum_{q} e^{iqx} J^{\dagger}_{m,q}\left|0\right\rangle , \tag{5.28}$$

where $\Psi^{\dagger}_{m,J}(x)$ creates a pair with character $J = \{s, t\}$ (singlet or triplet) in mode m at position x, and $J^{\dagger}_{m,q}$ creates a pair with character J at momentum q in mode m. The form of this operator is

$$J_{m,q} = \frac{c_{-q,m,\downarrow}c_{q,m,\uparrow} + \mathrm{sgn}(J)c_{-q,m,\uparrow}c_{q,m,\downarrow}}{2}.$$

The overlap integral is

$$\mathcal{I} = \int \mathrm{d}x \psi^{\dagger}_{m,J}(x) V(x) \psi_{n,J}(x). \tag{5.29}$$

The proposed model concerns the scattering of triplets at the boundary between helical and unmodulated regions. Thus, the potential is $V(x) = V_0\delta(x - L)$ for triplets and $V(x) = 0$ for singlets. Then, Eq. 5.29 becomes

$$\begin{aligned} \mathcal{I} &= V_0 \psi^{\dagger}_{m,t}(L)\psi_{n,t}(L) \qquad (5.30) \\ &= V_0 \sum_{q,k} e^{i(q-k)L} \langle t_{k,m} t^{\dagger}_{q,n} \rangle. \end{aligned}$$

This is expanded using the same mean-field techniques as above to express this in terms of the correlation functions obtained from the Hartree-Bogoliubov model

$$\begin{aligned}\mathcal{I} =& \frac{V_0}{2}\sum_q \Bigg\{ \sum_k 2e^{i(q-k)L}\langle t_{k,m}\rangle\langle t^{\dagger}_{q,n}\rangle \\ &+(1-\cos 2qL)\left[\langle c_{q,m,\downarrow}c^{\dagger}_{q,n,\uparrow}\rangle\langle c_{-q,m,\uparrow}c^{\dagger}_{-q,n\downarrow}\rangle + \langle c_{q,m,\downarrow}c^{\dagger}_{q,n,\downarrow}\rangle\langle c_{-q,m,\uparrow}c^{\dagger}_{-q,n,\uparrow}\rangle\right]\Bigg\}.\end{aligned} \tag{5.31}$$

5.3.4 Conductance From Scattering

The Scattering Matrix $\mathcal{S}_{LR}$ has the following action

$$\begin{pmatrix}\mathbf{A_R}\\ \mathbf{B_L}\end{pmatrix} = \mathcal{S}_{LR}\begin{pmatrix}\mathbf{A_L}\\ \mathbf{B_R}\end{pmatrix}, \tag{5.32}$$

where $\mathbf{A_L}$ is the input from the left lead, $\mathbf{B_R}$ is the input from the right lead, $\mathbf{A_R}$ is the output from the right lead, and $\mathbf{B_L}$ is the output from the left lead. Of interest is the right-moving transport - what comes out at the right lead when electrons are injected (or in this case, pairs of electrons) at the left lead. As such, $\mathbf{B_R} = \mathbf{0}$, and we want to calculate $\mathbf{A_R}$. This is a vector of transmission coefficients - if this was a single particle model, the components of this vector would be fed into the Landauer-Buttiker model as transmission coefficients, which would read

$$G = \frac{e^2}{h}\sum_n |a^R_n|^2, \tag{5.33}$$

where a^R_n is the nth element of $\mathbf{A_R}$ with n labelling different spin-channels and transverse modes, in this model. The input vector is not a normalized wavefunction.

In the case where an electron is input into every scattering channel available, $\mathbf{A_L} = \mathbf{1}$ As such, $0 \leq |a_n^R|^2 \leq 1$ is required for these to be transmission coefficients. If the same treatment is performed for the scattering model of pairs, pairs are expected to give $2e^2/h$ conductance [24], and so the conductance becomes

$$G = \frac{2e^2}{h} \sum_n |a_n^R|^2, \tag{5.34}$$

where $0 \leq |a_n^R|^2 \leq 1$.

This works well if each pair channel is independent. However, when there are singlet and triplet pairs in the same mode, this is no longer the case. Extending the notation, and for now only looking at the case where both pairing electrons are in the same mode for each pair, the desired condition is

$$|a_{n,s}^L|^2 + |a_{n,t}^L|^2 = 1,$$

where s and t denote the singlet and triplet modes, and n the y harmonic oscillator state (with z being neglected as $n_z = 0$ throughout). If there are only singlet pairs (vertical waveguide) then this reduces to the same conductances as obtained in Ch 3.3. The components could be weighted by their densities, but to make this simpler a 50/50 split of singlet and triplet conductance (this most easily gives a $2e^2/h$ baseline with oscillations on top) is taken. So, in this case, $a_{n,s}^L = a_{n,t}^L = \frac{1}{\sqrt{2}}$.

In the end, this means that $|a_{n,s}^R|^2 = 1/2$ and $0 \leq |a_{n,t}^R|^2 \leq 1/2$, so for two modes this gives

$$G = 2\frac{e^2}{h} + 2\frac{e^2}{h}\left(|a_{0,t}^R|^2 + |a_{1,t}^R|^2\right),$$

where $0 \leq |a_{0,t}^R|^2 + |a_{1,t}^R|^2 \leq 1$. Thus from this, stable singlets in the first two bands plus oscillating triplets from the first two bands could result in oscillations above a conductance baseline of $2e^2/h$.

5.3.5 Conductance Oscillations

All of this culminates in producing conductance plots using the scattering model, which is build on a multi-band version of the mean-field model. Since the scattering model only deals with pairs, in regions where there is no pairing, zero conductance is obtained. Thus, we are showing only the pairing contribution to the conductance in these plots, but in principle it should be possible to include the single-electron contributions via the Landauer formula.

This are presented in Fig. 5.10 in both linecut form at select magnetic fields and in the whole (B, μ_{SG}) parameter space with and without the triplet-inducing lateral modulation. In Fig. 5.10a, which shows the conductance as a function of μ_{SG} at various magnetic fields for the vertical modulation only, an stable plateau of $4e^2/h$ is observed. The decay of the plateau at high energies is not due to an actual decrease in conductance, but a result of pair breaking in these regimes. When the lateral modulation is included in Fig. 5.10b, the plateau consists of oscillations between $2e^2/h$ and $4e^2/h$. This effect is displayed across the (B, μ_{SG}) parameter space in Figs. 5.11a,b, where the oscillations in the helical waveguide disappear at high fields as pairs are broken. This is consistent with experimental observations.

5.3.6 Outlook

This model provides a zero-th order method of studying the oscillations in conductance observed in experiment. However, one potential issue is that of the interface between the left lead and the helical region - in principle, the backscattered part of the wavefunction should also scatter at this barrier, leading to a question of what

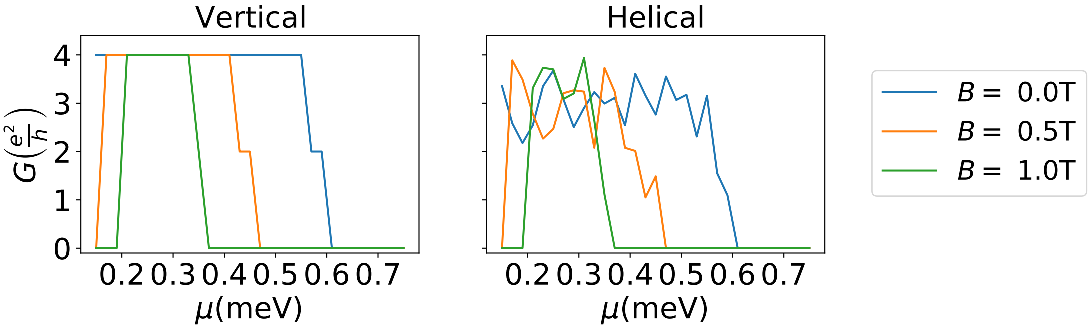

Figure 5.10: Linecuts of the conductance as a function of μ_{SG} from the scattering model for the vertical ($A_z = 0.1$meV, $\alpha_v = 2.0$meVnm) and helical ($A_y = 10$nm, $\alpha_l = 3.0$meVnm) waveguides for effective triplet scattering potential $V_0 = 0.03$meV and interaction strength $U = -4.0$meVnm. Waveguide parameters are $m_x = m_y = 1.9m_e$, $m_z = 6.5m_e$, $l_y = 26$nm, $l_z = 8.1$nm, $\lambda = 10$nm, and $g = 0.6$.

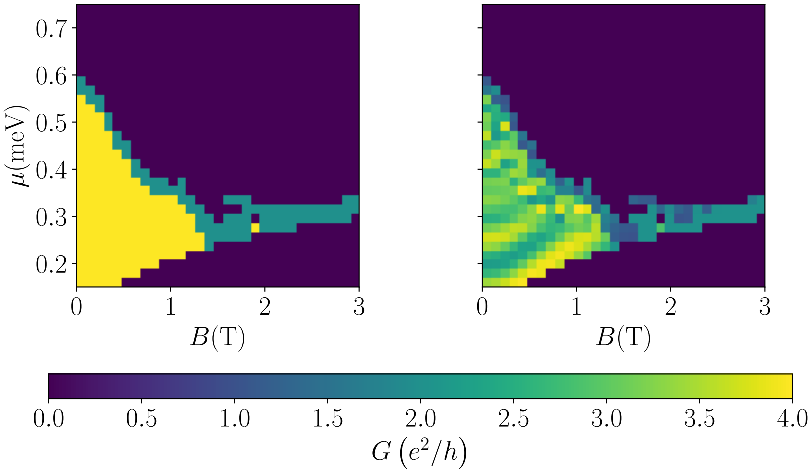

Figure 5.11: Conductance from the scattering model for the vertical ($A_z = 0.1$meV, $\alpha_v = 2.0$meVnm) and helical ($A_y = 10$nm, $\alpha_l = 3.0$meVnm) waveguides for effective triplet scattering potential $V_0 = 0.03$meV and interaction strength $U = -4.0$meVnm. Waveguide parameters are $m_x = m_y = 1.9m_e$, $m_z = 6.5m_e$, $l_y = 26$nm, $l_z = 8.1$nm, $\lambda = 10$nm, and $g = 0.6$.

happens to the wavefunction of the triplet trapped in the waveguide. This can be resolved by noting that in the actual system, rather than having a single superposition of singlet and triplet pieces, the wavefunction should actually undergo oscillations between these two states [77]. In this model, the scattering would become a boundary matching problem with the transported particles being bosonic electron pairs, and is analagous to the transport of spinful fermions between spin polarized wires. This treatment is performed in detail in a recently submitted paper, allowing for the estimation of the spin-orbit coupling strength engineered by the modulation [51].

5.4 Conclusion

In this chapter, we expanded the usual mean-field model in a Bloch basis instead of the usual plane wave expansion, allowing us to treat the effects of periodic modulations on electron-electron interactions. This allowed us to study the effect of helical modulations on electron transport, and we find that this leads to both significantly enhanced electron pairing and the introduction of triplet pairing into the waveguide region. The enhanced pairing is observed in experimental transconductance features via a strong initial peak of $2e^2/h$ which is stable up to $B = 18$T.

Additionally, we utilised a phenomenological pair scattering model to study the conductance oscillations. Proposing that this is a result of pair scattering at the helical-unmodulated interface, we were able to obtain conductance oscillations between $2e^2/h$ and $4e^2/h$, which is observed in experiment in helical LAO/STO nanowires [51].

Chapter 6

Conclusion

This thesis has presented my work on using mean-field theory to study electron-electron interactions in one-dimensional electron waveguides. I extended the usual Hartree-Fock-Bogoliubov formalism to include spin-orbit coupling and the effect of periodic modulations. Using these techniques, I showed that a significant enhancement of the pairing strength is introduced by Kronig-Penney modulation through both the form of the potential and the engineered spin-orbit interaction. This allows for the prospect of engineering paired electron phases in these systems. Additionally, triplet pairing has been observed when this formalism is applied to laterally-modulated waveguides. This could be useful in the study of the physical processes behind high T_c superconductivity as some unconventional superconductors display triplet pairing [78, 79], so being able to control it is an exciting prospect. Finally, I have used a phenomenological scattering model to offer an explanation as to the oscillations in the conductance observed in helically-modulated LAO/STO nanowires.

The approximation of the wavefunction being separated into Bloch waves along x and a harmonic oscillator along y, which allows for the treatment of the A_y modulation, can be relaxed. By expanding the y wavefunction in a basis of unperturbed harmonic oscillators, it is possible to well describe the lowest energy states of the modulated waveguide. However, this requires a large number of states, and given that a large number of coefficients are already required for expansion in x, the less numerically-consuming method has been used. The next step is to utilise this exact method, which would allow for the angular momentum of the states to be calculated to draw parallels with chiral-induced spin-selectivity and also with optical waveguides for which this has been done [80]. Optical waveguides form a large field with rich physics, and having a platform to perform similar experiments with electrons as photons could lead to novel technological applications.

The Hartree-Fock-Bogoliubov model used does not allow for the direct calculation of the conductance, and requires interaction to be weak. The first of these could be overcome by using dynamical mean-field theory (DMFT) or a Green's function approach to interacting transport. The latter, however, would need Luttinger liquid or density matrix renormalization group (DMRG) analysis. While all of these could in principle be performed, the approach taken in this thesis provides a solid first model for the systems considered. Rather than searching for a quantitative agreement with the experiments, I sought to understand whether the qualitative physical features of the experiments could be modelled using these techniques. I would say that I have been successful in this regard.

The model of triplet scattering at the helical-unmodulated interface is a potential explanation for the presence of conductance oscillations seen in experiments in helical LAO/STO nanowires. This could be probed in more detail by increasing the length of the unmodulated regions. Because the unmodulated region does not support triplet pairing, the triplet pairs would be expected to decay as a function of the length, and so the observed conductance oscillations would be reduced for longer unmodulated regions.

Bibliography

[1] S. Datta, *Quantum Transport: Atom to Transistor*. Cambridge University Press, 2005.

[2] C.-C. Chien, S. Peotta, and M. Di Ventra, "Quantum transport in ultracold atoms," *Nature Physics*, vol. 11, pp. 998–1004, Dec 2015.

[3] L. J. LeBlanc, K. Jiménez-García, R. A. Williams, M. C. Beeler, A. R. Perry, W. D. Phillips, and I. B. Spielman, "Observation of a superfluid hall effect," *Proceedings of the National Academy of Sciences*, vol. 109, no. 27, pp. 10811–10814, 2012.

[4] S. Krinner, D. Stadler, D. Husmann, J.-P. Brantut, and T. Esslinger, "Observation of quantized conductance in neutral matter," *Nature*, vol. 517, pp. 64–67, Jan 2015.

[5] F. A. Buot, *Nonequilibrium Quantum Transport Physics in Nanosystems.* WORLD SCIENTIFIC, 2009.

[6] D. Ferraro, M. Campisi, G. M. Andolina, V. Pellegrini, and M. Polini, "High-power collective charging of a solid-state quantum battery," *Phys. Rev. Lett.*, vol. 120, p. 117702, Mar 2018.

[7] S. Sweeney and A. Adams, *Optoelectronic Devices and Materials*, pp. 887–916. Boston, MA: Springer US, 2007.

[8] J. Gooth, M. Borg, H. Schmid, V. Schaller, S. Wirths, K. Moselund, M. Luisier, S. Karg, and H. Riel, "Ballistic one-dimensional InAs nanowire cross-junction interconnects," *Nano Letters*, vol. 17, pp. 2596–2602, Apr 2017.

[9] A. Ohtomo and H. Y. Hwang, "A high-mobility electron gas at the $LaAlO_3/SrTiO_3$ heterointerface," *Nature*, vol. 427, pp. 423–426, Jan 2004.

[10] C. Cen, S. Thiel, G. Hammerl, C. W. Schneider, K. E. Andersen, C. S. Hellberg, J. Mannhart, and J. Levy, "Nanoscale control of an interfacial metal–insulator transition at room temperature," *Nature Materials*, vol. 7, pp. 298–302, Apr 2008.

[11] S. Thiel, G. Hammerl, A. Schmehl, C. W. Schneider, and J. Mannhart, "Tunable quasi-two-dimensional electron gases in oxide heterostructures," *Science*, vol. 313, no. 5795, pp. 1942–1945, 2006.

[12] A. Brinkman, M. Huijben, M. van Zalk, J. Huijben, U. Zeitler, J. C. Maan, W. G. van der Wiel, G. Rijnders, D. H. A. Blank, and H. Hilgenkamp, "Magnetic effects at the interface between non-magnetic oxides," *Nature Materials*, vol. 6, pp. 493–496, Jul 2007.

[13] N. Reyren, S. Thiel, A. D. Caviglia, L. F. Kourkoutis, G. Hammerl, C. Richter, C. W. Schneider, T. Kopp, A.-S. Rüetschi, D. Jaccard, M. Gabay, D. A. Muller, J.-M. Triscone, and J. Mannhart, "Superconducting interfaces between insulating oxides," *Science*, vol. 317, no. 5842, pp. 1196–1199, 2007.

[14] D. Hangleiter, J. Carolan, and K. P. Y. Thébault, *Analogue Quantum Simulation.* Springer International Publishing, 2022.

[15] G. Cheng, M. Tomczyk, A. B. Tacla, H. Lee, S. Lu, J. P. Veazey, M. Huang, P. Irvin, S. Ryu, C.-B. Eom, A. Daley, D. Pekker, and J. Levy, "Tunable electron-electron interactions in $LaAlO_3/SrTiO_3$ nanostructures," *Phys. Rev. X*, vol. 6, p. 041042, Dec 2016.

[16] C. Beenakker and H. van Houten, "Quantum transport in semiconductor nanostructures," in *Semiconductor Heterostructures and Nanostructures* (H. Ehrenreich and D. Turnbull, eds.), vol. 44 of *Solid State Physics*, pp. 1–228, Academic Press, 1991.

[17] P. A. Mello and N. Kumar, *Quantum Transport in Mesoscopic Systems: Complexity and Statistical Fluctuations. A Maximum Entropy Viewpoint.* Oxford University Press, 05 2004.

[18] T. Giamarchi, *Quantum Physics in One Dimension.* Oxford University Press, 12 2003.

[19] B. J. van Wees, H. van Houten, C. W. J. Beenakker, J. G. Williamson, L. P. Kouwenhoven, D. van der Marel, and C. T. Foxon, "Quantized conductance of point contacts in a two-dimensional electron gas," *Phys. Rev. Lett.*, vol. 60, pp. 848–850, Feb 1988.

[20] R. Landauer, "Can a length of perfect conductor have a resistance?," *Physics Letters A*, vol. 85, no. 2, pp. 91–93, 1981.

[21] D. A. Wharam, T. J. Thornton, R. Newbury, M. Pepper, H. Ahmed, J. E. F. Frost, D. G. Hasko, D. C. Peacock, D. A. Ritchie, and G. A. C. Jones, "One-

dimensional transport and the quantisation of the ballistic resistance," *Journal of Physics C: Solid State Physics*, vol. 21, p. L209, mar 1988.

[22] A. Annadi, G. Cheng, H. Lee, J.-W. Lee, S. Lu, A. Tylan-Tyler, M. Briggeman, M. Tomczyk, M. Huang, D. Pekker, C.-B. Eom, P. Irvin, and J. Levy, "Quantized ballistic transport of electrons and electron pairs in $LaAlO_3/SrTiO_3$ nanowires," *Nano Letters*, vol. 18, no. 7, pp. 4473–4481, 2018.

[23] Y. Meir and N. S. Wingreen, "Landauer formula for the current through an interacting electron region," *Phys. Rev. Lett.*, vol. 68, pp. 2512–2515, Apr 1992.

[24] D. L. Maslov and M. Stone, "Landauer conductance of luttinger liquids with leads," *Phys. Rev. B*, vol. 52, pp. R5539–R5542, Aug 1995.

[25] C. Smith, M. Pepper, H. Ahmed, J. Frost, D. Hasko, D. Peacock, D. Ritchie, and G. Jones, "Quantum ballistic transport through a zero-dimensional structure," *Superlattices and Microstructures*, vol. 5, no. 4, pp. 599–602, 1989.

[26] F. Martins, S. Faniel, B. Rosenow, H. Sellier, S. Huant, M. G. Pala, L. Desplanque, X. Wallart, V. Bayot, and B. Hackens, "Coherent tunnelling across a quantum point contact in the quantum hall regime," *Scientific Reports*, vol. 3, p. 1416, Mar 2013.

[27] E. Mikheev, I. T. Rosen, J. Kombe, F. Damanet, M. A. Kastner, and D. Goldhaber-Gordon, "A clean ballistic quantum point contact in strontium titanate," *Nature Electronics*, vol. 6, pp. 417–424, Jun 2023.

[28] N. J. Tao, "Electron transport in molecular junctions," *Nature Nanotechnology*, vol. 1, pp. 173–181, Dec 2006.

[29] L. P. Kouwenhoven, A. T. Johnson, N. C. van der Vaart, A. van der Enden, C. J. P. M. Harmans, and C. T. Foxon, "Quantized current in a quantum dot turnstile," *Zeitschrift für Physik B Condensed Matter*, vol. 85, pp. 381–388, Oct 1991.

[30] S. Frank, P. Poncharal, Z. L. Wang, and W. A. de Heer, "Carbon nanotube quantum resistors," *Science*, vol. 280, no. 5370, pp. 1744–1746, 1998.

[31] S. Blankenburg, J. Cai, P. Ruffieux, R. Jaafar, D. Passerone, X. Feng, K. Müllen, R. Fasel, and C. A. Pignedoli, "Intraribbon heterojunction formation in ultranarrow graphene nanoribbons," *ACS Nano*, vol. 6, pp. 2020–2025, Mar 2012.

[32] A. F. Young and P. Kim, "Quantum interference and klein tunnelling in graphene heterojunctions," *Nature Physics*, vol. 5, pp. 222–226, Mar 2009.

[33] B. Kumanek, K. Z. Milowska, Ł. Przypis, G. Stando, K. Matuszek, D. MacFarlane, M. C. Payne, and D. Janas, "Doping engineering of single-walled carbon nanotubes by nitrogen compounds using basicity and alignment," *ACS Applied Materials & Interfaces*, vol. 14, pp. 25861–25877, Jun 2022.

[34] O. A. Jaramillo-Quintero, R. V. Barrera-Peralta, A. Baron-Jaimes, R. A. Miranda-Gamboa, and M. E. Rincon, "Sb(2)O(3) nanoparticles anchored on n-doped graphene nanoribbons as improved anode for sodium-ion batteries," *RSC Adv*, vol. 11, pp. 31566–31571, Sept. 2021.

[35] P. W. Anderson, "Absence of diffusion in certain random lattices," *Phys. Rev.*, vol. 109, pp. 1492–1505, Mar 1958.

[36] M. Cutler and N. F. Mott, "Observation of anderson localization in an electron gas," *Phys. Rev.*, vol. 181, pp. 1336–1340, May 1969.

[37] J. M. Moix, M. Khasin, and J. Cao, “Coherent quantum transport in disordered systems: I. the influence of dephasing on the transport properties and absorption spectra on one-dimensional systems,” *New Journal of Physics*, vol. 15, p. 085010, aug 2013.

[38] J. Z. Imbrie, “On many-body localization for quantum spin chains,” *Journal of Statistical Physics*, vol. 163, pp. 998–1048, Jun 2016.

[39] S. S. Kondov, W. R. McGehee, W. Xu, and B. DeMarco, “Disorder-induced localization in a strongly correlated atomic hubbard gas,” *Phys. Rev. Lett.*, vol. 114, p. 083002, Feb 2015.

[40] M. Kulig, J. Zipfel, P. Nagler, S. Blanter, C. Schüller, T. Korn, N. Paradiso, M. M. Glazov, and A. Chernikov, “Exciton diffusion and halo effects in monolayer semiconductors,” *Phys. Rev. Lett.*, vol. 120, p. 207401, May 2018.

[41] M. Wurdack, E. Estrecho, S. Todd, T. Yun, M. Pieczarka, S. K. Earl, J. A. Davis, C. Schneider, A. G. Truscott, and E. A. Ostrovskaya, “Motional narrowing, ballistic transport, and trapping of room-temperature exciton polaritons in an atomically-thin semiconductor,” *Nature Communications*, vol. 12, p. 5366, Sep 2021.

[42] J. Schooley, W. Hosler, and M. L. Cohen, “Superconductivity in semiconducting srtio3,” *Physical Review Letters*, vol. 12, no. 17, p. 474 – 475, 1964. Cited by: 630.

[43] N. Nakagawa, H. Y. Hwang, and D. A. Muller, “Why some interfaces cannot be sharp,” *Nature Materials*, vol. 5, pp. 204–209, Mar 2006.

[44] F. Schoofs, M. A. Carpenter, M. E. Vickers, M. Egilmez, T. Fix, J. E. Kleibeuker, J. L. MacManus-Driscoll, and M. G. Blamire, “Carrier density modulation by structural distortions at modified $LaAlO_3/SrTiO_3$ interfaces,” *Journal of Physics: Condensed Matter*, vol. 25, p. 175005, apr 2013.

[45] H. P. R. Frederikse and W. R. Hosler, “Hall mobility in $SrTiO_3$,” *Phys. Rev.*, vol. 161, pp. 822–827, Sep 1967.

[46] A. Kalabukhov, R. Gunnarsson, J. Börjesson, E. Olsson, T. Claeson, and D. Winkler, “Effect of oxygen vacancies in the $SrTiO_3$ substrate on the electrical properties of the $LaAlO_3/SrTiO_3$ interface,” *Phys. Rev. B*, vol. 75, p. 121404, Mar 2007.

[47] M. Briggeman, H. Lee, J.-W. Lee, K. Eom, F. Damanet, E. Mansfield, J. Li, M. Huang, A. J. Daley, C.-B. Eom, P. Irvin, and J. Levy, “One-dimensional kronig–penney superlattices at the $LaAlO_3/SrTiO_3$ interface,” *Nature Physics*, vol. 17, pp. 782–787, Jul 2021.

[48] M. Briggeman, J. Li, M. Huang, H. Lee, J.-W. Lee, K. Eom, C.-B. Eom, P. Irvin, and J. Levy, “Engineered spin-orbit interactions in $LaAlO_3/SrTiO_3$-based 1d serpentine electron waveguides,” *Science Advances*, vol. 6, no. 48, p. eaba6337, 2020.

[49] M. Briggeman, *Experimental solid state quantum simulation using 1d superlattice structures.* PhD thesis, University of Pittsburgh, 2019.

[50] F. Damanet, E. Mansfield, M. Briggeman, P. Irvin, J. Levy, and A. J. Daley, “Spin-orbit-assisted electron pairing in one-dimensional waveguides,” *Phys. Rev. B*, vol. 104, p. 125103, Sep 2021.

[51] M. Briggeman, E. Mansfield, J. Kombe, F. Damanet, H. Lee, S. Biswas, J. Li, M. Huang, C.-B. Eom, P. Irvin, A. J. Daley, and J. Levy, “Engineered chirality of one-dimensional nanowires.” Submitted Oct. 2023.

[52] Y. V. Nazarov and Y. M. Blanter, *Quantum Transport: Introduction to Nanoscience.* Cambridge University Press, 2009.

[53] R. Landauer, “Spatial variation of currents and fields due to localized scatterers in metallic conduction,” *IBM Journal of Research and Development*, vol. 1, no. 3, pp. 223–231, 1957.

[54] M. Büttiker, Y. Imry, R. Landauer, and S. Pinhas, “Generalized many-channel conductance formula with application to small rings,” *Phys. Rev. B*, vol. 31, pp. 6207–6215, May 1985.

[55] A. D. Caviglia, M. Gabay, S. Gariglio, N. Reyren, C. Cancellieri, and J.-M. Triscone, “Tunable rashba spin-orbit interaction at oxide interfaces,” *Phys. Rev. Lett.*, vol. 104, p. 126803, Mar 2010.

[56] Z. Zhong, A. Tóth, and K. Held, “Theory of spin-orbit coupling at $\mathrm{LaAlO_3/SrTiO_3}$ interfaces and $\mathrm{SrTiO_3}$ surfaces,” *Phys. Rev. B*, vol. 87, p. 161102, Apr 2013.

[57] S. Datta and B. Das, “Electronic analog of the electro-optic modulator,” *Applied Physics Letters*, vol. 56, no. 7, pp. 665–667, 1990.

[58] R. M. Lutchyn, J. D. Sau, and S. Das Sarma, “Majorana fermions and a topological phase transition in semiconductor-superconductor heterostructures,” *Phys. Rev. Lett.*, vol. 105, p. 077001, Aug 2010.

[59] Y. A. Bychkov and E. I. Rashba, "Oscillatory effects and the magnetic susceptibility of carriers in inversion layers," *Journal of Physics C: Solid State Physics*, vol. 17, p. 6039, nov 1984.

[60] C. Kittel, *Introduction to Solid State Physics.* Wiley, 8 ed., 2004.

[61] R. de Laer Kronig and W. G. Penney, "Quantum mechanics of electrons in crystal lattices," *Proceedings of The Royal Society A: Mathematical, Physical and Engineering Sciences*, vol. 130, pp. 499–513, 1931.

[62] D. J. Griffiths and D. F. Schroeter, *Introduction to Quantum Mechanics.* Cambridge University Press, 3 ed., 2018.

[63] F. Bloch, "Über die quantenmechanik der elektronen in kristallgittern," *Zeitschrift für Physik*, vol. 52, pp. 555–600, Jul 1929.

[64] A. Leggett, *Quantum Liquids: Bose condensation and Cooper pairing in condensed-matter systems.* United Kingdom: Oxford University Press, Jan. 2008. Publisher Copyright: © Oxford University Press, 2014.

[65] M. Tinkham, *Introduction to Superconductivity.* Dover Publications, 2 ed., June 2004.

[66] D. Pekker, C. S. Hellberg, and J. Levy, "Theory of superconductivity at the laalo3/srtio3 heterointerface: Electron pairing mediated by deformation of ferroelastic domain walls," 2020.

[67] M. Briggeman, M. Tomczyk, B. Tian, H. Lee, J.-W. Lee, Y. He, A. Tylan-Tyler, M. Huang, C.-B. Eom, D. Pekker, R. S. K. Mong, P. Irvin, and J. Levy, "Pascal conductance series in ballistic one-dimensional $LaAlO_3/SrTiO_3$ channels," *Science*, vol. 367, no. 6479, pp. 769–772, 2020.

[68] L. Zhang, P. Brusheim, and H. Q. Xu, “Multimode electron transport through quantum waveguides with spin-orbit interaction modulation: Applications of the scattering matrix formalism,” *Phys. Rev. B*, vol. 72, p. 045347, Jul 2005.

[69] J. Hyttel, K. P. Bøgesø, J. Perregaard, and C. Sánchez, “The pharmacological effect of citalopram resides in the (s)-(+)-enantiomer,” *Journal of Neural Transmission / General Section JNT*, vol. 88, pp. 157–160, Jun 1992.

[70] I. A. Jaffe, K. Altman, and P. Merryman, “The antipyridoxine effect of penicillamine in man,” *The Journal of Clinical Investigation*, vol. 43, pp. 1869–1873, 10 1964.

[71] D. Winogradoff, P.-Y. Li, H. Joshi, L. Quednau, C. Maffeo, and A. Aksimentiev, “Chiral systems made from DNA,” *Advanced Science*, vol. 8, no. 5, p. 2003113, 2021.

[72] K. Ray, S. P. Ananthavel, D. H. Waldeck, and R. Naaman, “Asymmetric scattering of polarized electrons by organized organic films of chiral molecules,” *Science*, vol. 283, no. 5403, pp. 814–816, 1999.

[73] Y.-H. Kim, Y. Zhai, H. Lu, X. Pan, C. Xiao, E. A. Gaulding, S. P. Harvey, J. J. Berry, Z. V. Vardeny, J. M. Luther, and M. C. Beard, “Chiral-induced spin selectivity enables a room-temperature spin light-emitting diode,” *Science*, vol. 371, no. 6534, pp. 1129–1133, 2021.

[74] K. Banerjee-Ghosh, O. B. Dor, F. Tassinari, E. Capua, S. Yochelis, A. Capua, S.-H. Yang, S. S. P. Parkin, S. Sarkar, L. Kronik, L. T. Baczewski, R. Naaman, and Y. Paltiel, “Separation of enantiomers by their enantiospecific interaction with achiral magnetic substrates,” *Science*, vol. 360, no. 6395, pp. 1331–1334, 2018.

[75] M. Cahay, M. McLennan, and S. Datta, "Conductance of an array of elastic scatterers: A scattering-matrix approach," *Phys. Rev. B*, vol. 37, pp. 10125–10136, Jun 1988.

[76] E. Maniv, M. B. Shalom, A. Ron, M. Mograbi, A. Palevski, M. Goldstein, and Y. Dagan, "Strong correlations elucidate the electronic structure and phase diagram of $LaAlO_3/SrTiO_3$ interface," *Nature Communications*, vol. 6, 9 2015.

[77] R. I. Shekhter, O. Entin-Wohlman, M. Jonson, and A. Aharony, "Rashba splitting of cooper pairs," *Phys. Rev. Lett.*, vol. 116, p. 217001, May 2016.

[78] Jérome, D., Mazaud, A., Ribault, M., and Bechgaard, K., "Superconductivity in a synthetic organic conductor $(TMTSF)_2PF_6$," *J. Physique Lett.*, vol. 41, no. 4, pp. 95–98, 1980.

[79] K. Bechgaard, K. Carneiro, M. Olsen, F. B. Rasmussen, and C. S. Jacobsen, "Zero-pressure organic superconductor: Di-(tetramethyltetraselenafulvalenium)-perchlorate $[(TMTSF)_2ClO_4]$," *Phys. Rev. Lett.*, vol. 46, pp. 852–855, Mar 1981.

[80] X. Ma, C.-H. Liu, G. Chang, and A. Galvanauskas, "Angular-momentum coupled optical waves in chirally-coupled-core fibers," *Opt. Express*, vol. 19, pp. 26515–26528, Dec 2011.